

Impact of interfaces on the structural and electrical properties of epitaxial PZT heterostructures

D i s s e r t a t i o n

zur Erlangung akademischen Grades
doctor rerum naturalium (Dr. rer. nat.)

vorgelegt der
Naturwissenschaftlichen Fakultät II
der Martin-Luther-Universität Halle-Wittenberg

von Herrn Ludwig Feigl
geb. am 24.04.1980 in Jena

Gutachter:

1. Prof. D. Hesse
2. Prof. H. Beige
3. Prof. H.-N. Lee

Halle (Saale), 26.01.2009

Contents

List of abbreviations	5
1 Introduction	7
2 Fundamentals	9
2.1 Ferroelectrics	9
2.2 Thin films	15
3 Experimental	21
3.1 Film growth: Pulsed laser deposition	21
3.2 Characterisation methods	27
3.2.1 Scanning probe microscopy	27
3.2.2 Transmission electron microscopy	28
3.2.3 X-ray investigations	31
3.2.4 Electrical measurements	33
3.2.5 Rutherford backscattering spectroscopy	33
3.2.6 Electron paramagnetic resonance	34
4 Results	37
4.1 Properties of single composition films	37
4.2 Modification by one additional interface	52
4.3 Chromium doping of PZT20/80	68
4.4 Impact of increased density of interfaces	79
5 Summary	95
Bibliography	99

List of abbreviations

a	smaller tetragonal lattice parameter
a_c	cubic lattice parameter
AFM	atomic force microscopy
a_{pc}	pseudocubic lattice parameter
BF	bright field
c	larger tetragonal lattice parameter
DF	dark field
DFT	density functional theory
EDX	energy-dispersive X-ray spectroscopy
EPR	electron paramagnetic resonance
ϵ_r	dielectric constant
f	lattice misfit
Φ_a	fraction of a -domains
FeRAM	ferroelectric random access memory
f_{RT}	misfit strain at room temperature
FS	fine-structure
HAADF	high-angle annular dark field
h_C	critical thickness for the introduction of misfit dislocations
HRSTEM	high resolution scanning transmission electron microscopy
HRTEM	high resolution transmission electron microscopy
LGD	Landau-Ginzburg-Devonshire
MD	misfit dislocation
n	density of mobile charges (electrons)
N_{eff}	density of fixed space charges
NSM	Newman superposition model
PFM	piezoresponse force microscopy
Φ_B^0	Schottky barrier height at zero voltage
PLD	pulsed laser deposition
P_r	remanent polarisation
PZT	$PbZr_xTi_{1-x}O_3$ (lead zirconate-titanate)
PZT20/80	$PbZr_{0.2}Ti_{0.8}O_3$ (lead zirconate-titanate)

PZT40/60	$PbZr_{0.4}Ti_{0.6}O_3$ (lead zirconate-titanate)
PZT:Cr _x	$PbZr_{0.2}Ti_{0.8}Cr_{x/100}O_3$ (chromium doped lead zirconate titanate)
RBS	Rutherford backscattering spectroscopy
RSM	reciprocal space mapping
SAD	selected area diffraction
SEM	scanning electron microscope
SRO	$SrRuO_3$ (strontium ruthenate)
STO	$SrTiO_3$ (strontium titanate)
T	temperature
T_C	Curie temperature
TD	threading dislocation
TEM	transmission electron microscopy / microscope
V_{bi}	built-in voltage

1 Introduction

Ferroelectric thin films are in the focus of extensive research efforts for applications including but not limited to capacitors, pyroelectric sensors, ferroelectric random access memories and valves for ink, fuel or medicines [1, 2, 3, 4, 5]. In order to integrate ferroelectrics into suitable devices, miniaturisation is essential [6, 7]. Some of the main challenges that have been faced during the course of the research devoted to ferroelectrics are size-related phenomena. These have stimulated intense scientific debate owing to the apparently new physical properties that thin-film and nanoscale ferroelectrics possess compared to bulk material. For instance new effects may arise in thin films which influence the resulting properties. Due to the different lattice parameters of film and substrate, dislocations are frequently formed within the film [8, 9, 10, 11, 12, 13]. If the film thickness is reduced to below a certain critical value, strains occurring at interfaces become important [14], enabling strain engineering of the ferroelectric properties [15], e.g. by tailoring growth on different substrates [16]. Another approach to tune the properties of thin films is to grow heterostructures consisting of different ferroelectric materials [17]. It is also possible to combine ferroelectrics with other classes of materials as dielectrics [18, 19] or even semi- [20] or superconductors [21]. This way of fabricating heterostructures also allows to control the strain and microstructure by choosing the appropriate components comprising the functional system.

In all these attempts a highly controlled microstructure is essential. The formation of strain, dislocations, and domain structures in ferroelectric thin films strongly impacts the ferroelectric properties. These features usually originate at the interfaces, and therefore a careful design of interfaces allows to control these structural characteristics. $PbZr_xTi_{1-x}O_3$ is a ferroelectric material most commonly used for applications because of its high piezoelectric coefficients. Furthermore, it crystallises in the rather simple perovskite structure which makes it a good model system for fundamental research. In the frame of this work the influence of interfaces on the ferroelectric properties are investigated using two similar tetragonal ferroelectric materials, viz. $PbZr_{0.2}Ti_{0.8}O_3$ and $PbZr_{0.4}Ti_{0.6}O_3$.

Chapter 2 addresses the fundamentals required for the understanding of this topic. That is on one hand the general properties of perovskites (Section 2.1) including a closer look on the used materials and the model system of $PbZr_xTi_{1-x}O_3$ as a ferroelectric and a wide bandgap semiconductor. On the other hand the various growth modes of thin films are reviewed. The dislocation formation during growth is theoretically described. It depends

on the lattice misfit and the layer thickness of the combined materials (Section 2.2).

In the first part of the experimental Chapter (Chapter 3) fabrication methods are introduced and the possible influence of the deposition conditions is explained (Section 3.1). The second part contains details on the characterisation methods used to analyse the structure and electrical properties of the films. Scanning probe microscopy including atomic force microscopy in conventional and in piezoresponse mode was applied to investigate the topography and the domain structure at the surface of the grown films (Section 3.2.1). In order to reveal the microstructure, dislocations and a -domains were imaged, and the layer thickness was determined by (high resolution scanning) transmission electron microscopy (Section 3.2.2) of cross-sectional samples. Electron paramagnetic resonance (Section 3.2.6) was applied to probe point defects. X-ray diffraction measurements were performed to obtain information on the crystal structure from a larger part of the film compared to the very local transmission electron microscopy investigations (Section 3.2.3). Energy dispersive X-ray spectroscopy was applied during transmission electron microscopy to analyse the composition of the film. Another method used to determine the film composition is RUTHERFORD backscattering spectroscopy (Section 3.2.5). Electrical investigations were performed on the fabricated films as described in Section 3.2.4.

All specified investigation methods were used to reveal the properties of the fabricated heterostructures as shown in Chapter 4. The key term of this work is the modification of the ferroelectric films via interfaces, including the interface between the electrode and a single ferroelectric layer. The lattice misfit introduced at this interface determines the properties of the ferroelectric film as shown in Section 4.1. This is the simplest design without any modifications of the ferroelectric film. However, it leaves only few possibilities to further tune the properties. These possibilities are (i) the variation of the thickness with its known consequences [22, 23, 24, 25] and (ii) doping. Therefore the latter is also investigated. An artificial interface is introduced into the ferroelectric film by growing two layers to have more degrees of freedom in influencing the film properties. In Section 4.2 the strong impact of this structural modification is experimentally demonstrated and theoretically described. Differences between the used model and experimental data are discussed in the following chapters. Section 4.3 investigates the influence of doping on the properties of the ferroelectric film. Section 4.4 shows the effect of a systematic increase of the density of interfaces by growing multilayers.

Chapter 5 briefly summarises the discussed results and gives a short outlook on future research.

2 Fundamentals

2.1 Ferroelectrics

Applications

A direct application of the specific properties of ferroelectrics is the utilisation of the switchable remanent polarisation in order to create non-volatile ferroelectric random access memories (FeRAMs). However, the most common areas of applying ferroelectrics use attributes resulting from their dielectric, piezoelectric and pyroelectric properties. Ferroelectric ceramics, for instance, can be found as dielectrics in capacitors. Furthermore, due to the tunability of the dielectric constant by an electric field, ferroelectric films can serve as waveguides. The piezoelectric effect is used for ultrasonic devices, active damping elements, high-precision actuators in microscopes, and valves for inks, fuel, and medicine. Moreover, passive infrared sensors often contain ferroelectric materials. Many other applications have been suggested as recently summarised by Scott [4].

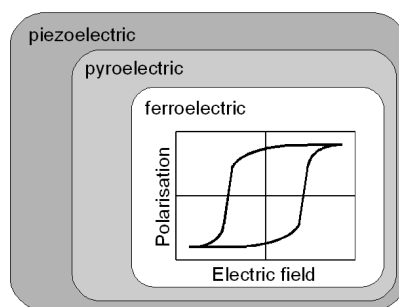


Figure 2.1: Classification of ferroelectricity after [26]. The inset shows the typical ferroelectric polarisation-field hysteresis curve. The polarisation is switched if a critical field strength is reached.

Properties

Ferroelectrics belong to the pyroelectric materials which are in turn a subgroup of piezoelectric materials (Fig. 2.1). Piezoelectric materials show an electrical charge if they are exposed to mechanical stress due to the relative displacement of their ions. The piezoelectric effect was discovered in 1880 by Jacques and Pierre Curie on tourmaline single crystals [27]. This effect is only possible in ionic crystals with a crystal structure without

inversion symmetry. In addition to the described effect of piezoelectricity, a pyroelectric crystal builds up a charge when the temperature is changed. Pyroelectric crystals are always polar due to a permanent dipole formed by the lattice ions. Under conditions of thermodynamic equilibrium the surface charge is compensated by free carriers from the environment. If the crystal is cooled down or heated up, the distance of the lattice ions will change due to thermal expansion and produce a charge on two opposite sides of the crystal. If the polarisation of a pyroelectric material can be switched between two thermodynamically stable states, then the material is called ferroelectric [28]. For ferroelectric switching an electric field higher than the according threshold value has to be applied opposite to the direction of the polarisation. This results in the well-known hysteresis curve showing the polarisation switching in dependence on the applied electric field $P(E)$ which is typical for ferroelectric materials (Fig. 2.1).

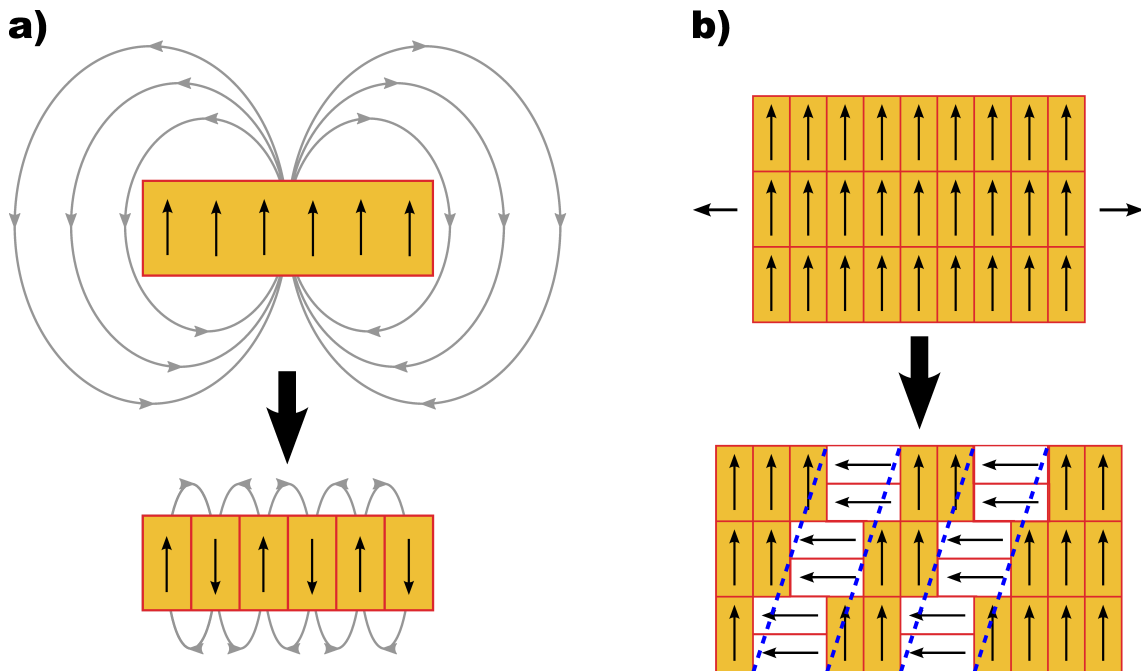


Figure 2.2: Domains are generally formed to reduce the free energy of the ferroelectric. There are basically two different types of domains: **a)** Formation of electric 180° domain walls to reduce the high energy necessary to maintain the wide spread of the electric field. This energy can be reduced if the electric flux lines are short-circuited by the domains. **b)** Formation of elastic 90° domain walls to accommodate tensile stress (blue dashed lines). By tilting the direction of the polarisation, the ferroelectric is able to expand in the direction of the stress.

The direction of the polarisation is not uniform throughout the whole ferroelectric, but regions of a common polarisation state, so-called domains, are formed. Depending on the crystal symmetry, different angles between the directions of the polarisation in adjacent domains are possible. These are separated by domain walls denominated by this angle (e.g. 180° domain wall). The domain walls exhibit a finite thickness which may range from one to ten unit cells for 180° domain walls in $Pb(Zr,Ti)O_3$ films as recently shown by direct investigations using high resolution transmission electron microscopy

[29]. Domains are generally formed to reduce the free energy of the system. Ideally, to decrease the electric stray field, domains with an opposite sign of polarisation will develop to short the electric flux lines (Fig. 2.2a). Their formation does not impact any strain states.

Another domain type occurs if a ferroelectric material has a paraelectric phase which is cubic so that in the ferroelectric phase the polarisation can point into six different directions. To reduce the magnitude of tensile strain, 90° domains are formed (Fig. 2.2b). Due to the relaxation of the elastic deformation by these domains they are also named ferroelastic domains. The domain wall is inclined to avoid charging.

Domains play an important role during polarisation switching. Ferroelectric samples are not switched as a whole but 180° domain walls nucleate and propagate through the sample. Afterwards the lateral motion of the domain walls consumes more volume of the sample until it is switched [22, 30]. The polarisation of 90° domains may also be turned. However, due to mechanical confinements, strong backswitching is likely to occur [31, 32, 33]. A remanent rotation is only possible if it is allowed by the elastic boundary conditions. This may, e.g., happen if the additional strains are compensated elsewhere.

Perovskites

Many ferroelectric materials crystallise in the perovskite structure. The prototype mineral of this structure is $CaTiO_3$. Gustav Rose discovered it in 1839 and named it Perovskite after Lew Alexejewitsch Perowski (a Russian mineralogist). The empirical formula of all perovskites is ABO_3 where A and B are different cations and O is oxygen. Perovskites crystallise in a face-centred sphere packing of the A and O ions with the B ions at a quarter of the octahedral spaces (Fig. 2.3a). The stability of this structure can be estimated by using geometrical considerations to define the GOLDSCHMIDT tolerance factor [34]:

$$t = \frac{r_A + r_O}{\sqrt{2}(r_B + r_O)}. \quad (2.1)$$

The perovskite structure is assumed to be stable for $0.83 < t < 1.07$ [35, 36]. At $t \approx 1$ an ideal cubic structure is realised which is distorted for higher and lower values. This distortion leads to a ferroelectric behaviour for $t > 1$.

In the course of this work, certain $PbZr_xTi_{1-x}O_3$ (PZT) compositions are investigated as a model system for tetragonal ferroelectrics. The high piezoelectric coefficients of PZT make changes of the properties easily observable. Its lattice constants are similar to the paraelectric perovskite $SrTiO_3$ (STO) which is therefore used as a substrate. A further perovskite, $SrRuO_3$ (SRO), exhibits metallic conductivity and also has lattice constants which are very close to that of PZT , therefore SRO is employed as the electrode material. Below, these three materials are discussed in detail.

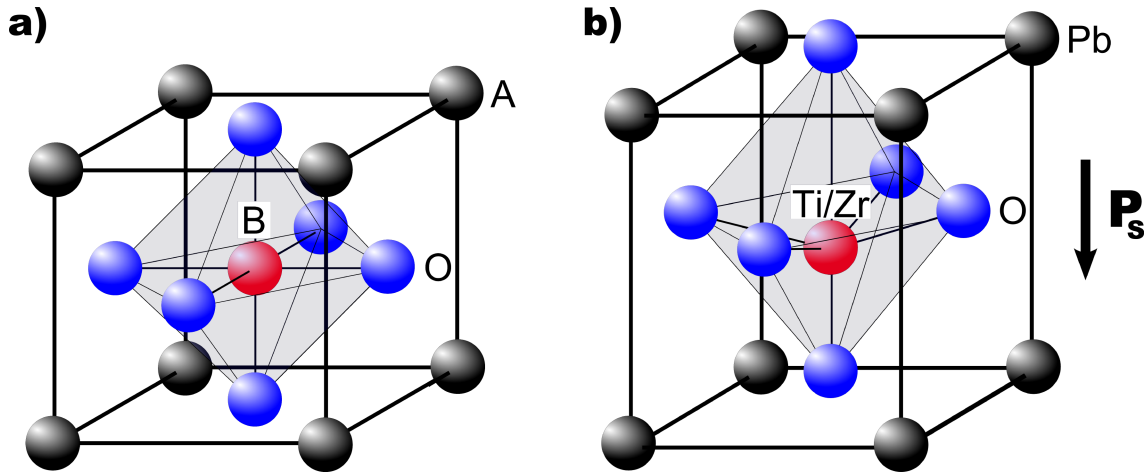


Figure 2.3: **a)** Perovskite structure ABO_3 , black are the A ions, red is the B ion and blue are the O ions. The A and O ions form a face centred cubic lattice. The B ion is located in the octahedral space between the O ions (shaded area). **b)** Unit cell of $PbZr_{0.2}Ti_{0.8}O_3$. The central ions (Zr or Ti) and the O ion are shifted with respect to the Pb ions.

Lead zirconate-titanate: Lead titanate $PbTiO_3$ is a ferroelectric known for its high polarisation values and piezoelectric coefficients. Zr can replace the Ti ions on the B site of the perovskite cell to form the solid solution lead zirconate-titanate $PbZr_xTi_{1-x}O_3$. Depending on the Zr content and the temperature, PZT will exhibit different crystal phases (Fig. 2.4a): for all Ti/Zr ratios above the corresponding CURIE temperature T_C , PZT is paraelectric and cubic (P_C). With increasing Zr content T_C decreases. At the same time the phase below T_C changes from ferroelectric tetragonal (F_T) to ferroelectric rhombohedral (F_R) and finally to antiferroelectric orthorhombic (A_O) with a small region of an antiferroelectric tetragonal (A_T) phase. The central B ion (Zr or Ti) and the O ions are shifted in the ferroelectric phases with respect to the centrosymmetric case (Fig. 2.3). This causes a permanent dipole moment parallel to the shift and therefore a polarisation of the unit cell. The interaction of the unit cells determines the behaviour of the material. For ferroelectric PZT compositions all dipole moments are aligned in parallel. In the antiferroelectric phase the ions of adjacent unit cells are shifted antiparallel to each other which results in zero net polarisation. Also the lattice parameters change with the Zr/Ti ratio and show a splitting in the orthorhombic and tetragonal phases (Fig. 2.4b). PZT cannot be manufactured in the form of large single crystals because of the incongruent melting of the compounds [37]. Therefore, it is widely used in the form of ceramics or thin films. Ceramics consist of grains with different crystal orientations. This leads to an average macroscopic polarisation of about zero. Thus ceramic samples have to be poled using an external electric field to more or less align the polarisation of all the grains. In the case of epitaxial thin films the orientation of the polarisation is not arbitrary but is influenced by mechanical confinements of the underlying substrate. Any difference of the in-plane lattice parameters between substrate and film results in a definite in-plane strain.

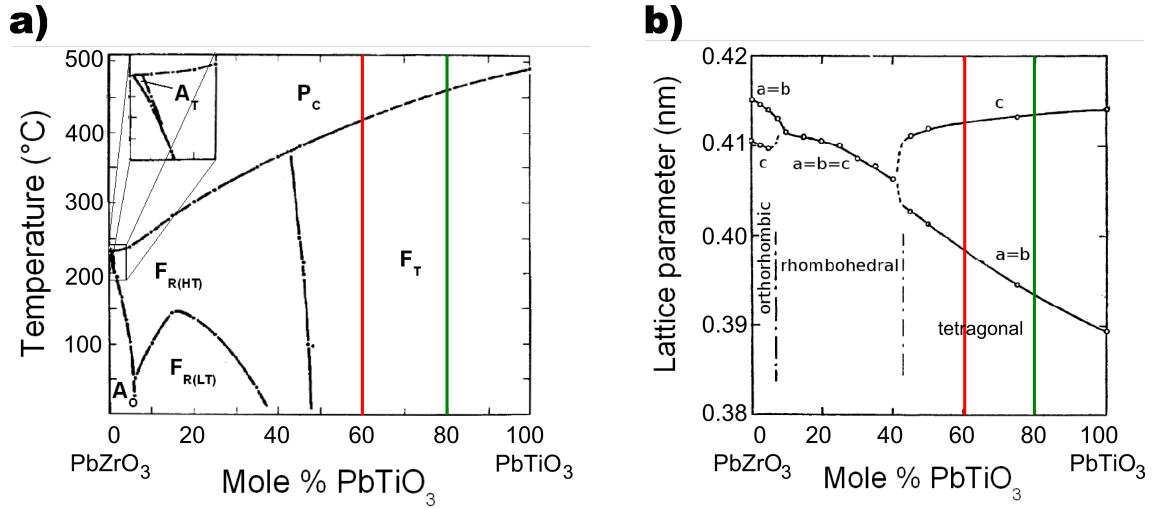


Figure 2.4: **a)** Phase diagram of $PbZr_xTi_{1-x}O_3$ after [38] showing the stability borders of the para-, ferro- and antiferroelectric phases in dependence on the Zr content and the temperature. The coloured lines mark the investigated compositions $PZT40/60$ (red line) and $PZT20/80$ (green line). **b)** Lattice parameter of the ferroelectric and antiferroelectric phases of $PbZr_xTi_{1-x}O_3$ at room temperature versus the Zr content (after [39]).

Compressive strain supports an out-of-plane polarisation whereas tensile strain supports the in-plane polarisation.

In this work, the PZT compositions $PbZr_{0.2}Ti_{0.8}O_3$ ($PZT20/80$, green line in Fig. 2.4) and $PbZr_{0.4}Ti_{0.6}O_3$ ($PZT40/60$, red line in Fig. 2.4) are used. Both of them have a tetragonal crystal structure with the lattice parameters $a_{PZT20/80} = 0.395\text{ nm}$, $c_{PZT20/80} = 0.414(8)\text{ nm}$, $a_{PZT40/60} = 0.400\text{ nm}$ and $c_{PZT40/60} = 0.415(0)\text{ nm}$ [40, 41].

PZT as a wide bandgap semiconductor: In many cases, ferroelectrics can be considered as ideal insulators. In these cases the influence of external factors, such as free carriers, interfaces and local structural defects, can frequently be neglected without important impact on final results and discussions. In systems with reduced dimensionality, such as thin films or nanostructures, these details may play an important role. For instance lead-based ferroelectric thin films have to be treated as semiconductors to correctly interpret the experimental data. The size of the bandgap depends on the composition and on the microstructure (polycrystalline, single crystalline, etc.) [42, 43]. Experimental investigations on single crystalline epitaxial PZT films exhibiting a structural quality comparable to the ones used here have a bandgap of 3.9 eV for $PZT20/80$ and 4.1 eV for $PZT40/60$ [42]. These values are close to those obtained by theoretical descriptions using the density functional theory (DFT) which predicts 3.73 eV for $PZT25/75$ [44]. The sign of the mobile charge carriers is still under discussion. The achieved result depend on the theoretical approach used. If the PZT is described by defect chemistry this would result in p-type conduction [45]. In contrast, n-type conduction is probable when considering the much higher mobility of electrons injected from the electrode which are mainly responsi-

ble for the conduction [46]. Recent experiments performed on single crystalline epitaxial *PZT20/80* films suggest n-type conduction [47].

Strontium titanate: As will be described in Section 2.2, an appropriate substrate is crucial for film growth. Since only *PZT* compositions with $x = 0.2$ and $x = 0.4$ were used, with lattice parameters a of 0.395 nm and 0.400 nm , respectively, the cubic perovskite strontium titanate SrTiO_3 is the chosen substrate. It has a lattice parameter of $a_{\text{STO}} = 0.390\text{ nm}$ [40, 48] which is very close to the lattice parameter a of both ferroelectric compositions and therefore allows epitaxial growth of films with a high crystalline quality. Since the lattice parameter of *STO* is slightly smaller than those of the *PZT* compositions this will favour a c -axis oriented growth of the *PZT* films with an out-of-plane polarisation, an inevitable condition for macroscopic investigations of the polarisation.

Strontium ruthenate: To allow an electrical characterisation of the ferroelectric layers a bottom electrode is required. Strontium ruthenate SrRuO_3 is a perovskite which shows a metallic behaviour. Investigations on *SRO* thin films revealed a resistivity of about $200\mu\Omega\text{cm}$ [49]. It has an orthorhombic structure at room temperature with $a = 0.553\text{ nm}$, $b = 0.557\text{ nm}$ and $c = 0.785\text{ nm}$ [50, 51]. According to Zayak *et al.* [52] these parameters can be converted into the lattice parameter of a slightly distorted cubic phase giving a pseudocubic lattice parameter $a_{\text{SRO}} \sim \frac{a}{\sqrt{2}} \sim \frac{b}{\sqrt{2}} \sim \frac{c}{2} \sim 0.393\text{ nm}$. Thus it lies in between the lattice constants of *STO* and *PZT* and fits very well to both of them. Moreover, the perovskite structure facilitates the growth of the subsequent *PZT* layer. Another advantage of using an oxide electrode is its permeability to oxygen vacancies. These are known as one of the major reasons for fatigue in switching of ferroelectric thin films [53]. If common metal electrodes are used, the oxygen vacancies may agglomerate at the interfaces and thus may deteriorate the switching properties. This effect does not occur with *SRO*, because here the oxygen vacancies can easily cross the respective interface.

2.2 Thin films

Thin films are material layers ranging from fractions of a nanometre to several micrometres in thickness. Electronic semiconductor devices, optical coatings and hard coatings are the current main applications benefiting from thin-film design. In the growing field of solar technology, for example, thin films are introduced with the perspective to substantially reduce the cost of the still expensive photovoltaic systems. Thin-film designs for ferroelectrics reduce the necessary operation voltages and allow their integration into microelectronic devices.

Thin films can be fabricated by either growing from the vapour phase, depositing from a liquid solution or by wafer-bonding onto a substrate. This work will focus on the growth from the vapour phase, for which the various important mechanisms will be detailed below.

Epitaxial Films

The growth of thin films from the vapour phase is preceded by clustering processes of the adatoms on the substrate surface. These basic processes which all take place simultaneously are shown in Fig. 2.5. Adatoms arrive on the surface and are accommodated there. Some of them have enough energy to re-evaporate. Other adatoms are not able to escape due to their lower energy but can still diffuse on the surface. When a certain density of adatoms on the surface is reached, the formation of clusters begins [54]. These clusters are not necessarily stable, atoms might still be re-evaporated. A critical cluster size is reached, when the sum of the atoms diffused to and directly impinged on the cluster is higher than the number of re-evaporated atoms. This cluster is considered to be stable and is called a nucleus. Further growing of the clusters leads to their coalescing and the formation of a continuous film. Nucleation does not occur homogeneously on the surface. Defect sites on a crystal surface generate local minima in the potential and are therefore preferred nucleation sites. This can lead to an acceleration of the nucleation process [55]. Three growth modes dominate the epitaxial growth on flat surfaces:

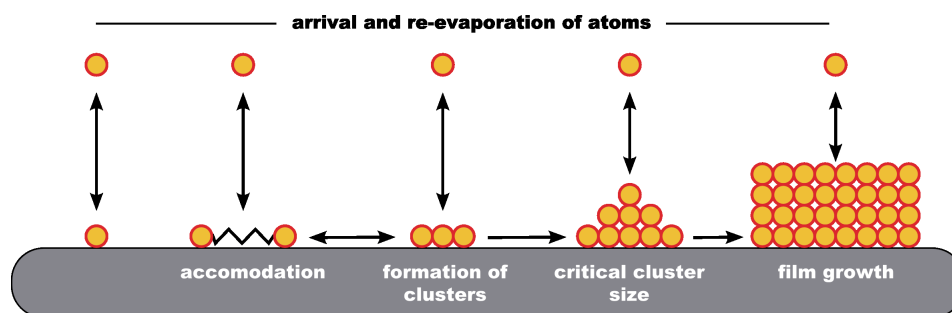


Figure 2.5: Nucleation processes of arriving atoms on the substrate during the initial stage of film growth. Stable clusters are required to enable the formation of films.

1. Two-dimensional FRANK-VAN DER MERWE growth mode (Fig. 2.6a): The film grows in layers, the subsequent atomic layer does not start before the preceding one is complete.
2. Three-dimensional VOLMER-WEBER growth mode (Fig. 2.6b): In this case isolated islands grow. A continuous film is formed when the islands are large enough to come into contact with each other and coalesce. Since the islands do not necessarily have the same orientation the resulting films may exhibit perturbations of the regular lattice structure as twin boundaries.
3. A mixture of both above modes, called STRANSKI-KRASTANOV growth mode (Fig. 2.6c): Here, firstly a continuous film forms, as displayed in Fig. 2.6a. At a later stage of the growth, depending on the properties of film and substrate, the film continues to grow in form of islands, comparable to Fig. 2.6b.

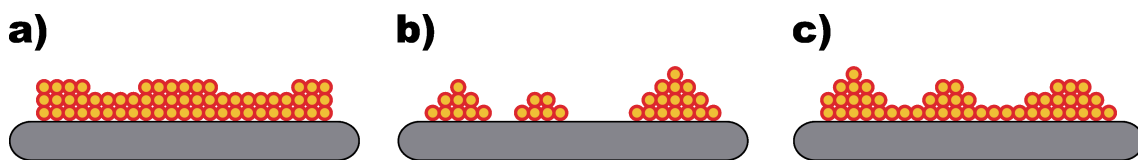


Figure 2.6: Possible growth modes of films on flat surfaces. The mode depends on the interaction strength between adatoms and the surface. The film can grow either **a)** layer-by-layer (FRANK-VAN DER MERWE), **b)** in form of coalescing islands (VOLMER-WEBER) or **c)** in a mixed mode, where layer-by-layer growth is followed by island growth (STRANSKI-KRASTANOV).

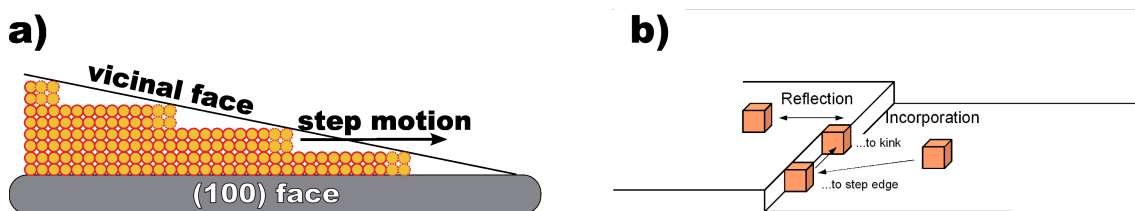


Figure 2.7: **a)** Example of different crystal faces. The (100) face belongs to the so-called singular faces with low Miller indexes. Due to the miscut angle in between the vicinal and the singular face, steps are formed. The direction of the movement of the steps during film growth is indicated. **b)** Possible diffusion paths of atoms at a surface step. If the atom approaches the upper side of the step, it may be reflected. If it approaches from the lower side it will more likely be incorporated into the step.

In addition to these three basic growth modes, two more growth modes are induced by the substrate surface. Thin films cannot be prepared in a freestanding form but have to be grown on substrates. These substrates have to be single crystalline if epitaxial films shall be fabricated. The structure of the crystal face used as substrate determines the growth of the covering film. Low-indexed crystal faces are called singular faces. If the crystal faces differ by small angles from atomically flat faces, they contain lamellar terraces of

singular faces interrupted by monatomic steps. They are called vicinal faces (Fig. 2.7a). The edges of these steps can be considered as defects where preferred nucleation takes place and simultaneously they act as diffusion barriers [56]. Adatoms would have to overcome an energy barrier to diffuse across a step. If their energy is too low to move down a step, they will be reflected. When approaching a step edge from the lower side the atom will most likely be incorporated because it is attracted by more nearest neighbours than on the free surface (Fig. 2.7b) [57]. At a high rate of incoming atoms, islands are formed randomly distributed on the surface. If the rate of arriving atoms is low enough to prevent nucleation on the terraces, the steps will move during the growth process because ideally the atoms are joined only to the step edge. This is the so-called *step-flow growth*, a special kind of layer-by-layer growth. Any perturbation in the rate of the lateral motion of a step leads to the formation of a bunch of steps. The step height is the sum of all steps which contribute to the bunch. Because the velocity of the steps decreases with its height, the bunches move slower than the monatomic steps, which at the end amplifies this effect, resulting in *step bunching*.

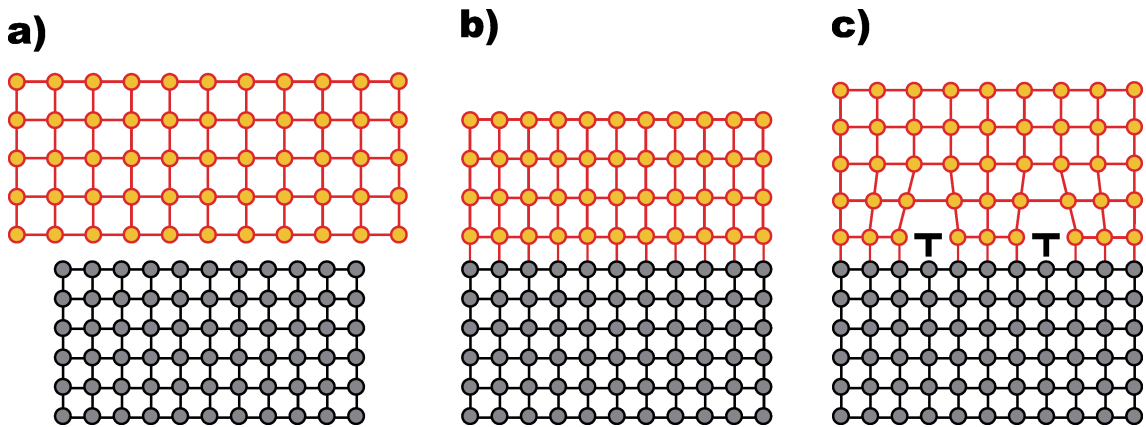


Figure 2.8: Basic principle of the mechanism of the formation of misfit dislocations due to misfit strain. **a)** In heteroepitaxy the film material usually exhibits a different in-plane lattice parameter than the substrate. In the shown case the lattice parameter of the film is larger than that of the substrate. **b)** If the film thickness stays below a critical threshold value ($h < h_C$) the lattice parameter of the film is adapted to that of the substrate. **c)** If the critical thickness is exceeded during film growth ($h > h_C$), misfit dislocations (\top) are introduced to relax the strained film. In the shown example an extra half plane is present in the substrate at each misfit dislocation.

Films are grown on substrates which can either consist of the same (homoepitaxy) or of a different material (heteroepitaxy). In most cases of heteroepitaxy there is a difference in the lattice parameters of the substrate and the film (Fig. 2.8a). In case of identical lattice parameters in both in-plane directions the biaxial misfit f can be defined according to

$$f = \frac{a_s - a_f}{a_f} \quad (2.2)$$

with a_s and a_f the nominal in-plane lattice parameters of the substrate and epitaxial film, respectively. In the first stage of growth of a film with, for example, a larger lattice parameter (Fig. 2.8a) the film is strained to the substrate and grows pseudomorphically (Fig. 2.8b). When the film thickness exceeds a critical thickness h_c , misfit dislocations (MDs) are introduced to release the strain. Each MD results in an extra half crystal plane in the substrate (Fig. 2.8c). The same mechanism holds for films with a smaller lattice constant compared to the substrate. The only difference is the opposite sign of the misfit which leads to the introduction of additional planes in the film. The MDs give rise to threading dislocations (TDs) which propagate to the surface of the film. h_c can be estimated from the forces acting on existing dislocation lines [58]. The force exerted by the misfit strain ε is

$$F_\varepsilon = \frac{2G(1+\nu)}{(1-\nu)}bh\varepsilon \cos \lambda, \quad (2.3)$$

where G is the shear modulus, ν the Poisson ratio, b the Burgers vector, h the film thickness and λ the angle between the slip direction and the direction in the film plane which is perpendicular to the intersection of the slip plane and the interface. The tension in the dislocation line can be estimated as

$$F_l = \frac{Gb^2}{4\pi(1-\nu)}(1-\nu \cos^2 \alpha) \left(\ln \frac{h}{b} + 1 \right), \quad (2.4)$$

with α being the angle between the dislocation line and the Burgers vector. If

$$F_\varepsilon \left(\varepsilon_{max} = \frac{1}{2}f \right) > 2F_l \quad (2.5)$$

the TDs will move. Thereby the coherence of the interface is destroyed and ε is reduced. The critical thickness h_c can be calculated by equating both equations 2.4 and (2.5):

$$h_c = \frac{b}{2\pi f} \frac{(1-\nu \cos^2 \alpha)}{(1+\nu) \cos \lambda} \left(\ln \frac{h_c}{b} + 1 \right). \quad (2.6)$$

This estimation gives the minimum thickness for the introduction of MDs into one layer of a multilayer system. For calculating the critical thickness of a single layer on a thick substrate, two additional boundary conditions have to be considered. Firstly, in a multilayer system the misfit strain is assumed to be shared between the layers, so one layer type is under compression and the other under tension. This is no longer valid for a single layer. Secondly, the moving of a threading dislocation in a sandwiched layer would cause two misfit dislocations, one at each interface, whereas in a single layer only one occurs. Each of these conditions divide the critical thickness by a factor of two resulting in

$$h_c = \frac{b}{8\pi f} \frac{(1-\nu \cos^2 \alpha)}{(1+\nu) \cos \lambda} \left(\ln \frac{h_c}{b} + 1 \right). \quad (2.7)$$

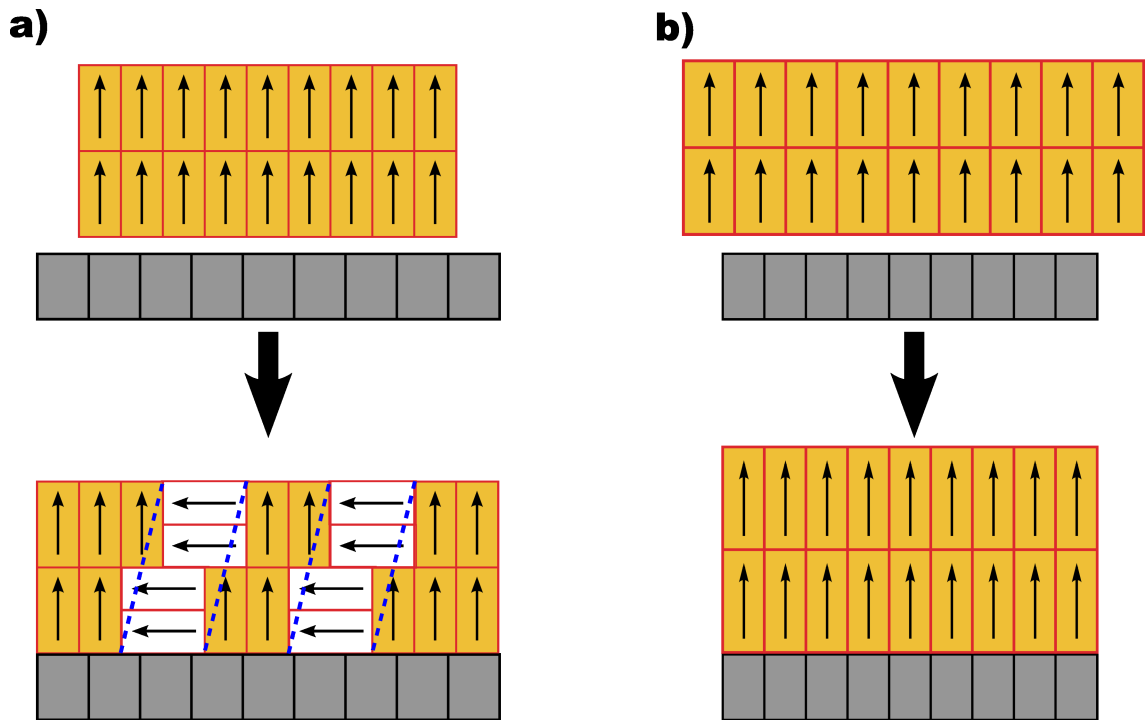


Figure 2.9: Impact of different misfits on the spontaneous polarisation of tetragonal ferroelectric thin films. **a)** If the substrate has a larger lattice parameter than the film, the induced tensile strain leads to the formation of elastic a -domains. The tilt of the spontaneous polarisation to the in-plane direction causes a decrease of the remanent polarisation of the film. **b)** If the substrate has a smaller lattice parameter than the film, the induced compressive strain leads to a higher tetragonality of the unit cell. This enhances the spontaneous polarisation via the electrostrictive coupling (see Eq. 4.1 - 4.2).

However, it is possible to grow coherent films beyond h_c since there are kinetic barriers which slow down or prevent the formation of MDs [23, 59, 60]. The film structure is determined by the growth mode and the density of dislocations. Both are influenced by the intrinsic properties of the materials used for film and substrate, by the film thickness and by the general growth conditions.

Ferroelectric thin films

If ferroelectrics are grown in thin film geometry they are exposed to strong mechanical confinements induced by the supporting substrate. This affects the displacement of the ions which is essential for the development of the ferroelectric effect as well as the formation and movement of the domain walls. Therefore severe changes of the thin film behaviour compared to the bulk properties can be expected.

Depending on the preferred substrate-film combination, either compressive or tensile strains can be introduced into the ferroelectric film. In certain cases, the tensile strain is able to tilt the polarisation vector from the out-of-plane to the in-plane direction [61]. For a tetragonal symmetry the rotation of the unit cell on average results in an effective lattice parameter a_{eff} . This parameter is in the range between the smaller lattice parameter a

and the larger lattice parameter c ($a \leq a_{eff} \leq c$) and is closer to the substrate's lattice parameter (Fig. 2.9a). Another prominent characteristic of electric polarisation is the possibility to enhance it to higher values than these measured in bulk via strain-polarisation electrostrictive coupling (Fig. 2.9b) [62], even though this is not always as extensive as expected [63, 64, 65]. Thus, ferroelectric films can be tuned to exhibit either polarisation values superior to the corresponding bulk material or an outstanding dielectric constant. Other properties like the pyroelectric effect are affected as well [66, 67, 68].

However these considerations only hold true for a very confined thickness range. If a critical thickness is exceeded during film growth, the heteroepitaxial film usually starts to relax by forming misfit dislocations, which is accompanied by threading dislocation formation (see Section 2.2) [58, 69, 70, 71, 72, 73]. Additional stresses could also arise upon cooling down the film from growth temperature to room temperature due to different thermal expansion coefficients between film and substrate. For particular ferroelectric films, a -domains can form below the Curie temperature to further relax the residual stresses [40, 74]. These a -domains are characterised by their polarisation axes lying in the plane of the film-substrate interface. Due to the different elastic strain state and/or lattice parameters the a -domains are detectable in diffraction characterisation such as electron diffraction (Section 3.2.2) or X-ray diffraction (Section 3.2.3). While these relaxation mechanisms give rise to global and local strain relaxation in the film, they can be detrimental for the ferroelectric behaviour [9]. The reason for the latter is that local strain variations induce a position dependent polarisation owing to the electrostrictive nature of these systems. Strong internal electric fields due to polarisation gradients could develop, smearing out the phase transition and even suppressing ferroelectricity.

3 Experimental

3.1 Film growth: Pulsed laser deposition

Pulsed laser deposition (PLD) belongs to the physical vapour deposition methods. A laser is used to ablate a material from an appropriate target and the resulting plume of ions and atoms is deposited on a substrate. PLD was used for the first time in 1965 [75], but due to technical difficulties other techniques like molecular beam epitaxy and sputtering became more popular. With the advancements in laser technology Cheung *et al.* showed in 1983 the possibility of manufacturing films with a quality comparable to the results of other methods [76]. From this date PLD met with an increasing popularity due to its high versatility. Nearly every material, even molten targets [77], can be deposited using an appropriate wavelength of the laser light. Even complex crystal structures can be grown if the optimum parameters are determined. Since this method as a rule transfers the material as a whole, frequently stoichiometric targets can be used which simplifies the handling of a PLD system. The absence of sensitive electrical devices in the deposition chamber allows the use of a reactive atmosphere which broadens the range of depositable materials. By using a multi-target holder, films with layers of different compositions can be made in situ, i.e. without opening the chamber. The strong non-equilibrium conditions during PLD give rise to unique applications: it is possible to grow metastable materials which cannot be fabricated by standard routes, and species which form only during the laser ablation process can be grown into thin films [78]. Finally, the highly directed plume allows a high deposition rate. In the following, the operation principles and the influence of the deposition parameters will be discussed.

Basic principles

When the laser hits an absorbing material the energy is absorbed by electrons and phonons of the lattice, by free charge carriers at the surface, and by the plume of the ablated material [79, 80]. The absorption by the electrons leads to their excitation which dramatically increases the gas pressure of the target material or even directly destroys the chemical bonds of the lattice. This leads to a rapid expanding gas which also drags parts of the target along. The emerging particles are further heated and accelerated by the incoming laser beam to form a plasma close to the surface. Above the surface the particles collide with each other and form the so-called KNUDSEN layer. Therefore, the velocity distri-

bution differs from the one caused by the pure ablation process. Beyond the KNUDSEN layer a region of 'free flight' follows up to the substrate with nearly no collisions. After having left the target the flying particles are visible as a fluorescent plume (Fig. 3.1b) which consists of electrons, ions, atoms, molecules, clusters, solid particles and molten droplets. The plume is directed perpendicular to the target surface. Its size and shape are determined by the energy and energy density of the laser light as well as by the pressure and composition of the background gas. A certain pressure of reactive gas is used in PLD to retain volatile components and to thermalise the plume. After the flight period the particles arrive on the substrate, which is usually heated to improve the surface diffusion, and form a film.

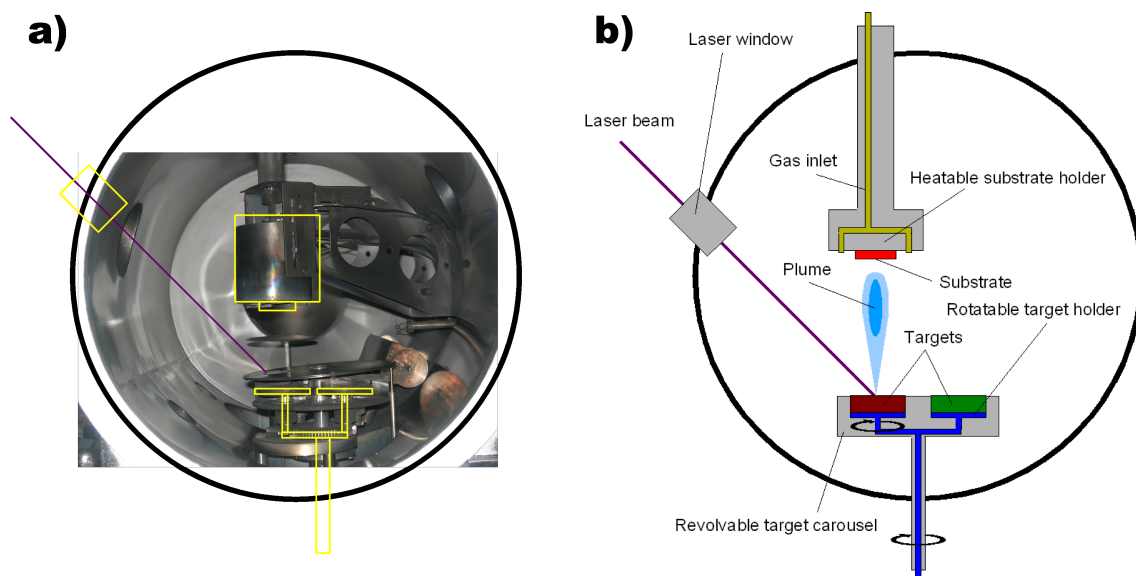


Figure 3.1: Image of the PLD chamber which is used in the frame of this work. The constituent parts shown in **a)** are explained in **b)** showing a schematic drawing of the used PLD chamber including the descriptions of all important parts.

Laser

Usually, laser radiation with a short wavelength is applied in PLD. This has the advantage of an improved light absorption as well as a smaller penetration depth for the materials relevant in this work. Therefore, only thin layers of the target are ablated which reduces both the probability of splashing and the energy density (fluence) necessary for ablation, which contributes to a more controlled ablation process. A further reduction of the number of too large particles takes place as they are partially dissolved when some of the laser light is absorbed by the plume [81].

Excimer lasers deliver radiation in the ultraviolet range [82]. They work with a gas which is in the simplest case pumped by electric discharges. Two components are excited to form the excimer molecule in the presence of a buffer gas. The ground state is repulsive which causes the excimer molecule to dissociate rapidly and allows high repetition rates.

Possible excimer molecules are F_2 , ArF , $KrCl$, KrF , $XeCl$ and XeF . Lasers which use KrF as excimer molecule have a very high gain and consequently this kind of laser is most commonly used.

The energy profile within the beam has to be as homogeneous as possible to enable a well-defined ablation. This is mainly given by the design of the laser but it can be improved by the use of an aperture. To have an effective conversion of energy to the lattice of the target, the pulse duration has to be in the order of nanoseconds. Otherwise the thermal conduction would carry away increasing parts of the energy. Furthermore, the laser energy plays a crucial role for the ablation mechanism. If the energy deviates from the optimum regime, the composition of the ablated material would change. Moreover, when the laser energy is reduced to a level which is not sufficient to completely vaporise the ablated material this leads to a higher number of particles in the plume. Even lower energies result in a considerable drop of the ablation rate with a smaller number of particles [83]. The threshold fluence for PZT was estimated to be $0.3 \frac{J}{cm^2}$ [84]. Much higher energy densities cause a larger number of high energetic particles which might damage the film surface.

The rate of ablated material is also controlled by the repetition frequency of the laser. If the amount of ablated material is not sufficient to form a continuous film this leads to the creation of pinholes. Too much material does not allow the surface atoms to diffuse to equilibrium positions and outgrowths of fast growing crystal faces can be observed [85]. The repetition rate of the laser pulses determines the time for the material to equilibrate between the arrival of the vapour pulses. The duration of the vapour pulses was estimated to be approximately 1 ms [86]. Finally, the laser fluence has to be adjusted according to the used film and substrate properties to enable the optimum growth regime (step-flow growth or layer-by-layer growth). Different growth regimes were determined theoretically and verified experimentally for the growth of SRO on STO [87].

Target

In principle any kind of target can be used for ablation by a laser beam. However, to grow films in a controlled manner, the target has to be dense and homogeneous with a smooth surface to avoid extensive particle formation. During the ablation process the laser radiation might change the surface properties of the target. Volatile components could be ablated at a higher extent. In this case the composition of the surface differs from the bulk of the target. The remaining components would shield the material behind and thereby cones would be formed (Fig. 3.2a). As a result, the target is irregularly ablated [88, 89].

Background gas

A higher gas pressure than in methods like molecular beam epitaxy ($10^{-2} Pa$) [90] is used during PLD ($10 Pa$). Oxygen is used as a reactive background gas for the deposition of *PZT*. This helps retaining the volatile components in the target and the growing film in two ways, viz. due to the basic physical effect of a higher background gas pressure and because the vapour pressure of the used metals decreases when they are oxidised. Additionally, the species in the plume are scattered at the gas molecules and are slowed down. This is necessary to avoid damaging of the substrate and film surface by high energetic particles. Due to the collisions of the particles with the oxygen atoms, lead oxide *PbO* is formed as a precursor for the formation of the film [84]. The higher reactivity of the oxygen compared to the other components also facilitates the nucleation of the arriving atoms on the surface. In order to further improve the reactivity of the oxygen atmosphere the pressure could be increased. This in turn leads to a lower deposition rate, so a compromise has to be found.

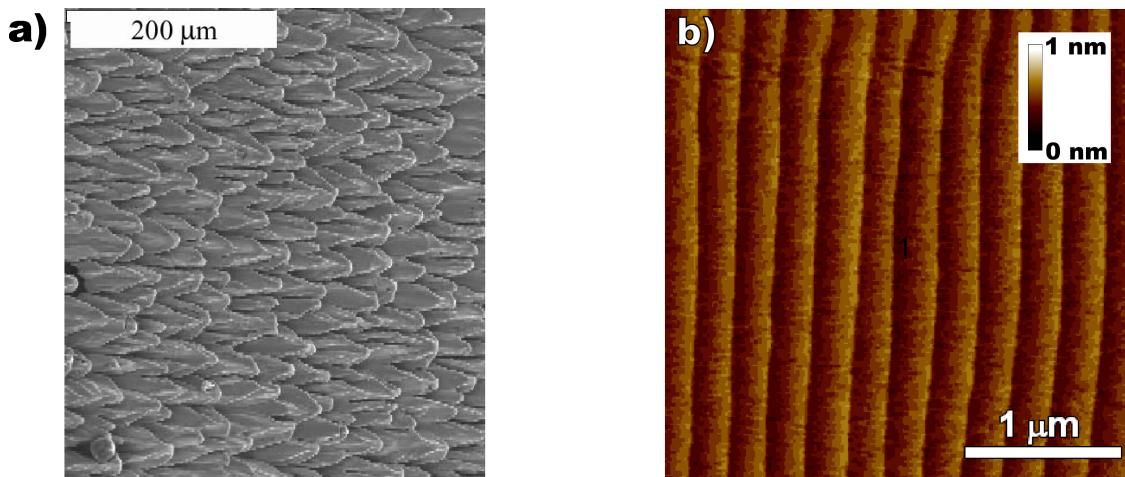


Figure 3.2: a) Example for cone formation on an Yttrium Iron Garnet target caused by the irradiation with laser light [89]. b) Stepped surface of an etched and annealed vicinal (100) *STO* substrate.

Experimental setup

An image of the deposition chamber and its components is given in Fig. 3.1. The employed excimer laser (LPX300 by Lambda Physics) uses *KrF* as the excimer molecule and *Ne* as a buffer gas. The laser emits light at a wavelength $\lambda = 248 nm$ which corresponds to a photon energy of about $5 eV$. This is higher than the band gap of about $4 eV$ of *Ti*-rich *PZT* which allows the ablation of this material by electronic excitation. The pulse duration provided by the used laser is $25 ns$. The beam is sent through an aperture to cut off the lower energetic edges and get a more homogeneous energy profile of the beam. After being reflected by a mirror, the beam passes the *laser window* of the chamber and is

focused on a ceramic *target*. The targets are positioned on a revolvable four-*target holder* and can be rotated to allow in situ change of the deposited material. The chamber is filled with oxygen via a *gas inlet*. The substrate is mounted above the target on a *heatable holder* at a distance from the target of 5.5 cm. Several accessible parameters have to be adjusted for the optimisation of the film growth in the described setup.

Laser adjustment: The repetition rate of the laser pulses is kept at 5 Hz for all ablated materials. This gives the material a time of about 200 ms to equilibrate between the arrivals of the vapour pulses. In the case of PZT the laser beam was sent through an attenuator. Measurements of the laser energy density (fluence Φ) are performed inside the deposition chamber. Laser fluences of 1.4 and 2.8 $\frac{J}{cm^2}$ were used, depending on the ablated material (Tab. 3.1), which causes the plasma *plume* to cover about 80% of the target-to-substrate distance.

Target preparation: Disc-shaped ceramic targets with a diameter of 50.8 mm and a thickness of 3.175 mm have been used. According to the specifications of the manufacturer (PRAXAIR) the purity is at least 99.9%. To avoid an extensive surface modification the target is sanded and a preablation is performed preliminary to each deposition. Since the favoured evaporation of volatile components cannot be fully inhibited, the PZT targets contain 10 % excess of Pb.

Gas pressure: An oxygen pressure of 14 – 30 Pa was used during deposition of the different materials.

deposited material	target density $\left(\frac{g}{cm^3}\right)$	laser fluence $\left(\frac{J}{cm^2}\right)$	oxygen pressure (Pa)	substrate temperature (°C)
<i>SRO</i>	3.72	2.8	14	700
<i>PZT20/80</i>	7.42	1.4	30	575
<i>PZT20/80:Cr</i>	7.48	1.4	30	575
<i>PZT40/60</i>	7.70	1.4	30	575

Table 3.1: List of deposited materials with corresponding target properties and PLD parameters.

Substrate preparation: To achieve smooth films with a very high crystal quality, layer-by-layer growth is necessary. The optimum mode to reproduce a regular surface is the step-flow growth which is only possible for small misfits as for *SRO* on *STO*. Step bunching would lead to enlarged and irregular terraces whereas coalescing islands often cause antiphase boundaries. To enable step-flow growth, a substrate with steps of equal width and height, a so-called vicinal substrate, is required. Vicinal *STO* substrates with a miscut angle of 0.1° are used throughout this work. Initially, the surface is not uniformly termi-

nated but exhibits a stochastic mixture of both strontium oxide SrO and titanium dioxide TiO_2 as termination. Therefore, a special treatment of the surface is required. The STO is etched in buffered hydrofluoric acid with a pH -value of 4.4...4.6 to dissolve only the basic SrO and spare the acidic oxide TiO_2 [91]. This results in a TiO_2 -terminated surface with steps of one unit cell height. The substrate is then annealed at 900 – 1100°C for 1 – 2 h, depending on the substrate's terrace width, in order to smoothen out possible defects from the etching process and to adjust the terrace edges to a nearly parallel shape [92]. This procedure provides a regular substrate surface as shown in Fig. 3.2b.

During the film deposition the substrate is kept at elevated temperature. The chosen temperature depends on the growing material (Tab. 3.1). This increases the diffusion length of the deposited atoms and allows to grow single crystalline films but also slightly increases the evaporation of the volatile component [84]. Without the substrate heating, the sample had to be annealed after deposition which could result in a polycrystalline or textured film.

3.2 Characterisation methods

3.2.1 Scanning probe microscopy

Atomic force microscopy: Atomic force microscopy (AFM) is used to map the topography of surfaces by utilising attractive and repellent atomic forces. A sharp tip carried by a deformable cantilever is approached to the sample. When the distance to the surface is small enough, attractive van der Waals forces pull the tip towards the surface. In ambient conditions capillary forces give an additional contribution to the attractive forces. If the tip is pushed closer to the surface the forces become repulsive. The tip is exposed to both attractive and repulsive forces during the scan across the investigated surface. This leads to a deflection of the cantilever if the height of the surface features changes or to a twisting if any frictional forces occur. A laser beam is reflected from the backside of the cantilever to detect such deformations. The beam reflection is measured on a four-quadrant photo detector. The height of the tip is adjusted to stay at zero deflection.

In contact mode, the force applied by the tip may damage the investigated surface. A way to avoid the damage is to use the so-called tapping mode. In this mode the cantilever is oscillating above the surface and just 'touches' the surface at its lowest point. The amplitude of this oscillation is tracked during scanning over the surface. Any surface features cause a shift of the oscillating amplitude and phase. A feedback loop corrects the position of the cantilever which is registered and the surface morphology is mapped. Any frictional forces are eliminated by this technique [93].

From the AFM images the root-mean-squared roughness RMS is calculated as a measure of the surface roughness:

$$RMS = \sqrt{\frac{1}{N} \sum_{i=1}^N (z_i - \langle z \rangle)^2}, \quad (3.1)$$

with N the number of measured coordinates, i the i 'th measured coordinate, z_i the height value of the measured coordinate and $\langle z \rangle$ the average of all N height values.

A Digital Instruments 5000 AFM equipped with a MikroMasch NSC15/AIBS silicon cantilever (with a spring constant of 40 Nm^{-1}) operating in tapping mode was used during this work.

Piezoresponse force microscopy: Piezoresponse force microscopy (PFM) is a modification of conventional AFM. A conductive tip is used to apply an alternating voltage to the sample. This leads to a deformation of a ferroelectric film via the converse piezoelectric effect which is measured as a deflection of the cantilever. The frequency of

the deflection caused by the piezoresponse is known and can be subtracted from the overall topography signal (lock-in principle). Different deflection amplitudes and phase shifts are obtained, depending on the polarisation of the film. If the polarisation is pointing away from the tip a positive voltage causes an expansion of the film. The oscillations are in phase with the applied alternating voltage. If the polarisation is pointing towards the tip this causes a phase shift of 180° . In case of a polarisation perpendicular to the applied field, as in the case of a-domains in tetragonal ferroelectrics, in the first approximation the applied voltage does not lead to any deformation of the film, and the measured PFM amplitude equals zero [94]. Certain in-plane polarisation components can, however, be detected via shear deformation of the cantilever.

In this work PFM was performed using a scanning probe microscope (ThermoMicroscopes) equipped with a PtIr coated tip (ATEC-EFM-20) with an elastic constant of about $2.8 Nm^{-1}$. Surface mapping and local hysteresis measurements were usually carried out applying an ac probing voltage of 2 V at 25 kHz.

3.2.2 Transmission electron microscopy

Transmission electron microscopy (TEM) is a powerful tool to image the microstructure of crystals. Crystal features like deformations and extended defects such as dislocations and stacking faults can be easily observed. In this work a Philips CM20Twin was operated at an acceleration voltage of 200 kV to observe conventional TEM images. The high resolution TEM images (HRTEM) and high resolution scanning TEM images (HRSTEM) were obtained using a JEOL 4010 and a FEI TITAN 80-300 at a working voltage of 400 kV and 300 kV, respectively.

Working principle

The working principle of transmission electron microscopy is comparable to an optical microscope in transmission mode. Instead of a lamp an electron source is used and the lenses are made of coils generating an electromagnetic field which is used to manipulate the electron's path (Fig. 3.3). The resolution of both transmission optical and electron microscopes is principally limited to features of the size of the used wavelength. However, the limiting factor in TEM are the lens aberrations. Nevertheless, a rather high resolution can be achieved due to the short wavelength of electrons accelerated by several hundred kilovolts.

When electrons hit a sample, due to their electric charge they interact mostly with the nucleus of the atoms. If the sample is crystalline, a diffraction pattern is created due to constructive interference under the conditions given by BRAGG's Law

$$n\lambda = 2d \sin \theta \quad (3.2)$$

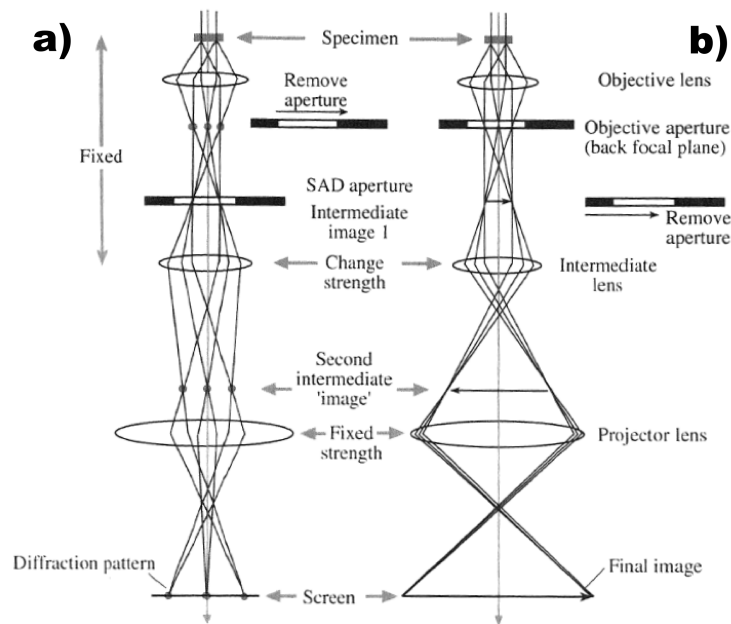


Figure 3.3: Paths of the electron beams in the TEM [95]. **a)** shows the operation mode if the diffraction pattern shall be projected on the screen whereas **b)** shows the operation mode to view the magnified image of the sample. The selected area diffraction (SAD) aperture is used to obtain a diffraction pattern of a small area of the sample. The objective aperture is necessary to create an amplitude contrast in the image (details in Fig. 3.4).

where n is a number, λ the wavelength of the electrons, d the distance of the diffracting planes and θ the angle between the incident wave and the scattering plane. Depending on the excitation of the intermediate lens, either the diffraction pattern (Fig. 3.3a) or the image (Fig. 3.3b) of the sample is projected on the screen.

A selected area diffraction (SAD) aperture has to be inserted if the diffraction pattern should be obtained from a defined part of the sample. Since it is not possible to insert an aperture at the location of the sample, the SAD aperture is inserted into the image plane of the objective lens. In order to create an amplitude contrast an objective aperture is used (Fig. 3.3b). In diffraction-contrast mode, the objective aperture offers two different kinds of images. Firstly, the residual electrons of the direct beam give rise to the so-called bright field (BF) image, if the scattered electrons are absorbed by the aperture (Fig. 3.4a). Secondly if the aperture is positioned in such a way that the direct beam is absorbed (Fig. 3.4b) and the scattered electrons are allowed to pass, they form the dark field (DF) image. The diffraction pattern is utilised to adjust the position of the objective aperture. The aperture has to be placed on the bright central spot to obtain a BF image (Fig. 3.5a). One of the smaller diffraction spots representing a certain crystal plane has to be chosen and let pass by the aperture (Fig. 3.5b) in order to obtain the DF image. If the diameter of the aperture is large enough to include both the direct beam and some of the scattered beams (Fig. 3.5c) they will interfere with each other. This will create a phase contrast which is used to generate HRTEM images. If a scanning transmission

electron microscope with high enough lateral resolution is available, single atom columns can be resolved in high-angle annular dark field (HAADF) images (Z-contrast images) which make use of incoherent scattering events at the nuclei of the atoms, providing high resolution scanning TEM (HRSTEM) images.

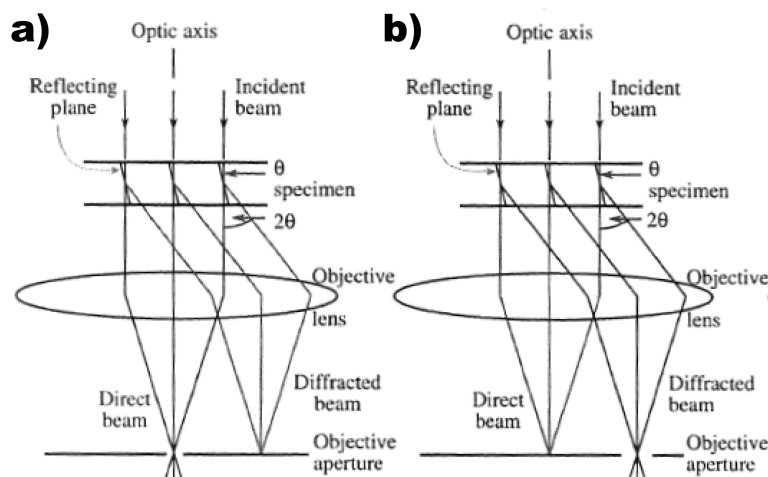


Figure 3.4: First part of the electron beam path in TEM when an image of the sample is displayed [95]. **a)** If the objective aperture lets only the direct beam pass, a so-called bright field image is detected. All the diffracted electrons generate the dark contrast. **b)** By letting the diffracted electrons pass, a dark field image is displayed. Only the collected diffracted electrons are visible as the bright parts of the image.

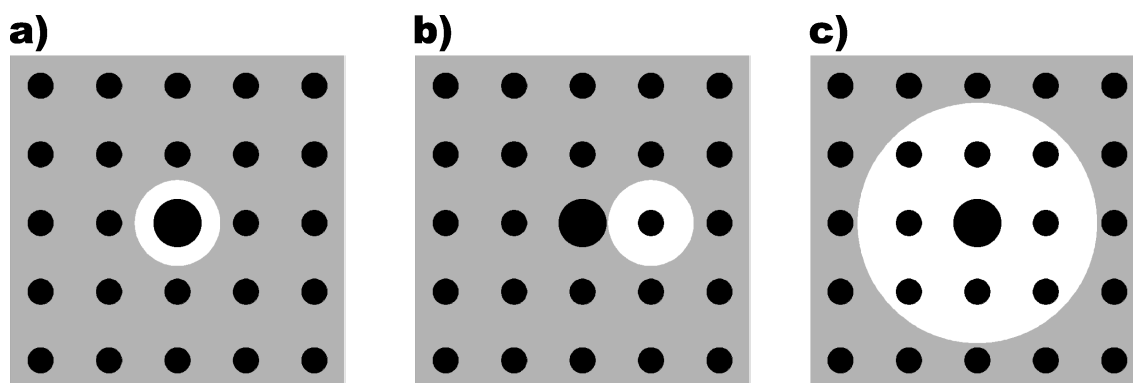


Figure 3.5: Objective aperture as seen in the diffraction pattern. The big dark spot designates the direct beam whereas the small spots depict the diffraction pattern of different crystal planes. **a)** If the aperture lets the electrons of the direct beam pass, all diffracted electrons are prevented from contributing to the image. **b)** If the aperture lets one diffracted beam pass, only the electrons diffracted at this certain plane are collected and contribute to the contrast in the image. **c)** If a big aperture is used which lets the direct beam and diffracted beams of various planes pass, the beams will interfere with each other. This generates a phase contrast which allows to create a HRTEM picture.

Sample Preparation

To prepare the samples for cross-section (HRS)TEM, they are cut in two pieces of equal size and glued face-to-face using M-Bond 610 epoxy resin. The glued sample is annealed for 90 min at 150 °C under the constant pressure of a clamp. Afterwards it is cut in slices of 0.5 mm thickness and sanded and polished down manually to a thickness of 50-80 μm . Next the thickness of the slices is further reduced to 10-15 μm with a dimple wheel and a polishing wheel attached to a Gatan Model 656 dimple grinder. Subsequently the sample is glued to a *Mo* oval grid using a two-component epoxy resin which has to harden for 12 h. Supported by this grid, the sample is put into a Gatan Model 691 PIPS dual ion mill wherein the sample is thinned from one side by Ar^+ bombardment. The ion energy is reduced from 4 keV to 2 keV to avoid a destruction of the sample during thinning. When a transmittable area becomes apparent the energy is reduced to 1.5 keV and the sample is polished from both sides to complete the preparation.

3.2.3 X-ray investigations

X-rays are part of the electromagnetic spectrum with a wavelength of 0.01 - 10 nm. They are used in various ways to analyse many kinds of materials [96, 97]. In X-ray fluorescence spectroscopy, for example, high energetic radiation excites X-rays to map the elemental and chemical composition of the investigated sample.

Other applications use the high penetration ability together with the changing absorption which depends on the atomic number and material defects. This allows radiography in many areas from medicine to materials testing.

However, the utilisation in this work concerns mainly the X-ray diffraction. Since the wavelength is in the same order as the atomic radii and the interatomic distances, the X-rays are diffracted and allow a detailed analysis of the crystal structure. It is possible to determine the orientation of crystals, their lattice constants and - to a certain extend - their composition by a comparison of the results with the existing extensive databases. Furthermore, also distortions of the crystal lattice like strains and textures can be observed.

X-ray diffraction

X-rays are created by decelerating high energetic electrons at the anode. A continuous spectrum is created if the electric field of the materials' atomic nuclei decelerates the electrons. Another energy loss process of the fast electrons is to knock out an electron on the inner shell of a target atom. When this place is refilled by an electron from an upper shell, it emits an X-ray photon having an energy according to the energy difference between the shells. This is called the characteristic radiation because the energy difference between the shells and therefore the wavelength of the characteristic line is specific to each element. The emitted photon is called the *K* radiation if an electron relaxes to the *K*-shell.

3 Experimental

If the transition takes place from the nearest higher shell the index α is used, if it comes from the next one β is used and so on. Finally, the index gets a number depending on the change of the inner quantum number j . The transition with the highest energy is provided with a 1 and the number increases with decreasing energy. The investigations described here are performed using the $CuK_{\alpha 1}$ radiation ($\lambda_{CuK_{\alpha 1}} = 0.1541 \text{ nm}$) [98] which is not separated from the $CuK_{\alpha 2}$ radiation ($\lambda_{CuK_{\alpha 2}} = 0.1544 \text{ nm}$) because their energies are very close.

CuK_{α} radiation with both wavelengths is sent on the sample and scattered. This process is called elastic scattering if the frequency of the wave does not change, because the wave preserves its energy. A coherent scattering is defined by a fixed phase correlation between scattered and unscattered wave. If an elastic and coherent scattering takes place on a periodic structure this is called diffraction. A signal can be detected only if there is a constructive interference which takes place at distinct angles described by BRAGG's law (Eq. 3.2). The intensity of these diffraction peaks depends on the atomic number of the elements and on the arrangement of the atoms in the unit cell. Both parameters change the electron configuration which determines the contribution to the scattering process. The diffraction pattern is unique for each material.

A four-circle Philips X'Pert material research diffractometer (type 3050/65, 50 kV and 30 mA, CuK_{α} radiation) was used to analyse the samples grown by PLD. The setup of this X-ray diffractometer is shown in Fig. 3.6a. Preliminary to each measurement the

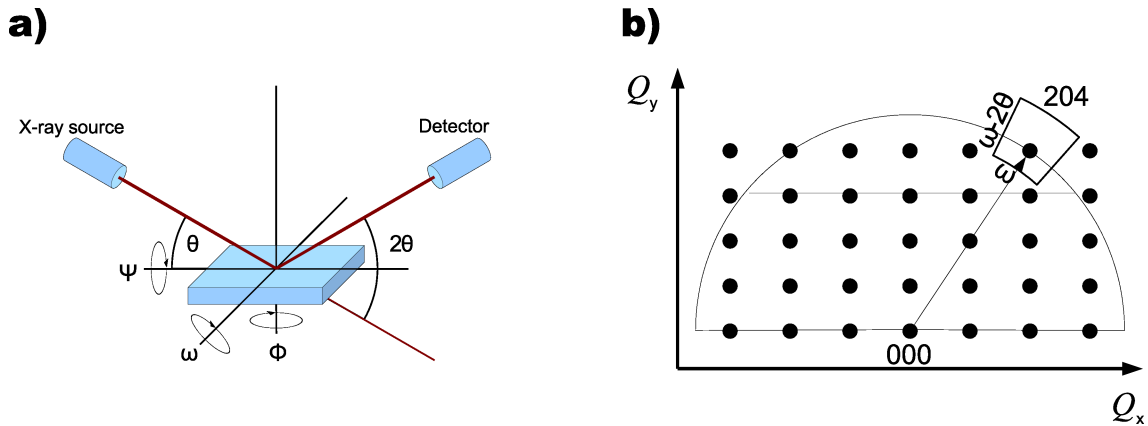


Figure 3.6: a) Setup of the used X-ray diffractometer. θ designates the angle between the surface and the incident beam. The sample can be tilted in the plane of the beam by varying ω and in both perpendicular directions with the help of Φ and Ψ . b) Principle of mapping the reciprocal space around the (204) diffraction spot. The reciprocal plane is spanned by varying ω and 2θ .

angles ϕ and ψ were used to optimise the orientation of the sample to get the maximum possible intensity. In order to investigate the crystal structure of the films, $\theta - 2\theta$ scans were performed which were realised in the used setup by rotating the sample around ω and changing 2θ by moving the detector. A more sophisticated method to investigate thin films is the recording of reciprocal space maps (RSM). This is usually done in the vicinity of a diffraction peak of the substrate (Fig. 3.6b). By carrying out many consecutive $\omega - 2\theta$

scans, whereby the starting value of ω is increased, the chosen area of the reciprocal space is mapped.

Energy-dispersive X-ray spectroscopy

The usage of an energy dispersive X-ray detector together with a TEM or scanning electron microscope (SEM) allows the determination of the energy of the X-ray photons that are emitted from the sample due to the incoming beam electrons. It is possible to identify the elements of the irradiated target from the detection of the characteristic radiation. This paves the way for a method to analyse the elemental composition of materials, called energy-dispersive X-ray spectroscopy (EDX) [96, 99]. Most SEMs and many TEMs are equipped with an EDX detector allowing the elemental analysis of the investigated sample.

3.2.4 Electrical measurements

Circular and square-shaped *Pt* top electrodes with a diameter of about $100\ \mu\text{m}$ and a side length of $60\ \mu\text{m}$, respectively, were deposited at room temperature by radio frequency sputtering through a corresponding stencil. Silver paste was used to connect the SRO bottom electrode with a copper plate. Both the copper plate and the top electrode were contacted by *W* tips with the help of a micromanipulator. Ferroelectric hysteresis curves were recorded at $1\ \text{kHz}$ (AixxACT TF Analyzer). Capacitance-voltage characteristics were recorded at $100\ \text{kHz}$ with a probing voltage of $0.1\ \text{V}$ (HP4194A Impedance Analyzer). The superimposed dc bias had a slope of about $1\ \text{V}\ \text{s}^{-1}$ and the delay time between slope up and down was $0.5\ \text{s}$. The values at zero voltage were used to calculate the equivalent dielectric permittivity using the simple plan-parallel capacitor model. Current-voltage characteristics were recorded using a Keithley 6517 with the voltage applied in the direction of the polarisation to avoid contributions due to the switching process. The voltage was applied for $2\ \text{s}$ before measuring the current.

3.2.5 Rutherford backscattering spectroscopy

Rutherford backscattering spectroscopy (RBS) is a nondestructive analytical technique to determine the composition of surfaces and layers up to a few micrometres. In RBS low-*Z* ions (H^+ or He^+) are accelerated with energies in the MeV range and directed towards the sample. The backscattered ions are detected and analysed in view of the residual energy which is influenced by the scattering process and the scattering angle. Two different processes reduce the energy of the ions with respect to the incoming beam. If the ions are scattered at an atomic nucleus they will lose a certain amount of energy which depends on the mass of the nucleus. This allows the identification of the elements in the sample.

Additionally, the ions are decelerated by the sample electrons. With increasing depth of the scattering core the energy will continuously decrease. The depth of the scattering process can be determined from the energy difference which enables to create a depth profile of the sample's composition [100].

RBS investigations were performed in cooperation with Dr. R Mattheis (IPHT Jena) at the 3MVTandetron accelerator JULIA at CISLAB, Friedrich Schiller University Jena, using ${}^4\text{He}^+$ ions with a primary energy of 1.4MeV . RBS spectra were simulated with the iterative simulation software RUBSODY [101].

3.2.6 Electron paramagnetic resonance

Electron paramagnetic resonance (EPR) is able to detect only non-paired electrons of atoms or ions. All atoms and ions with paired electrons do not contribute to the signal which strongly limits the application of this technique. However, at the same time this allows a very specific detection of responding atoms and ions. These properties make EPR an adequate method to investigate point defects. In EPR the sample is exposed to a magnetic field in the order of several Tesla. In the magnetic field the degeneracy of the electrons' energy levels is lifted and the latter split with respect to their magnetic quantum numbers. The developing energy gap ΔE has a magnitude of

$$\Delta E = g_e \mu_B B \quad (3.3)$$

with g_e the LANDÉ factor, μ_B the BOHR magneton and B the applied magnetic field. Unpaired electrons can surpass this energy gap if excited by electromagnetic waves which fit the condition

$$hf = \Delta E. \quad (3.4)$$

Here h is PLANCK's constant and f the frequency of the electromagnetic radiation. An additional splitting is caused by the interaction among the electrons, giving rise to the so-called fine structure. The local fields σ modify the experienced magnetic field which is taken into account by modifying g_e that becomes the so called g -factor

$$g = g_e (1 - \sigma). \quad (3.5)$$

The g -factor is smaller than g_e if the according shell is less than half filled and it will be larger if more than half of the shell is filled. In EPR measurements the frequency of the radiation is kept constant and the magnetic field is varied. An absorption peak is observed if the energy gap fits the frequency. The determined g -factor is characteristic for every element in a certain valence state. The fine-structure interaction can be described by a Hamiltonian containing the fine-structure (FS) tensor. From the symmetry of the tensor the local site symmetry of the paramagnetic ion can be concluded [102].

240 GHz EPR measurements were performed in cooperation with Dr. R.-A. Eichel (TU Darmstadt, now University of Freiburg) at the National High Magnetic Field Laboratory (NHMFL) on a spectrometer invoking a quasi-optical setup without resonator [103]. Microwave radiation was provided by the multiplied output of a Gunn oscillator. Heterodyne signal detection allowed full control of the signal phase [104]. The setup of the thin film oriented with its crystalline c -axis parallel with respect to the magnetic field results in an orientation-selective measurement of only the parallel components of the spin-Hamiltonian parameters. Calculations employing the semi-empirical NEWMAN superposition model (NSM) [105] were performed by Dr. E. Erdem (University of Freiburg). Alternative information on the defect structure was obtained from DFT calculations by Dr. P. Erhart (Lawrence Livermore National Laboratory). The corresponding calculations within the local spin density approximation were carried out using the projector-augmented wave method as implemented in the Vienna ab-initio simulation package [106, 107].

4 Results

This chapter deals with the results obtained on ferroelectric epitaxial heterostructures. The aim is to understand the impact of interfaces on the properties of tetragonal *PZT* films. Firstly, in Section 4.1, the electrode layer and single composition ferroelectric films are analysed to be able to distinguish between intrinsic properties of the investigated materials and extrinsic properties induced by the design of the heterostructure. Subsequently, two ferroelectric layers are combined to create an interface within the ferroelectric film which will be addressed in Section 4.2. Moreover, the influence of doping is examined in Section 4.3. Later on the number of interfaces will be systematically increased within Section 4.4.

PZT20/80 is known to grow epitaxially on *STO* [108] making it possible to largely exclude extrinsic influences and concentrate on the intrinsic properties. A similar material is needed to purposely create artificial interfaces in the ferroelectric film and simultaneously avoid to introduce too many new properties into the system. It would be much more difficult to interpret any data in terms of interface effects, if there had been a lot of other influences caused by a very different material system. Therefore, *PZT40/60* is chosen which is another composition of the solid solution system *PZT* and consequently is very similar to *PZT20/80*. It is also tetragonal and its ferroelectric properties are close to the ones of *PZT20/80*. The small difference in the lattice constants is expected to be sufficient to introduce a clearly discernible interface in any geometrical arrangement that combines these two compositions.

4.1 Properties of single composition films

As mentioned in Section 2.1, the investigated heterostructures consist of the substrate *STO*, the perovskite electrode *SRO* and a ferroelectric film of *PZT20/80* or *PZT40/60* or a combination of them. Dislocations are formed at growth temperature (given in Tab. 3.1) during deposition of the films. The resulting density of dislocations depends on the mismatch of the lattice parameters of the film and the underlying material at this temperature. Different thermal expansion coefficients of the layers may create additional stresses during cooling down to room temperature. Therefore, the knowledge on temperature dependence of the lattice parameters of both substrate and film material is crucial to understand the properties of the final film. The lattice parameters change severely between growth

temperature and room temperature. Since both *STO* and *SRO* are considered as cubic, the corresponding lattice parameters vary more or less linearly with temperature by thermal expansion. In contrast, the used ferroelectric *PZT* compositions undergo a phase transition at T_C from cubic to tetragonal (Fig. 2.4a). This is accompanied by a splitting of the single lattice parameter into two different ones. A pseudocubic lattice parameter can be extrapolated down to room temperature from the linear temperature dependence of the *PZT*'s lattice parameters above T_C , using the thermal expansion coefficients [109]. The tetragonal lattice parameters can be deduced with the help of the equations which describe the effect of the spontaneous strain [110]:

$$a = a_{pc} + a_{pc}Q_{12}P_S^2 \quad (4.1)$$

$$c = a_{pc} + a_{pc}Q_{11}P_S^2. \quad (4.2)$$

Here, a and c are the tetragonal lattice parameters whereas a_{pc} is the pseudocubic lattice parameter, Q_{ij} the electrostrictive coefficients and P_S the spontaneous polarisation. The spontaneous polarisation can be calculated from the minimisation of the free energy. To calibrate the results they are adjusted to fit the known room temperature a -axis lattice parameters [40, 41, 48, 50, 51]. The temperature dependent lattice parameters of all materials under consideration are shown in Fig. 4.1. A slight deviation between

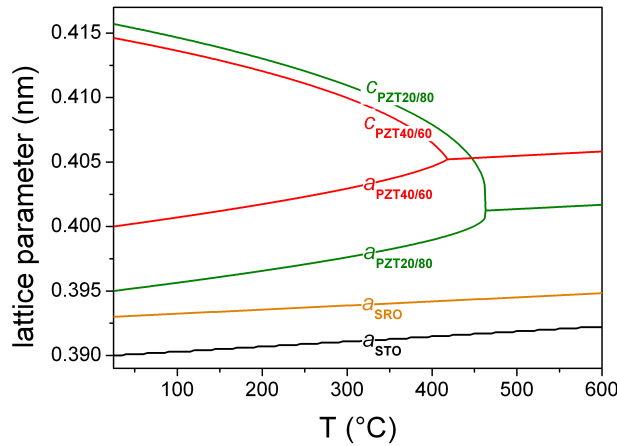


Figure 4.1: Non-strained lattice parameters of the materials used for PLD in dependence on temperature. *PZT20/80* and *PZT40/60* become ferroelectric below the Curie temperature and their cubic lattice parameter splits into the two tetragonal ones.

the calculated and the experimental c -axis lattice parameters is observed ($\Delta c_{PZT20/80} = 0.0009 \text{ nm}$, $\Delta c_{PZT40/60} = 0.0004 \text{ nm}$) which might result from the small discrepancy between the used parameters obtained by different authors. This deviation is small enough to neglect its influence on the deduced quantities. The misfit f (Eq. 2.2) can be calculated at any temperature from the difference of the lattice parameters. It is important to keep in mind that the misfit at growth temperature determines the corresponding critical thickness

h_C (Eq. 2.6) above which MDs are introduced. One important base which is common to all described ferroelectric films is the *SRO* bottom electrode. Therefore, the aim is to avoid the formation of dislocations in this layer. In the following the necessary conditions are discussed.

Bottom electrode layer: SRO

Prior to the deposition of all *PZT* films, the *SRO* bottom electrode has to be deposited to enable electrical characterisation of the sample. The surface of the *SRO* layer determines the growth and thereby the resulting crystal structure of the subsequent ferroelectric film. Therefore, the *SRO* surface should exhibit regular straight terraces of a uniform width which reflects the vicinal surface of the substrate. This can be realised only if the *SRO* grows in the step-flow mode and if the structural quality of the *SRO* layer is very high.

SRO has a very small misfit of $f = -0.55\%$ (at 700°C) to the *STO* substrate. In order to decide which of the Eqs. 2.6 or 2.7 has to be used, the boundary conditions of the *SRO* layer have to be considered: since the *SRO* layer is covered by (at least) one further layer, the strain can be shared between the layers, and MDs are allowed to occur on two interfaces. Therefore it is Eq. 2.6 that gives the correct value of the critical thickness. Due to this equation, it is possible to grow an *SRO* layer pseudomorphically up to a critical thickness $h_C \approx 80\text{nm}$ without the formation of misfit dislocations. Experimentally the growth of coherently strained *SRO* was shown for a thickness up to 75nm [73]. Depending on the deposition parameters, different growth modes are observed. As it was theoretically predicted and experimentally confirmed [87] the PLD growth regime for *SRO* depends on the flux of the incoming atoms as well as on the temperature and the terrace width of the substrate (see Fig. 4.2). In the present work the terrace width of the used substrates

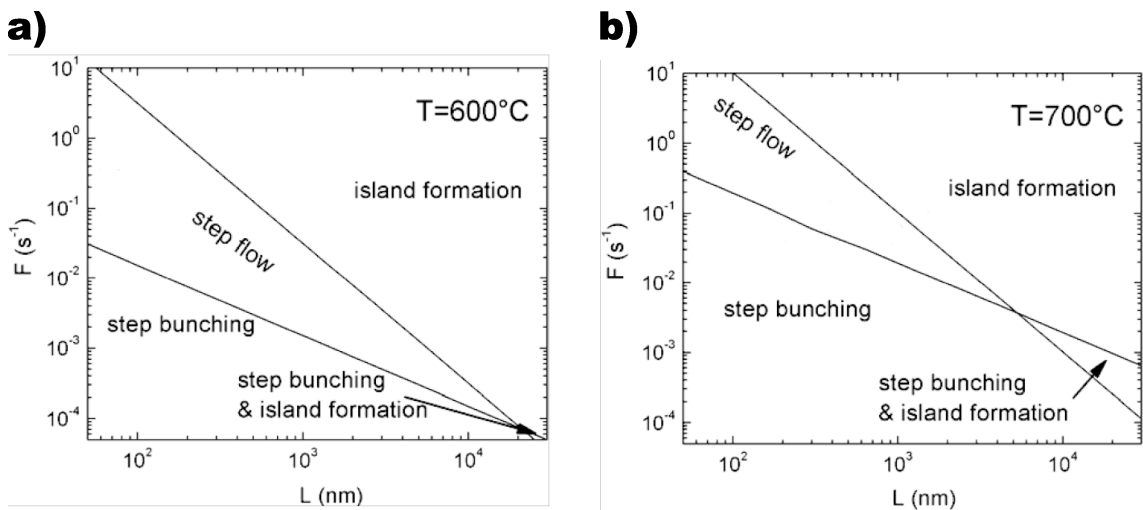


Figure 4.2: PLD growth regimes in dependence on the flux F of incoming atoms and the terrace width L of the substrate at **a)** 600°C and **b)** 700°C , after [87]. It can be seen that the desired step flow growth is limited to a small region in between step bunching and island formation.

varies only slightly from sample to sample, amounting about 200 nm which corresponds to a miscut of about 0.1° . The atom flux at a constant oxygen pressure (Tab. 3.1), target to substrate distance (5.5 cm) and repetition rate (kept at 5 Hz) was controlled by varying the energy density of the laser pulses (laser fluence Φ_L). Figure 4.3 displays the evolution of different growth modes with increasing laser fluence which are explained in detail in Section 2.2. At values of $\Phi_L \approx 2.4 \frac{\text{J}}{\text{cm}^2}$ the terraces of the *SRO* conglomerate leading to

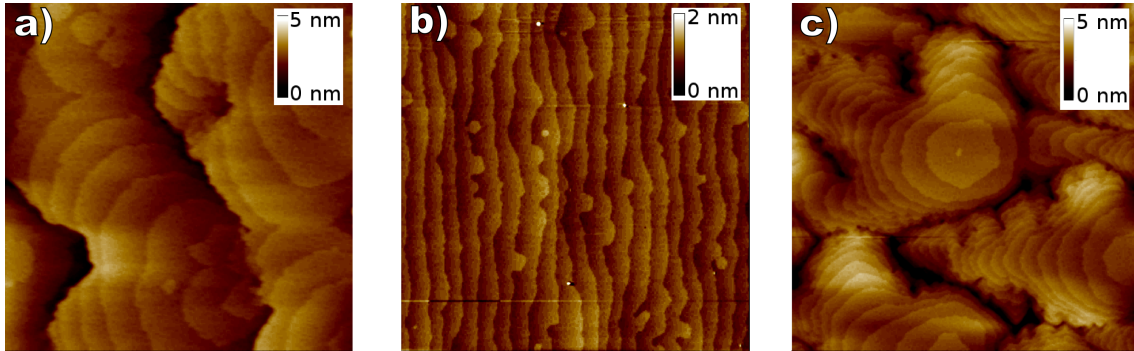


Figure 4.3: AFM images showing surfaces of 70 nm thick *SRO* films on a substrate with a terrace width of 200 nm , grown at a temperature of 700 C obtained from different growth modes generated by different laser fluences. The image size is $3\ \mu\text{m} \times 3\ \mu\text{m}$. With increasing laser fluence the growth mode changes from **a)** step bunching at $\Phi_L = 2.4 \frac{\text{J}}{\text{cm}^2}$ over **b)** step flow growth at $\Phi_L = 2.8 \frac{\text{J}}{\text{cm}^2}$ finally to **c)** island grow at $\Phi_L = 3.2 \frac{\text{J}}{\text{cm}^2}$.

the observed irregular structure typical for the step-bunching mode (Fig. 4.3a). According to the theoretical results, the energy (at the given terrace width and temperature of the substrate) is too low to achieve step-flow growth. At $\Phi_L \approx 2.8 \frac{\text{J}}{\text{cm}^2}$ the *SRO* grows in the step-flow (Fig. 4.3b) mode. In this growth mode the steps of the underlying *STO* substrate are reproduced. *SRO* has the best homogeneous microstructure with a regular surface. A further increase up to $3.2 \frac{\text{J}}{\text{cm}^2}$ leads to island growth (Fig. 4.3c). At these values of Φ_L the energy window for the step-flow growth at the given temperature and terrace width is already left. The atom flux is high enough to cause a nucleation at arbitrary points of the surface, the preferred nucleation at the step edges does no longer dominate the growth. Individual islands form, resulting in a rough surface topography.

As can be seen, the step-flow mode reproduces a regular surface at every step of the growth process providing the required *SRO* surface with regular terraces. The corresponding optimum PLD parameters for growing *SRO* films are used throughout the present work to prepare the bottom electrode. In this way the basis for a layer-by-layer growth of the subsequent *PZT* film is laid.

Ferroelectric layer: PZT40/60 and PZT20/80

The properties of the single composition ferroelectric films have to be investigated before any attempts can be made to understand more sophisticated systems.

Microstructure: As a useful side effect of the similar structural and physical properties of the two investigated *PZT* compositions, the same deposition conditions can be used (Tab. 3.1). The grown films exhibit a very smooth surface: AFM measurements reveal a surface roughness of $RMS \approx 0.252 \text{ nm}$ for the layer system consisting of the *SRO* bottom electrode and the ferroelectric *PZT40/60* layer (Fig. 4.4 a). In case of a *PZT20/80* layer, some outgrowths with a height of around 10 nm occur (Fig. 4.4 b). However, in between these outgrowths the surface roughness is as low as $RMS \approx 0.172 \text{ nm}$ and even some terrace-like structure induced by the substrate is still visible. Both the small roughness and the observed terraces indicate a highly controlled and homogeneous film growth for both compositions.

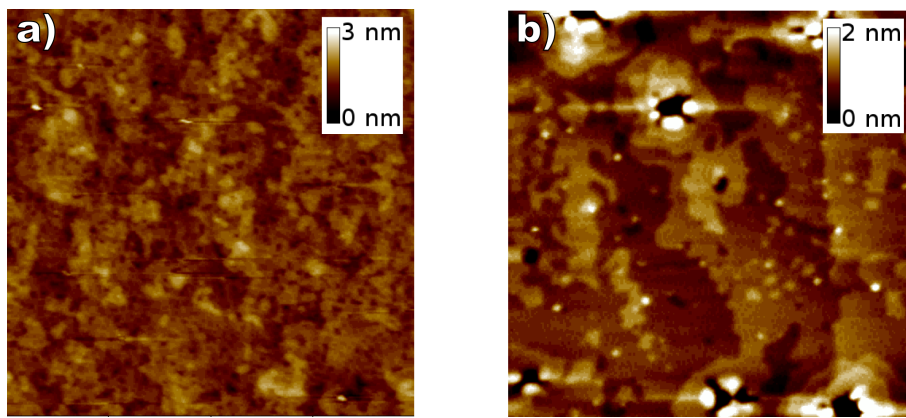


Figure 4.4: AFM images of the surface of **a)** a 100 nm thick *PZT40/60* and **b)** a 90 nm thick *PZT20/80* film. The image size is $1 \mu\text{m} \times 1 \mu\text{m}$. A very small roughness is observed for both films. In case of the *PZT20/80* film terraces induced from the substrate can be observed in between the outgrowths.

$\theta - 2\theta$ XRD scans were performed to examine the crystallographic orientation of the films. The resulting diffraction peaks are shown in Fig. 4.5. For *PZT* exclusively (00*l*) reflections occur. Several characteristics cause the details of the diffraction patterns: Firstly, both the *STO* substrate and the *SRO* electrode cause peaks very close to the ones associated with the *PZT*. This happens due to their crystallographic similarity for which they were chosen as parts of the heterostructures. The peaks are not well separated from each other but rather triples are observed, especially at low *l*. Due to the decreasing out-of-plane lattice constant of the used materials the diffraction peaks of *PZT*, *SRO* and *STO* occur always in this sequence. Secondly additional peaks occur stemming from the not completely suppressed $\text{CuK}\beta$ radiation (marked by # in Fig. 4.5), the polycrystalline top *Pt* electrode (*), a *W* contamination of the X-ray target (+) and the *Si* sample holder (%). From the sole occurrence of the (00*l*) reflection a highly oriented single crystalline structure of both *PZT* compositions can be derived with the tetragonal *c*-axis pointing out-of-plane.

The internal microstructure of the fabricated films is revealed by TEM investigations of cross-sectional samples as shown in Fig. 4.6. Firstly, the pictures provide the information

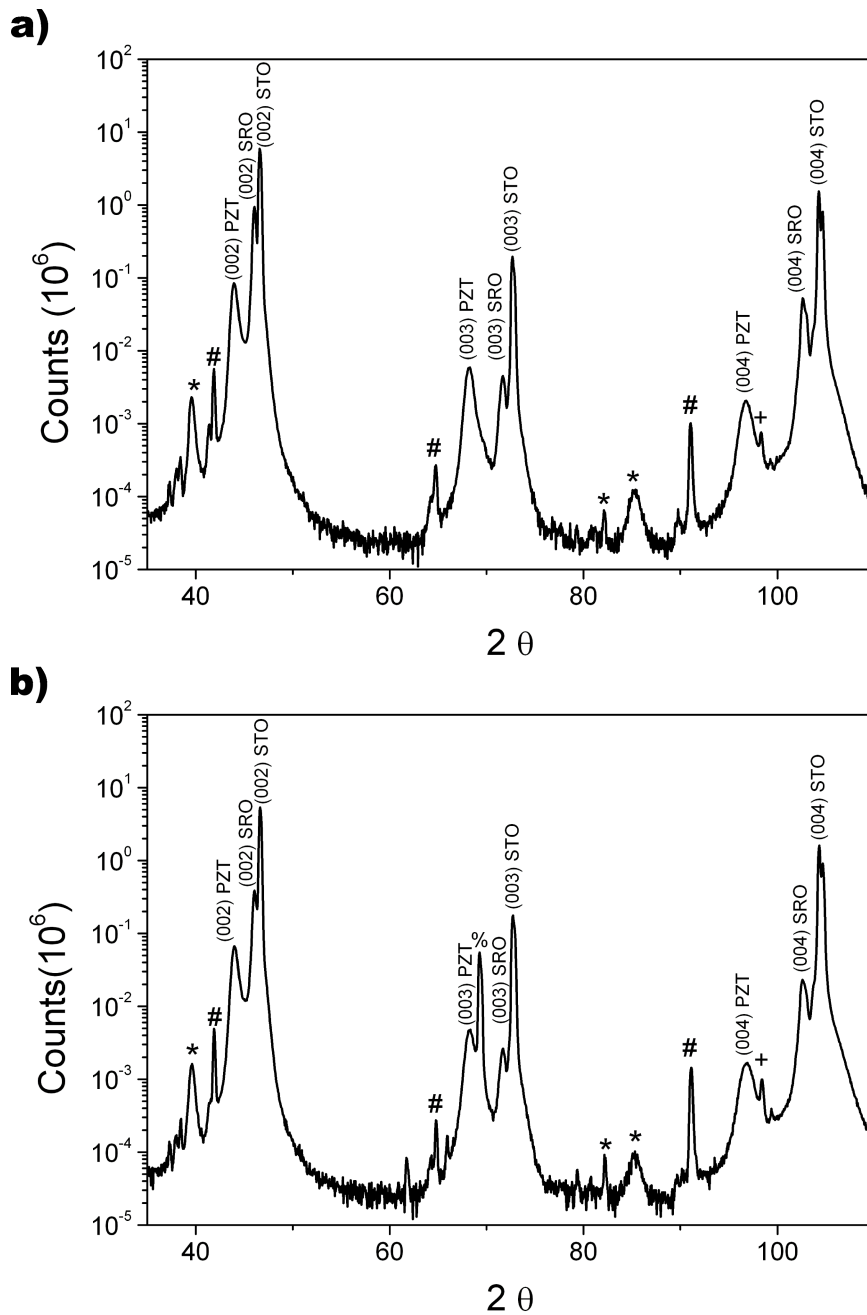


Figure 4.5: $\theta - 2\theta$ scan of a $Pt/PZT/SRO/STO$ heterostructure with **a)** a 100 nm thick $PZT_{40/60}$ and **b)** a 90 nm thick $PZT_{20/80}$ layer. The $(00l)$ peaks with $l = 2 \dots 4$ are indicated. The peaks are always triples consisting of diffraction peaks of PZT , SRO and STO (in this sequence). Additional peaks are visible which belong to the polycrystalline Pt top electrode (*), the remaining $CuK\beta$ radiation (#), the Si sample holder (%) and the W line (+) from a tungsten contamination of the X-ray target by the tungsten cathode filament.

about the thicknesses of the layers which is essential for a good estimation of the applied electric field and further electrical properties like the dielectric constant and the coercive field. In this specific case, the thickness of the $PZT_{40/60}$ and $PZT_{20/80}$ film is 100 nm and 90 nm, respectively. From Fig. 4.6 it can be seen that the SRO grows coherently. As shown in Fig. 4.6a a detailed microstructure with many features is exhibited by the

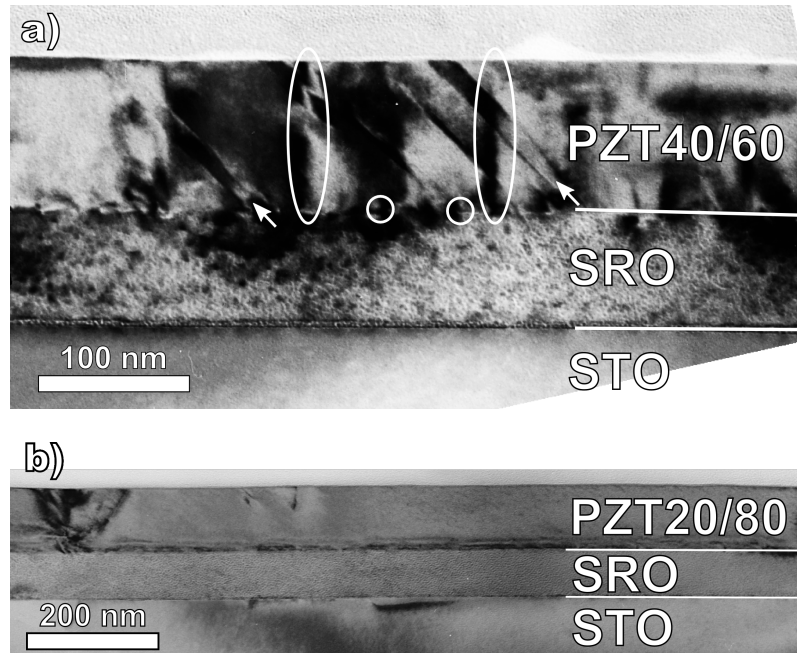


Figure 4.6: TEM cross-section micrographs of **a)** a 100 nm thick *PZT40/60* and **b)** a 90 nm thick *PZT20/80* film grown with a *SRO* bottom electrode on (001)-oriented *STO*, seen from the [010] *STO* direction. In **a)** a high density of misfit dislocations (circles), threading dislocations (ovals) and *a*-domains (arrows) are visible as signs for advanced relaxation. A much lower density of the structural features observed in **a)** is visible in the *PZT20/80* film shown in **b)**. Large regions of the film are free of extended defects.

PZT40/60 layer. Due to the lattice mismatch a high density of MDs can be observed at the interface with the bottom electrode. Threading dislocations (TDs) emerge from many of the MDs and propagate to the surface of the film, as the MDs are a preferred site for half loop nucleation. A feature typical for tetragonal ferroelectrics is the formation of *a*-domains, which are marked by white arrows in Fig. 4.6a. In contrast, the *PZT20/80* layer shown in Fig. 4.6b exhibits a very low density of these defects. MDs, accompanied by TDs, and *a*-domains occur only occasionally.

The slight difference between the in-plane lattice parameters of the used materials is the determining factor. From this difference the misfit of the two layers being in contact is calculated at growth temperature to estimate the extent of defect formation. As it is shown above, in the *SRO* layer a much lower density of dislocations is formed during growth, which justifies the assumption that this layer is coherent to the *STO* substrate and completely adopts its lattice parameter. Therefore, the subsequent *PZT* layer experiences the misfit with the lattice parameter of *STO*. This gives $f_{GT} = -3.01\%$ for a *PZT40/60* film and $f_{GT} = -1.84\%$ for a *PZT20/80* film with f_{GT} the misfit at growth temperature. Concluding from the MATTHEWS-BLAKESLEE criterion the critical thickness h_C for the introduction of MDs can be calculated as given in Eq. 2.6. This results in $h_C \approx 10\text{nm}$ for *PZT40/60* and $h_C \approx 20\text{nm}$ for *PZT20/80*. However, attention has to be paid to the boundary conditions of this structures. Since there is no covering layer, the strain cannot

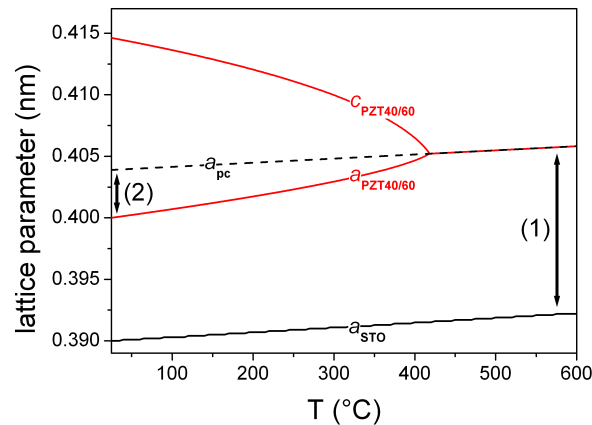


Figure 4.7: Lattice parameters of *STO* and *PZT40/60* in dependence on temperature. The dashed line designates the pseudocubic lattice parameter a_{pc} of *PZT40/60* extrapolated from the paraelectric phase. At elevated temperatures the *PZT40/60* film is exposed to compressive strain, as indicated by arrow (1). At room temperature tensile strain acts on the ferroelectric film, indicated by arrow (2).

be shared and there is only one interface to form MDs. Therefore, the critical thickness is given by Eq. 2.7 [58]. Analysing the TEM pictures in Fig. 4.6 reveals a high MD density at the *PZT40/60* / *SRO* interface, but in spite of the also low critical thickness obviously a larger spacing of the MDs for the *PZT20/80* film and consequently only local relaxation takes place in the latter case. Several reasons might be responsible for this observation [60]. First, the lattice relaxation is very sluggish. Since the film deposition takes only a finite time and PLD is known to result in a non-equilibrium film growth [78], the experimentally determined critical thickness would be higher and the observed density of MDs would be lower than theoretically expected. Due to the difference in the critical thickness, which is for *PZT20/80* twice as large as for *PZT40/60*, this effect is able to effectively impede the formation of MDs in *PZT20/80*, whereas the kinetic barriers are overcome and a high density of dislocations occurs in *PZT40/60*. Second, the TEM investigations just cover a small part of the sample and therefore no statistics can be made on the real density of MDs. At a low density of MDs it might be estimated lower than the true value.

Another feature observed in connection with the dislocations is the establishing of an *a/c*-domain structure. Although *PZT40/60* might be expected to be exposed to compressive strain due to the smaller in-plane lattice constant of the *STO*, the *a*-domains indicate tensile strain. This may result from the formation of MDs during growth. At growth temperature, indeed, compressive strain acts on the *PZT40/60* film (arrow (1) in Fig. 4.7). Therefore, the film elastically relaxes when exceeding the critical thickness (see Fig. 2.8). In the ideal case, the film would relax completely and experience no more strain. After deposition the film is cooled down. Below T_C the cubic lattice parameter a_c splits into two different tetragonal lattice parameters a and c with a being smaller than the extrapolated

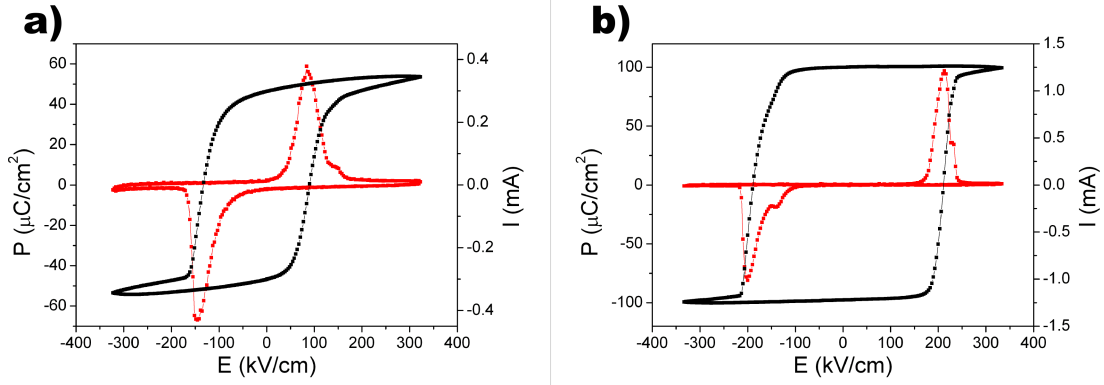


Figure 4.8: Typical hysteresis curve of **a)** *PZT40/60* and **b)** *PZT20/80* films. The black line denotes the polarisation the switching of which is accompanied by a switching current, displayed in red. Both hysteresis curves show a complete switching as confirmed by the current curve. The polarisation values of the *PZT20/80* film are enhanced with respect to the bulk values mostly due to the compressive in-plane strain.

a_c (dashed line in Fig. 4.7) which corresponds to a_{pc} (see Eqs. 4.1 and 4.2). At a_{pc} the film is relaxed. Therefore, a tensile strain would act on the a -axis of a purely c -oriented *PZT40/60* film (arrow (2) in Fig. 4.7). At temperatures below T_C , which are low compared to the ones used at the growth, the formation of additional or removal of redundant MDs is no longer possible. Therefore, in some parts of the film 90° domains form, i.e. the c -axis is turned in-plane to create an average lattice parameter $xa + (1 - x)c$ (with $0 < x < 1$) which is closer to the substrate's lattice parameter (as shown schematically in Fig. 2.9a and experimentally in Fig. 4.6a). This means the formation of a -domains reduces the elastic energy. The a -domains interact with the dislocations which are suspected to change the domain wall mobility and could even occasionally pin the a -domains [13]. In the case of *PZT20/80* films only marginal relaxation takes place which leads to a still compressive stress at room temperature, even subsequently to the tetragonal splitting of the lattice parameters. Consequently a -domains are observed only in the vicinity of TDs. Judging from these considerations the formation of a -domains in these heterostructures is not possible without the preceding relaxation process.

Electrical properties: All these structural features should manifest themselves in the electrical properties of the film. Measurements of the P-E hysteresis curve allow quickly to estimate the properties of the investigated ferroelectric material. Typical hysteresis curves of single crystalline epitaxial *PZT40/60* and *PZT20/80* films are shown in Figs. 4.8a and b. The P-E hysteresis curves show a remanent polarisation of $P_r \approx 50 \frac{\mu C}{cm^2}$ and $P_r \approx 100 \frac{\mu C}{cm^2}$ for *PZT40/60* and *PZT20/80* films, respectively. The switching current shows peaks around the coercive field for both positive and negative voltage. Outside this region the measured current values go down to nearly zero; the leakage current is quite low compared to the switching current. A further important quantity describing the

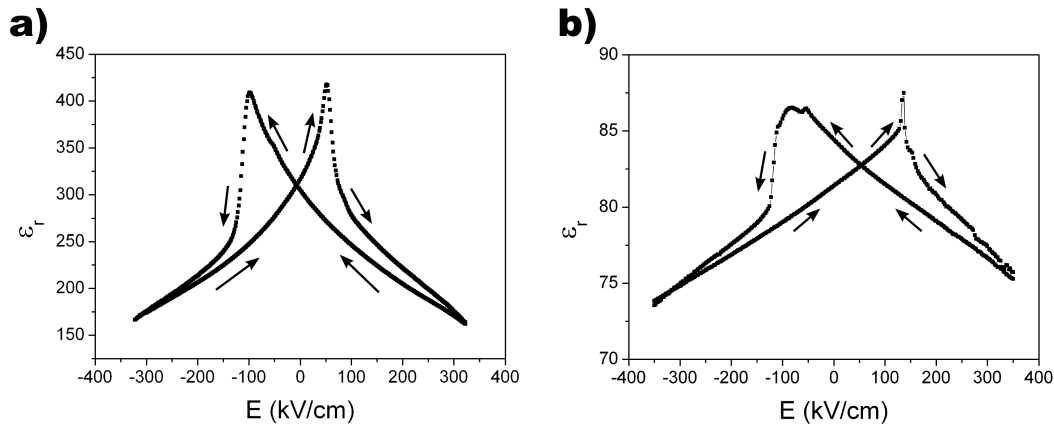


Figure 4.9: Voltage dependent dielectric constant of **a)** *PZT40/60* and **b)** *PZT20/80* from C-V measurements assuming the plan-parallel capacitor model. The influence of the asymmetric electrode alignment is clearly visible in the different peak shapes of the *PZT20/80*. Outside the switching peaks the effective dielectric permittivity is not constant but decreases as the voltage increases.

properties of ferroelectrics is the dielectric constant. Its voltage dependence for the films shown in Fig. 4.8 can be seen in Fig. 4.9. The dielectric constant at zero field amounts to $\epsilon_r \approx 310$ for the *PZT40/60* and $\epsilon_r \approx 80$ for the *PZT20/80* films.

Obviously, the electrical properties of *PZT20/80* and *PZT40/60* films are different, partly reflecting the nature of the observed microstructures. Concerning the *PZT20/80* film the compressive strain on the *a*-axes leads to an increase of the *c*-axis lattice parameter which is given by the POISSON ratio. The increased tetragonality should have a direct impact on the remanent polarisation P_r by enhancing it [62]. The polarisation is not expected to increase proportionally to the tetragonality but the increase can still be notable [63, 64, 65]. Indeed, fabricated samples exhibit square-shaped P-E hysteresis loops with a measured value of the remanent polarisation of about $100 \frac{\mu\text{C}}{\text{cm}^2}$, considerably larger than the theoretical bulk value of $70 \frac{\mu\text{C}}{\text{cm}^2}$ [111]. In the case of *PZT40/60*, parts of the film consist of *a*-domains, which means an effective loss of the remanent out-of-plane polarisation for this volume fraction, since the direction of polarisation is in-plane. This reduces the measured remanent polarisation.

In contrast to the influence of the tensile strain on the remanent polarisation, the dielectric constant is enhanced. In bulk *PZT* the dielectric constant perpendicular to the polarisation axis is higher than along the *c*-axis. This causes higher values of the effective dielectric constant of the *PZT40/60* film due to the contribution of the *a*-domains [110]. An even higher influence has the presence of the domain walls. These are able to respond to the applied electric field, leading to a significant increase of the effective dielectric constant.

A general feature exhibited by the voltage dependent dielectric constant of ferroelectrics are two maxima caused by the polarisation switching. In order to understand the origin of these peaks it has to be recalled that the measured quantity is not the dielectric constant

but the derivative of the dielectric displacement $\frac{dD}{dE}$. Starting from the general formula

$$D = \epsilon_0 E + P \quad (4.3)$$

P can be specified for ferroelectric materials as [110, 112]

$$\begin{aligned} P &= \chi E + P_S \\ &= \epsilon_0 (\epsilon_r - 1) E + P_S. \end{aligned} \quad (4.4)$$

This leads to the relation

$$D = \epsilon_0 \epsilon_r E + P_S. \quad (4.5)$$

The quantities denoted in these equations are the dielectric displacement D , the vacuum permittivity ϵ_0 , the electric field E , the polarisation P , the dielectric susceptibility χ , the spontaneous polarisation P_S and the relative dielectric constant ϵ_r . From Eq. 4.5 it follows the derivative

$$\frac{dD}{dE} = \epsilon_0 \epsilon_r + \frac{dP_S}{dE}. \quad (4.6)$$

In the case of a constant polarisation, such as at very high fields, this would be equal to the linear dielectric constant, but in case of the switching process the polarisation changes abruptly. Therefore the polarisation's derivative around E_C significantly contributes to $\frac{dD}{dE}$ and is responsible for the peaks of ϵ_r . This can be depicted by the fact, that at E_C the maximum number of domain walls exist in the sample whose reversible movement give a very high dielectric response [113]. Since the applied voltage changes much slower than in the hysteresis measurements, the coercive voltage determined from these peak positions is lower and approximately equal to the coercive voltage of a P-E hysteresis measured at a very low frequency.

The shape of the peaks of the dielectric constant around the coercive voltage varies with changing *PZT* composition: The dielectric constant of the *PZT40/60* film reveals symmetric peaks whereas these peaks are asymmetric in case of *PZT20/80*. Various effects originating from an asymmetric switching of the film or from the different electrodes and interfaces could contribute to this difference. The bottom electrode is made of *SRO* which is epitaxially connected as well with the *STO* substrate and with the subsequent *PZT* layer. In contrast the top electrode is made of *Pt* and sputtered at room temperature. Therefore, the interface at the top electrode is prone to structural and electronic defects and exhibits different electrical properties for different samples.

The contact of the *PZT* with the metal electrode leads to the formation of a SCHOTTKY contact [114, 115] associated with a band bending at the interface when the FERMI levels E_F of the *PZT* and E_{Fm} of the metal electrode line up (Fig. 4.10a). The band bending

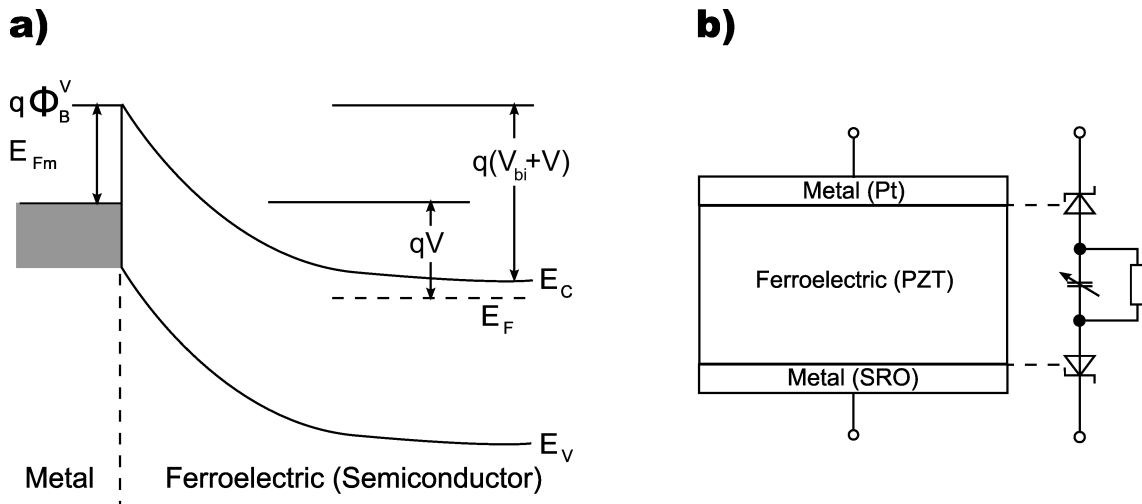


Figure 4.10: **a)** Energy band diagram of a contact between a metal electrode and an n-type semiconductor under a reverse bias V . At $V = 0$ the Fermi energy E_F of the semiconductor lines up with the Fermi energy E_{Fm} of the metal electrode. $q\Phi_B^V$ denotes the potential barrier which has to be overcome by the charge carriers to enter the semiconductor. V_{bi} is the built-in voltage resulting from the band bending. **b)** Model representation and equivalent circuit of a ferroelectric material with semiconducting character sandwiched between two metal electrodes. The interfaces between film and electrodes as well as the ferroelectric film change their electrical properties in dependence on an applied voltage.

leads to a depletion layer in the *PZT*. Two back-to-back SCHOTTKY diodes are formed by the interfaces between the ferroelectric layer and the two electrode layers (Fig. 4.10b). Depending on the sign of the applied voltage, the depletion layer vanishes at one of the interfaces. The depletion region strongly contributes to the film's capacitance which is used to calculate the dielectric constant. Since the depletion region always includes the interface, it is very susceptible to any modifications of the electrical properties of the interface. Depending on the sign of the applied voltage, the depletion region containing either the top or the bottom interface plays the major role in establishing the polarisation value. This leads to different peak shapes for different sweeping directions. The 'polarisation down' state seems to be preferred since the switching towards this state proceeds in a much closer voltage range as indicated by the narrower peak in Fig. 4.9b. This is also visible in Fig. 4.8b though less pronounced: at positive coercive field the slope of the P-E hysteresis is steeper and the peak of the switching current is higher and narrower. However, even in the ideal case of crystallographically perfect interfaces the electrode materials would still cause a slight asymmetry due to the smaller work functions of *SRO* compared to *Pt* which leads to a difference of $\Delta\Phi_B^0 = 0.75\text{ eV}$ [116]. This causes a different shift of the FERMI level accompanied by the respective band bending and thus the depletion regions are of different width, which in turn leads to an internal electric field pointing towards the bottom electrode. This might be one reason for the often observed polarisation down state in the as-grown samples. Contrary to the *PZT20/80* film, in the case of *PZT40/60* a high density of MDs forms already at the *SRO* electrode. In this way

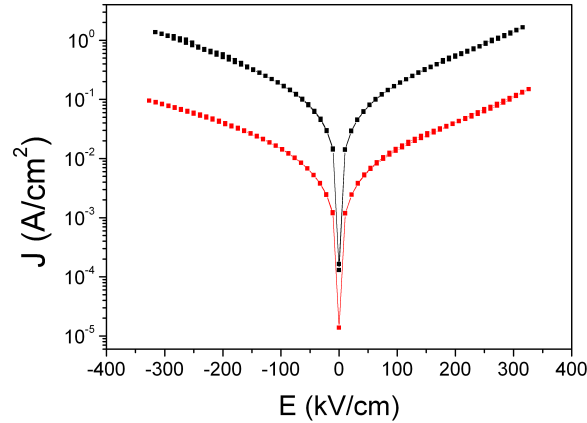


Figure 4.11: Current density in dependence on the electric field of *PZT20/80* (red symbols) and *PZT40/60* (black symbols) calculated from I-V measurements. The leakage current in the dislocation-free *PZT20/80* film is smaller than in the defective *PZT40/60* film.

both interfaces become similar in terms of defects and this leads to more symmetric C-V characteristics (Fig. 4.9). Additionally, the domain walls play a larger role in the dielectric constant, reducing the influence of the depletion region.

A further feature of the voltage dependence of the dielectric constant is that it does not stay at a constant value outside the switching peaks (as it should be according to Eq. 4.6) but decreases continuously. Again, the Schottky behaviour of the interfaces has to be stressed to explain this decrease. The thickness of the depletion layer, and therefore also the capacitance, depends on the applied voltage. The dependence of the capacitance C on the applied voltage V , caused by the broadening of the depletion layer, can be described by [117]

$$C \propto \frac{1}{\sqrt{V}}. \quad (4.7)$$

If the SCHOTTKY model is applied, information about the electronic properties of the *PZT* films can be deduced from capacitance-voltage (C-V) and current-voltage (I-V) measurements. The latter are presented as $J(E)$ curve in Fig. 4.11. During C-V measurements, only the mobile charges are able to follow the high frequency of the probing field, thus their density n can be determined by [117, 118]:

$$n = \frac{2}{q\epsilon_0\epsilon_r A^2} \left(\frac{1}{d(1/C^2)/dV} \right) \quad (4.8)$$

where q is the electron charge, ϵ_0 the dielectric constant of the free space, ϵ_r the static dielectric constant, A the electrode area, C the capacitance and V the voltage applied on the investigated sample. The carrier density n which is determined by Eq. 4.8, correlates with the doping density as long as all impurities are ionised at room temperature and the contribution of deep traps is negligible.

Regarding the leakage properties, thermionic emission over the potential barrier Φ_B^V is assumed as the injection mechanism of the charge carriers into *PZT*. Therefore, the current density is given by

$$J = A^* T^2 \exp \left[-\frac{q}{kT} \left(\Phi_B^0 - \sqrt{\frac{qE_m}{4\pi\epsilon_0\epsilon_{op}}} \right) \right]. \quad (4.9)$$

using RICHARDSON's constant A^* , the temperature T BOLTZMANN's constant k , the SCHOTTKY barrier height at zero voltage Φ_B^0 , the optical dielectric constant ϵ_{op} , and the maximum electric field at the interface E_m . In order to account for the ferroelectric properties, the polarisation is considered as a sheet of charge near the surface.¹ This causes a change of the band bending and directly links the polarisation with the electronic properties [119]. For instance the influence of the semiconductor properties on the dielectric properties can be described. In this way, if *PZT* is considered as a semiconductor, the adapted SCHOTTKY model is able to describe the measured features. In addition, it offers the possibility of determining the electronic properties of the investigated ferroelectric material.

Using Eq. 4.8, the density of free charges n and the built-in voltage V_{bi} are evaluated. This is done by plotting $\frac{1}{C^2}$ versus voltage. From the slope of the resulting graph outside the switching region, n is calculated and the interception point at $V = 0$ gives an estimation of V_{bi} . By applying a nonlinear regression of Eq. 4.9 to the curve of the current density, using a least squares fit, the barrier height Φ_B^0 and the density of fixed space charges N_{eff} are determined. The results are summarised in Tab. 4.1. The values of N_{eff} and V_{bi} are subjected to high fluctuations which makes it useless to distinguish between the two *PZT* compositions. Therefore only the order of magnitude is given.

As it can be seen from Fig. 4.11 the leakage current of the *PZT20/80* film is lower compared to that of the *PZT40/60* film. Despite this fact the density of mobile charges is lower in the *PZT40/60* film (Tab. 4.1). This finding is consistent with the described structural properties which show a high density of defects in this film. These act as traps and scattering centres for the carriers and therefore reduce their density in the conduction band [120]. However, the Schottky barrier in the *PZT40/60* film is lower than in *PZT20/80* which causes the observed higher leakage current.

¹The maximum electric field E_m at the interface can be calculated according to

$$E_m = \sqrt{\frac{2qN_{eff}(V + V_{bi})}{\epsilon_0\epsilon_r}} \pm \frac{P_S}{\epsilon_0\epsilon_r}, \quad (4.10)$$

with the apparent built-in voltage V_{bi} and the effective charge density in the depleted region N_{eff} which also includes charged traps.

<i>PZT</i>	P_r ($\mu\text{C}/\text{cm}^2$)	ϵ_r ($f = 100\text{kHz}$)	n (10^{18}cm^{-3})	Φ_B^0 (eV)
40/60	55	310	5.5 ± 0.2	0.76 ± 0.03
20/80	100	80	17.6 ± 1.0	1.11 ± 0.04
$N_{eff}(\text{cm}^{-3})$ $V_{bi}(\text{V})$		$\approx 10^{20} \dots 10^{21}$ $\approx 10^{-1}$	for both <i>PZT</i> compositions for both <i>PZT</i> compositions	

Table 4.1: Evaluated values of the remanent polarisation P_r , the dielectric constant ϵ_r , the density of charge carriers (electrons) n and the potential barrier Φ_B^0 of *PZT20/80* and *PZT40/60* films. Due to big fluctuations of the determined values of the effective space charge density in the depleted region N_{eff} and the apparent built-in voltage V_{bi} only the order of magnitude can be given.

Summary

The structural properties of the *SRO* layer and films of both *PZT* compositions were investigated both theoretically and experimentally. It was demonstrated that the growth mode of the *SRO* can be controlled by varying the deposition conditions. A pseudo-morphic growth of *SRO* on *STO* was achieved. *PZT* was grown heteroepitaxially and (001)-oriented onto the *SRO* electrode. The higher misfit caused a much stronger relaxation of the *PZT40/60* films accompanied by a high dislocation density compared to the *PZT20/80* films which in turn exhibited only a very small density of dislocations. Below T_C *a*-domains were formed to release the strain newly introduced during cooling down the heterostructure from growth temperature to room temperature. Caused by the higher dislocation density also the density of *a*-domains is much higher in the *PZT40/60* film.

Investigations of the resulting ferroelectric and dielectric properties of the *PZT* films revealed the impact of the microstructure on the macroscopic quantities. A higher dielectric constant was observed in *PZT40/60* films due to the contribution of the *a*-domains. At the same time the remanent polarisation was decreased due to the relaxation of the compressive strain.

The SCHOTTKY model was applied to deduce the electronic properties. It was found that the *PZT40/60* films exhibited a smaller density of free charge carriers and a strongly reduced SCHOTTKY barrier height which results in a higher leakage current. No difference in the density of fixed space charges and the built-in voltage could be determined within the accuracy of the investigations.

Both the choice of the substrate-film combination and the thickness of the film can be utilised to modify the properties of the ferroelectric film. However, this provides not many degrees of freedom to tune the properties. Therefore, an artificial interface is introduced in the next chapter to more efficiently control the microstructure of the ferroelectric film.

4.2 Modification by one additional interface

Having investigated the properties of ferroelectric films consisting of either *PZT20/80* or *PZT40/60*, this chapter is dedicated to the influence of modifications in the ferroelectric film. This is done by combining these two *PZT* compositions in form of bilayers in order to specifically create an artificial interface within the ferroelectric film. As shown in Section 4.1, for a given film-substrate combination with a corresponding lattice misfit, the dislocation content and domain formation in single composition thin films are determined mainly by the film thickness and the growth conditions. A bilayer structure offers the possibility to control the formation of both features via the presence of the additional interface. Due to the different misfits between the layers and between the individual layers and the substrate, various relaxation and elastic domain states are possible. In spite of the relatively small lattice misfit of the used system, it is possible to introduce elastic *a*-domains into the layers via changing their sequence where the relaxation state of one layer alters the strain state of the other. It is one of the motivations to characterise the impact of *a*-domains on the electrical properties of a bilayer by changing the growth parameters in a controlled manner. Due to the pseudomorphic growth of the *SRO* onto *STO* (100) vicinal crystals, the *PZT* layers directly experience the misfit with the thick *STO* substrate.

Structures of *PZT20/80* / *PZT40/60* bilayers: For *PZT20/80* and *PZT40/60* layers well above the critical thickness for misfit dislocation formation, there are two main possibilities shown schematically in Fig. 4.12. (I) When the first grown layer is *PZT20/80*, this is strained to the substrate with a low dislocation density due to its small misfit with the *SRO/STO* of -1.8% ; however, the subsequent *PZT40/60* layer has a larger misfit of about -3.0% and grows by forming misfit dislocations (MDs) at the *PZT/PZT* interface accompanied by threading dislocations (TDs) propagating to the top surface. In addition, the top *PZT* layer exhibits narrow *a*-domains which are also originating from this interface. TEM pictures depicting this case are shown in Fig. 4.12a together with a schematic drawing in Fig. 4.12b. (II) When *PZT40/60* is used as the bottom layer, a high density of MDs forms at the interface with the *SRO* electrode. From the MDs many TDs emerge towards the free surface of the structure, crossing the entire *PZT20/80* top layer. On the other hand, the abrupt strain state change at the interface could also act as a barrier for the TDs' propagation [121, 122], and somewhat reduces the dislocation content in the top layer with respect to the bottom one. Moreover, two different domain states are possible in the case of this particular dislocation distribution: 1) the *a/c*-domains are confined to the *PZT20/80* layer and terminate at the interface, as shown in Figs. 4.12c and 4.12d; 2) the domains are crossing the interface, extending through the entire film (Fig. 4.12e and 4.12f) in order to reduce the overall elastic energy of the structure, when the elastic energy of the partially strained film is high enough (possible in thicker films).

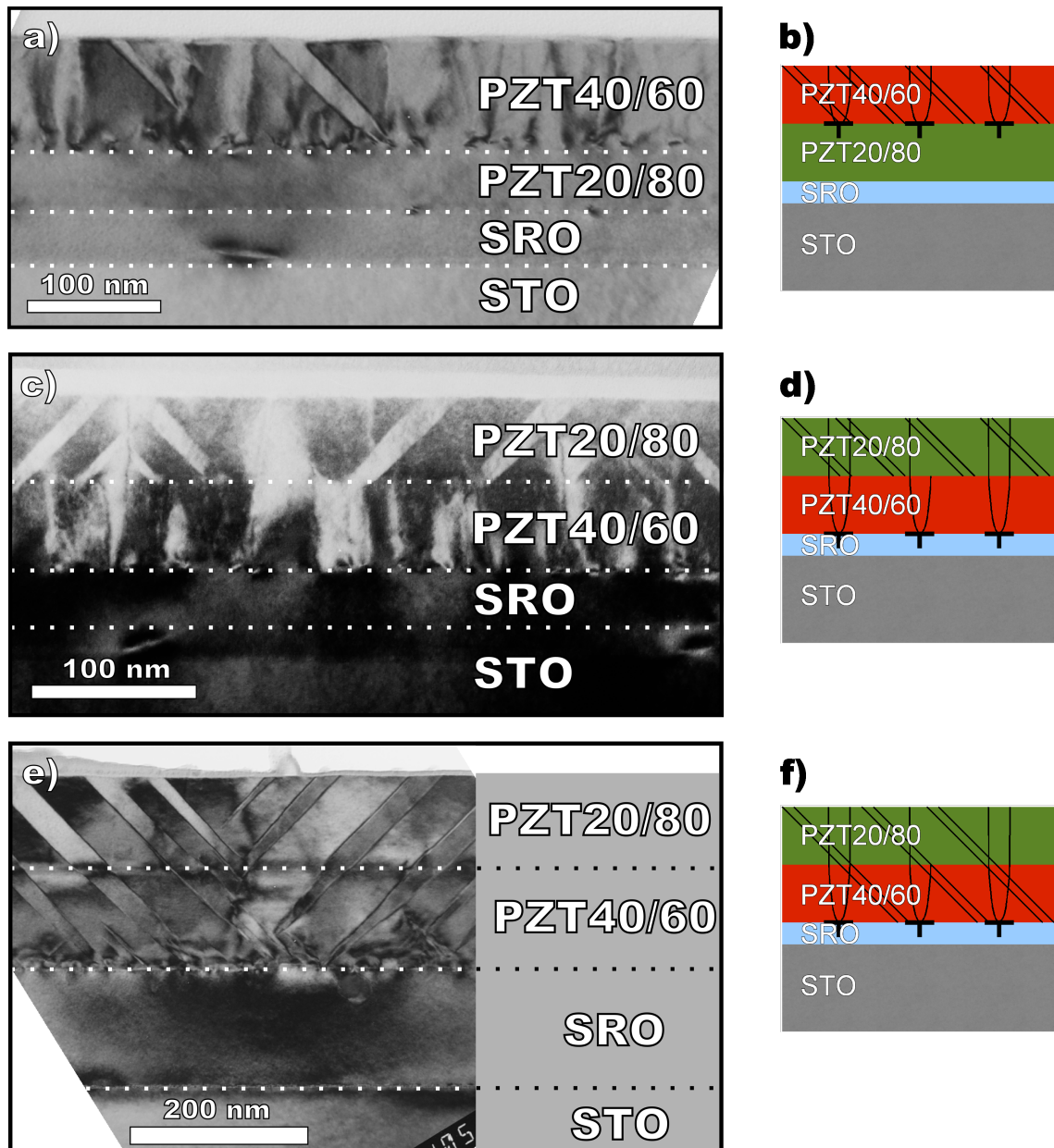


Figure 4.12: TEM cross-section micrographs (a, c, e) and according schemes (b, d, f) showing the layer sequence, domain walls, misfit and threading dislocations of ferroelectric bilayers consisting of *PZT20/80* and *PZT40/60* grown with a *SRO* bottom electrode on (001)-oriented *STO*, seen from the [010] *STO* direction.

Effect on electrical properties: The voltage dependent polarisation and dielectric constant of all films were measured. Typical results on heterostructures with two ferroelectric layers of equal thickness are shown in Figs. 4.13 and 4.14. Both the bilayers with a *PZT40/60* (Fig. 4.13a) and with a *PZT20/80* (Fig. 4.13b) bottom layer show saturated hysteresis curves and low leakage. In spite of the qualitatively different microstructures (Fig. 4.12a and 4.12c) the hysteresis curves show a similar shape. However, a larger value of the remanent polarisation is observed if a *PZT20/80* bottom layer is used. In contrast the shape of the C-V curve exhibits clear differences.

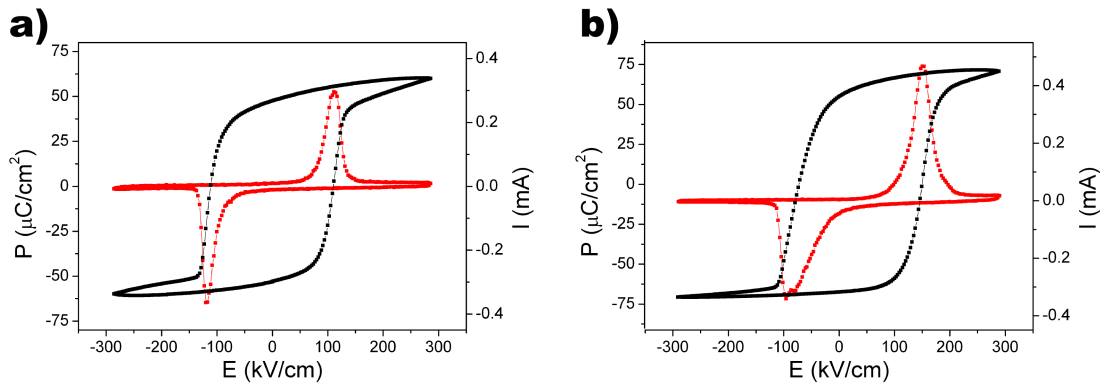


Figure 4.13: P-E Hysteresis curves with corresponding switching current of bilayers with **a)** a dislocation-rich *PZT40/60* bottom layer and **b)** a *PZT20/80* bottom layer containing only a low dislocation density. Both show a slanted P-E curve with a larger remanent polarisation in case of the *PZT20/80* bottom layer. The switching current curves show a clear switching peak demonstrating a complete switching at the maximum applied electric field.

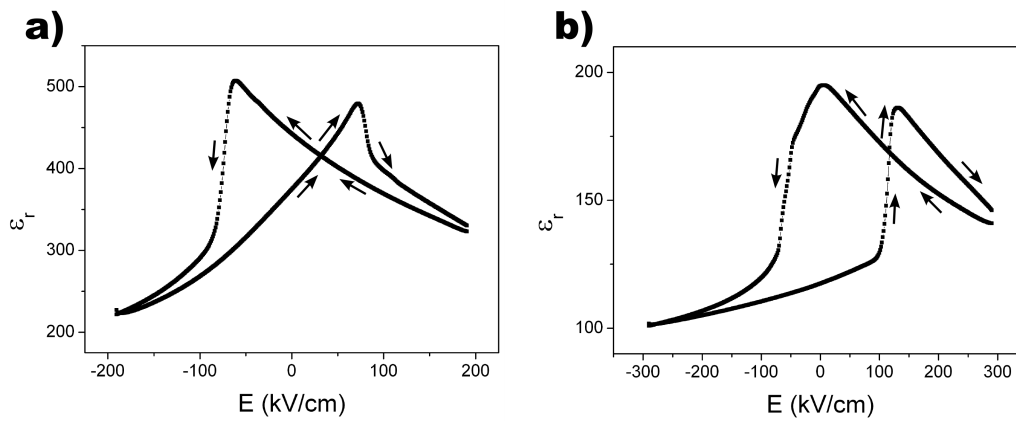


Figure 4.14: **a)** Voltage dependent dielectric constant of bilayers possessing a *PZT40/60* bottom layer which contains threading dislocations forming at the interface with the bottom electrode (see Figs. 4.12c - 4.12f). **b)** If a *PZT20/80* bottom layer is used, which has a very low density of dislocations (see Figs. 4.12a - 4.12b), the dielectric constant is smaller and exhibits asymmetric peaks at the coercive field.

As discernible from Fig. 4.14a the switching peaks of the dielectric constant of a film with a *PZT40/60* bottom layer show a steeper slope following the switching peak than before it, with a slightly larger maximum for negative voltages. The peaks of films with a *PZT20/80* bottom layer though are asymmetric, both exhibiting the steeper slope at the left edge as if just shifted along the abscissa.

The values at zero voltage are graphically summarised in Fig. 4.15, showing the dependence of the remanent polarisation P_r and dielectric constant ϵ_r on the relative thickness $\alpha = t_{PZT40/60}/t_{bilayer}$, with $t_{bilayer} = t_{PZT40/60} + t_{PZT20/80}$, of the structures. It can be seen that the different microstructures significantly modify the values of measured P_r and ϵ_r . Structures with a *PZT20/80* bottom layer containing a rather low density of dislocations

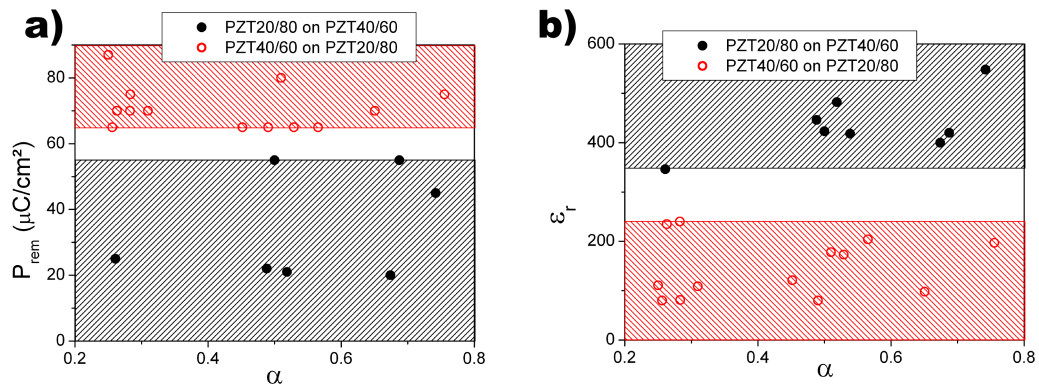


Figure 4.15: a) Remanent polarisation and b) dielectric constant of bilayers with a *PZT20/80* (○) and a *PZT40/60* bottom layer (●). The shaded areas designate the codomains of the measured values caused by the different layer sequences.

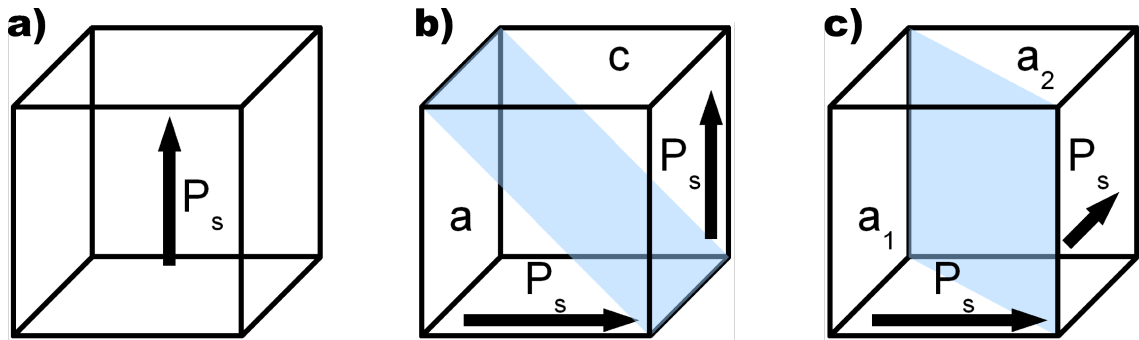


Figure 4.16: Changing domain structure of tetragonal *PZT20/80* at room temperature. a) Single *c*-domain state of *PZT20/80* at compressive misfit strain $f < -1.5\%$. b) *a/c*-domain state of *PZT20/80* at moderate misfit strain $-1.5\% < f < +0.5\%$. c) a_1/a_2 -domain state of *PZT20/80* at tensile misfit strain $f > +0.5\%$.

(Fig. 4.12a and 4.12b and corresponding open circles in Fig. 4.15) exhibit mean values of $P_r \approx 70 \mu\text{C}/\text{cm}^2$ and $\epsilon_r \approx 145$. In contrast to this picture, the films with a dislocation-rich *PZT40/60* bottom layer (Fig. 4.12c - 4.12f and corresponding full circles in Fig. 4.15) show a smaller P_r of about $35 \mu\text{C}/\text{cm}^2$ and a much higher $\epsilon_r \approx 435$. The corresponding cases of the two possible sequences in the bilayers are indicated by the shaded areas in Fig. 4.15.

Modelling: Inside the marked regions the values show a large scattering. This behaviour is not comprehensible by descriptive approaches. To explain these experimental observations, the LANDAU - GINZBURG - DEVONSHIRE (LGD) theory for ferroelectrics was adopted in an attempt to understand the impact of possible influences such as misfit of the layers and electrostatic coupling due to the polarisation jump at the interface on the properties [123]. Certainly, the LGD theory theoretically describes an ideal system which does not exist in reality, but the trend should be reproducible. Due to a varying misfit strain, the domain structure of *PZT* might change from pure *c*-domain over *a/c*-domain to

a_1/a_2 -domain [124] (here subscript 1 and 2 imply the domain orientations in a layer) as displayed in Fig. 4.16, if the strain becomes sufficiently high. The present approach includes appropriate modifications to the bulk LGD potential of the components taking into account the misfit strain due to the film-substrate lattice mismatch, relaxation by dislocations and a -domains as well as the electrostatic coupling of the two ferroelectric layers. The deposited films exhibit a thickness of about 100nm . This thickness is well above the usual thickness for similar systems where interface- and size-effect related phenomena have been reported to play a major role, therefore such effects have been neglected. The free energy density of a bilayer is defined as [125]

$$F = \alpha F_1 + (1 - \alpha) F_2 + F_C \quad (4.11)$$

with α being the relative thickness of the layer 1 and F_i ($i=1,2$) being the LGD potential of the individual layers that also contains the elastic energy due to misfit strain. An additional contribution F_C represents the energy due to the electrostatic coupling between the layers as a result of the polarisation discontinuity at the interfaces. The free energy densities F_i of each layer can be written in the form

$$F_i = F_0 + aP^2 + bP^4 + cP^6 - EP \quad (4.12)$$

where a and b are the strain-modified thermodynamic coefficients, c is the higher order dielectric stiffness coefficient in bulk state of layer i , (α_{111} in Ref. [126]) P the polarisation and E the external electric field parallel to the polarisation. Coefficients a and b include the effect of the pseudocubic misfit and the clamping of the thin film to the substrate originating from the addition of elastic energy terms to the bulk free energy. In the presence of different domain states, forms of the coefficients a and b are modified to reflect the presence of domains with different elastic strain values due to the misfit f [124]. For the case of a single film consisting of only c -domains,

$$a = \frac{T - T_C}{2\epsilon_0 C} + f \frac{2Q_{12}}{S_{11} + S_{12}}; b = \alpha_{11} + \frac{Q_{12}^2}{S_{11} + S_{12}} \quad (4.13)$$

with T_C being the CURIE temperature, C the CURIE constant, S_{ij} the elastic compliances, Q_{ij} the electrostrictive coefficients and α_{11} the dielectric stiffness for the bulk. The coefficients for a single-composition structure consisting of a/c - and a_1/a_2 -domains are

$$a^* = \frac{T - T_C}{2\epsilon_0 C} + f \frac{Q_{12}}{S_{11}}; b^* = \alpha_{11} + \frac{Q_{12}^2}{2S_{11}} \quad (4.14)$$

for the a/c structure and

$$a^{**} = \frac{T - T_C}{2\epsilon_0 C} + f \frac{Q_{11} + Q_{12}}{S_{11} + S_{12}}; b^{**} = \alpha_{11} + \frac{(Q_{11} + Q_{12})^2}{4(S_{11} + S_{12})} \quad (4.15)$$

for the a_1/a_2 structure, respectively. In order to find out which domain configuration is stable for a given misfit strain, the free energy has to be implemented with the term describing the purely elastic misfit strain energy, which excludes the self-strain energy. This term is

$$\frac{f^2}{S_{11} + S_{22}} \text{ and } \frac{f^2}{2S_{11}} \quad (4.16)$$

for the single c -domain state and the a_1/a_2 -domain configuration, and for the a/c -domain configuration, respectively. Equations 4.12 through 4.16 hold only for a single layer at a particular strain state. The minimisation of the free energy with respect to polarisation and a -domain fraction will give the stable domain configuration at a given temperature.

An important term in the free energy of the ferroelectric multilayer heterostructures is the one describing the electrostatic coupling between the component layers. This term should be expected to contribute significantly to the free energy of the system due to the polarisation difference at the interface. It must also to be kept in mind that the formation of a -domains is not related to any electrostatic interaction but is purely due to elastic misfit strain. The fraction of these a -domains, however, can slightly shift with external applied field that is one of the considerations in this study.

If sufficient elastic strain exists to stabilise c -domains in both layers, the electrostatic coupling term due to the polarisation-induced bound charge at the bilayer interface reads

$$F_C = \frac{1}{2\epsilon_0} \alpha (1 - \alpha) (P_1 - P_2)^2 \quad (4.17)$$

with ϵ_0 being the dielectric permittivity of vacuum, P_1 the polarisation of the top layer (layer 1) and P_2 the polarisation of the bottom layer (layer 2). In case of an elastic strain that favours a/c -domain configuration of the top layer, the fraction Φ_a of a -domains will be determined by

$$\Phi_a = \frac{(S_{11} - S_{12})(f - Q_{12}P_{c1}^2)}{S_{11}(Q_{11} - Q_{12})P_{c1}^2} \quad (4.18)$$

where P_{c1} is the polarisation of the c -domains in layer 1. The used approach assumes that the a -domains have a small induced c -polarisation due to the presence of an uncompensated charge at the interface between the layers. Thus, the single c -domain state of the bottom layer induces a small c -component (out-of-plane) of the polarisation in a -domains of the top layer and couples to the c -domain polarisation as in Eq. 4.17. This is due to the susceptibility of the a -domains along the out-of-plane direction with respect to the interface between the layers. Therefore the electrostatic coupling can be described as

$$F_C = \frac{1}{2\epsilon_0} \alpha (1 - \alpha) ((1 - \Phi_a)P_{c1} + \Phi_a P_{a1} - P_2)^2. \quad (4.19)$$

Here P_{a1} is the induced out-of-plane polarisation in the a -domains of layer 1. Equation 4.19 simply dictates that the electrostatic coupling will occur between all layers with

the contribution from the a -domains. For instance, had there been only an a_1/a_2 -domain configuration of the top layer, there would have been only induced polarisation in layer 1 and the coupling term would be written as

$$F_C = \frac{1}{2\epsilon_0} \alpha (1 - \alpha) (P_{a1} - P_2)^2. \quad (4.20)$$

If both layers exhibit an a/c -domain structure, the coupling term becomes

$$F_C = \frac{1}{2\epsilon_0} \alpha (1 - \alpha) ((1 - \Phi_{a1})P_{c1} + \Phi_{a1}P_{a1} - (1 - \Phi_{a2})P_{c2} - \Phi_{a2}P_{a2})^2 \quad (4.21)$$

with Φ_{a1} and Φ_{a2} the fraction of a -domains in the first and the second layer, respectively. It should be noted here that the used method does not take into account spatial variations in polarisations neither in the vicinity of the a -domain/ c -domain nor a -domain/ a -domain junctions of the two layers but only the sum of polarisation values of each layer. The induced c -polarisation in the a -domains gives rise to an additional energy term that also has to be taken into account [127]. This can be deduced for each layer where an a -domain has an additional c -polarisation component, modifying the free energy of a -domains in a layer i , F_i^a , in the form:

$$F_i^a(P, E = 0) = 2a^{**}P_a^2 + aP_c^2 + b_1P_a^4 + bP_c^4 + b_2P_a^2P_c^2 + \alpha_{111} (2P_a^6 + P_c^6) \\ + \alpha_{112} (2P_a^4 (P_a^2 + P_c^2) + 2P_a^2P_c^4) + \alpha_{123}P_a^4P_c^2 \quad (4.22)$$

containing the higher order dielectric stiffness coefficients α_{ijk} and the modified coefficients

$$b_1 = 2 \left(\alpha_{111} + \frac{1}{2} \frac{(Q_{11}^2 + Q_{12}^2) S_{11} - 2Q_{11}Q_{12}S_{12}}{S_{11}^2 - S_{12}^2} \right) \\ + \left(\alpha_{112} - \frac{(Q_{11}^2 + Q_{12}^2) S_{12} - 2Q_{11}Q_{12}S_{11}}{S_{11}^2 - S_{12}^2} + \frac{Q_{44}^2}{2S_{44}} \right) \quad (4.23)$$

and

$$b_2 = 2 \left(\alpha_{123} + \frac{Q_{12}(Q_{11} + Q_{12})}{S_{11} + S_{12}} \right). \quad (4.24)$$

for a layer i .

Depending on the type of elastic strain states in the layers and the relaxation mechanisms, the stable equilibrium domain configuration can be determined using the relations 4.11-4.24. F has to be minimised with respect to each polarisation component in order to calculate the polarisations in each layer. It is important to remind here that the polarisation solutions of both layers, including the solutions for the a -domains are all connected through the electrostatic coupling. Following the polarisation solutions, the small signal

dielectric constant ϵ_r was also calculated which is basically the polarisation difference arising in the structure when applying a small external electric field E_0 :

$$\epsilon_r = \frac{P(E = E_0) - P(E = 0)}{E_0}. \quad (4.25)$$

With the help of the described method any combination of ferroelectric materials with arbitrary misfits can be described if the required coefficients are known. However, to stay within a clear frame, the further consideration should refer only to the possible misfit combinations of the used heterostructure. Additionally the possible cases will be limited to the observed domain structures shown in Fig. 4.12.

The formation of misfit dislocations takes place at growth temperature. The resulting density of MDs determines the developing thermal strain in each layer upon cooling. Thus, a -domain formation in any of the layers will result once the particular layer reaches its T_C and if the misfit strain favours an a/c domain pattern of the layer, determined by comparing the free energies of possible domain states. Moreover, there could exist an a_1/a_2 pattern of a layer with the other layer being in any of the a/c -, c - or a_1/a_2 - domain states depending on the individual strain states of the layers. The misfit strain after cooling is the relevant misfit f used in the calculations. Therefore, the misfit has to be evaluated at the growth temperature and afterwards the resulting misfit at room temperature can be determined using the thermal expansion coefficients. The splitting of the lattice parameters due to the tetragonal distortion below T_C requires no additional attention because the above equations refer to the pseudocubic misfit. To calculate the pseudocubic lattice parameter, it is necessary to extrapolate the cubic lattice parameter of the paraelectric phase to below T_C . If required, it is possible to determine the tetragonal lattice parameters at any temperature from the pseudocubic lattice parameter as shown in Eqs. 4.1 and 4.2.

When estimating the range of misfit strains of the bottom layer, the highest possible misfit strain develops in the PZT if it is fully strained to the STO at growth temperature. Contrariwise, the lowest possible misfit strain arises if there is an extensive formation of MDs which leads to a complete relaxation of the PZT . In contrast the strain state of the top PZT layer refers no longer to the STO . It is limited solely by the grade of relaxation of the bottom PZT layer. When describing the relationship between the misfits of the PZT layers, the misfit of the bottom layer can be treated as the independent quantity whereas the misfit of the top layer is the dependent one. Some selected misfit combinations of this system including the bordering cases are listed in Tab. 4.2. Since the lattice parameter of the $PZT_{40/60}$ has a larger difference to the substrate's lattice parameter, a wider range of misfit combinations is possible if this composition is used as the bottom layer.

Even though misfit strain values for the same composition are the same in the middle two columns of Tab. 4.2 this does not mean that the resulting structures exhibit the same properties because they exhibit different a/c -domain structures. As already mentioned

only few particular a/c -domain structures are observed shown in Fig. 4.12: either the a -domains only form in the top layer (Figs. 4.12a - 4.12d) or they propagate through the whole film (Figs. 4.12e and 4.12f). Other imaginable cases like an a/c -domain structure limited to the bottom layer or a -domains consuming the whole thickness of a $PZT40/60$ on $PZT20/80$ film are not observed. To evaluate the maximum possible variation of P_r and ε_r , the misfit of the bottom layer is varied continuously from fully strained to fully relaxed. Concerning the top layer only both the extreme misfit cases are calculated without determining the states lying in between. So it has to be distinguished between the two cases of (a) a strained top layer and (b) a relaxed top layer for each of the three structural variants listed in Fig. 4.12. The values of P_r and ε_r depend on both misfits and the relative thickness α .

To determine the stability of the a -domain structure two conditions have to be fulfilled: First the fraction of a -domains has to be between zero and one, otherwise the result would make no physical sense. Second the free energy has to be lower than of the competing states. For bilayers with a $PZT20/80$ bottom layer in case (a) (strained top layer) the compressive strain acting on the $PZT40/60$ top layer stabilises the c -domain structure. In case (b) (relaxed top layer) there is only a small amount of residual strain originating from the thermal expansion and therefore, the a/c -domain structure is stable (both cases not shown as a graph). If $PZT40/60$ is used as the bottom layer there are two observed domain states. Therefore the formation of a -domains in the bottom layer can be allowed or forbidden by

$f(PZT20/80$ bottom layer)	-1.93 (fully strained)	-0.08 (fully relaxed)	-
$f(PZT40/60$ top layer) fully strained fully relaxed	-3.10 -0.08	-1.27 -0.08	-
$f(PZT40/60$ bottom layer)	-3.10 (fully strained)	-1.27 (partially relaxed)	-0.08 (fully relaxed)
$f(PZT20/80$ top layer) fully strained fully relaxed	-1.93 -0.08	-0.08 -0.08	+1.12 -0.08

Table 4.2: Misfit strain combinations of $PZT20/80$ and $PZT40/60$ on STO . The range of possible misfit strain of the top layer depends on the relaxation state of the bottom layer.

the applied model to match the observed cases (Figs. 4.12c - 4.12d or Figs. 4.12e - 4.12f). When the a -domains are forbidden, in case (b) the top layer forms an a/c -domain structure in the whole calculated range. Interestingly, in case (a) the conditions change with the misfit of the bottom layer:

Fig. 4.17 shows the difference of the free energies $\Delta F = F_{c\text{-domain}} - F_{a/c\text{-domain}}$ of the pure c -domain and the a/c -domain phase. When calculating the difference like this, a positive value of ΔF means that $F_{a/c\text{-domain}}$ is smaller than $F_{c\text{-domain}}$ and therefore the a/c -domain structure is energetically more favourable. This applies for the whole investigated range. Now it has to be taken care that in the dark shaded area the calculated fraction of a -domains is negative and therefore the a/c -domain structure only develops in the remaining part. If the a -domains are forbidden in the bottom layer, in case (a) the a -domains form only if $f_{PZT40/60} \geq -2.34\%$ (Fig. 4.17a) Case (b) was already mentioned above. In case of a -domains propagating through both layers, the region of a stable c -domain state is increased to $f_{PZT40/60} < -0.93\%$. If the strain becomes less compressive, a -domains will start to form. The strain state of the $PZT20/80$ top layer has no impact on the formation of a -domains. This happens both for coherent and relaxed $PZT20/80$ (Figs. 4.17b and 4.17c).

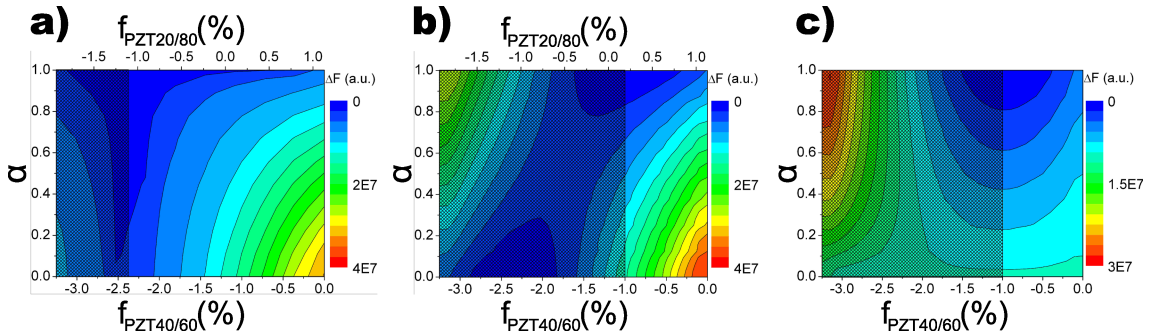


Figure 4.17: Difference of the free energies of the competing domain structures $\Delta F = F_{c\text{-domain}} - F_{a/c\text{-domain}}$ versus the misfits of the bottom layer and the relative thickness. The shaded area designates the misfit states where negative a -domain fractions occur which are therefore not stable in this area. **a)** Bilayer with a strained $PZT20/80$ top layer and the a -domains confined to this top layer. **b)** Bilayer with a strained $PZT20/80$ top layer and the a -domains propagating through the whole film. **c)** Bilayer with a relaxed $PZT20/80$ top layer and the a -domains propagating through the whole film.

By taking into account these stability conditions, P_r and ε_r are calculated (Fig. 4.18). The green plane represents the values of a bilayer containing a strained top layer whereas the blue plane refers to bilayers with a relaxed top layer. Concerning bilayers with a $PZT20/80$ bottom layer, P_r decreases if the compressive strain is released (Fig. 4.18a). That applies in several ways: First if the misfit of the bottom layer becomes smaller and second for the transition from the green to the blue plane. The third possibility concerns only the blue plane depicting a relaxed $PZT40/60$ top layer. In this case for an increasing α the fraction of the $PZT20/80$ decreases and therefore the impact of its strain on the

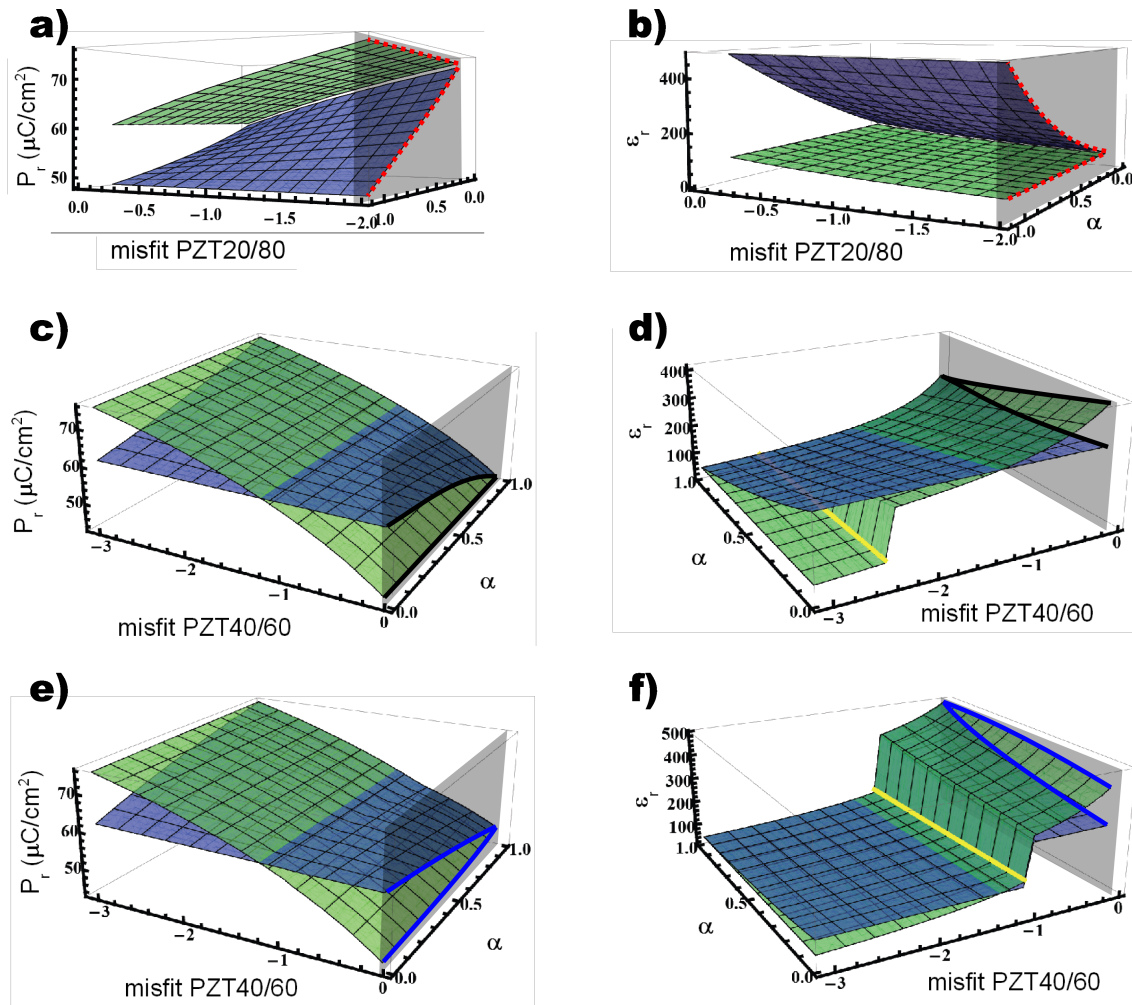


Figure 4.18: Theoretical results of the LGD approach on the remanent polarisation (**a**, **c**, **e**) and the dielectric constant (**b**, **d**, **f**). In **a**) and **b**) a *PZT20/80* bottom layer is used. Values of bilayers with a *PZT40/60* bottom layer and the *a*-domains confined to the top layer are shown in **c**) and **d**) whereas in **e**) and **f**) the *a*-domains are allowed to propagate through the whole film. The determined values depend on the misfit of the bottom layer and the relative thickness. The green plane represents the values of top layer coherent to the bottom layer whereas the blue plane represents the values of a fully relaxed top layer. The yellow line designates the changeover in the domain structure from a purely *c*-domain to an *a/c*-domain state. The grey planes mark the cross-section at a certain misfit of the bottom layer and the resulting lines correspond to the ones in Fig. 4.19.

electric properties of the ferroelectric film as a whole becomes less. ϵ_r behaves vice versa to P_r and increases under the described circumstances (Fig. 4.18b).

For the bilayers with a *PZT40/60* bottom layer the behaviour is more fascinating and not that easy to predict. One feature is the domain state which changes with the *PZT40/60*'s misfit as described above. This has a distinct impact on ϵ_r which increases considerably due to the introduction of the *a*-domains at a certain misfit of the bottom layer marked by the yellow line. The effect of the *a*-domains is clearly visible in Fig. 4.18d for the case of a coherent top layer (green plane) with domains constrained to it. Due to the transition from the *c*-domain to the *a/c*-domain structure there is a steplike increase of ϵ_r . At high

compressive misfits of the bottom layer, the blue plane exhibits higher values of ϵ_r because in this case the a/c -domain structure is stable from the beginning. Figure 4.18f depicts the case where the domains propagate through the whole bilayer. Again a steplike increase of ϵ_r is observed, this time for both planes due to the simultaneous formation of the a/c -domain structure in both layers. In contrast to the strong dependence of the dielectric constant on the domain state P_r of bilayers neither with a -domains confined to the top layer (Fig. 4.18c) nor with a -domains propagating through the whole film (Fig. 4.18e) are affected much by this. P_r just changes due to the altering strain state and layer fractions.

Another characteristic of the quantities of this bilayer system is the fact that the corresponding planes in Figs. 4.18c - 4.18f intersect. At this line there is only one possible misfit for the $PZT20/80$ top layer. The $PZT40/60$ layer is partially relaxed to the point where its lattice constant matches the value of the one belonging to relaxed $PZT20/80$. When crossing this line by further relaxing the $PZT40/60$ layer the strain on the $PZT20/80$ layer becomes tensile. This happens due to the advanced relaxation of the $PZT40/60$ layer. At this particular strain level its lattice constant becomes larger than the not strained lattice constant of $PZT20/80$. This must not be confused with the case described in Fig. 4.7. In this picture the $PZT40/60$ relaxes and just due to the tetragonal distortion of the unit cell a tensile in-plane strain arises and gives the explanation for the occurring a -domains even at a slightly compressive pseudocubic misfit. Now, the pseudocubic strain f , which is used for all calculations, becomes tensile. The tensile strain causes P_r to decrease below the value of a film with a relaxed $PZT20/80$ top layer whereas ϵ_r is increased to even higher values.

This methodology should now be applied to the cases that resemble the experimentally observed data. For the structures shown in Figs. 4.12a - 4.12d the model is assumed to include a single-domain bottom layer and a multi-domain top layer. In order to compare the measured values (given by the dots in Fig. 4.15) with these obtained via the theoretical description, the self strain-free pseudocubic strain states of the different layers must be known including the domain fractions. Since these are quite difficult to determine experimentally and vary from sample to sample, only the cases that are bordering the experimental data and observed microstructures are considered in the calculations.

The first considered case is a bilayer with a fully strained $PZT40/60$ layer (misfit at room temperature: $f_{RT} = -3.10\%$) on top of a fully strained $PZT20/80$ layer ($f_{RT} = -1.93\%$). The corresponding values for polarisation and dielectric constant are given in Figs. 4.19a and 4.19b by the red dotted line No. 1. However, the TEM image in Fig. 4.12a shows a lot of TDs in the top $PZT40/60$ layer suggesting a misfit dislocation driven relaxation of the layer. In the extreme case, this layer can be treated as fully relaxed at growth temperature where thermal strains develop upon cooling resulting in small compressive misfit at room temperature of $f_{RT} = -0.08\%$. The results are shown by line No. 2 in Figs. 4.19a and 4.19b, where P_r is smaller and ϵ_r larger compared to line No. 1.

These two lines correspond to a cross-section through the planes in Fig. 4.18a and 4.18b parallel to the axis labelled with α at the given misfit value of the *PZT20/80*. In reality, both layers will partially relax to some point, determined by the PLD growth conditions which cannot be precisely controlled or exactly measured. It has to be assumed that the measured values lie somewhere in the range between the two calculated red dotted lines. Concerning the *PZT20/80* on *PZT40/60* bilayer with domains terminated at the interface (Fig. 4.12c), the curves No. 3 and No. 4 (black lines) show the results of a relaxed *PZT20/80* ($f_{RT} = -0.08\%$) on a relaxed *PZT40/60* ($f_{RT} = -0.08\%$) and of a strained *PZT20/80* ($f_{RT} = +1.12\%$) on a relaxed *PZT40/60* layer, respectively. In this case, the film containing a strained *PZT20/80* layer exhibits a smaller P_r and a larger ϵ_r . The blue lines denoted as 3' and 4' cover the possibility of domains to propagate through both layers as shown in Fig. 4.12e. Again, these lines can be obtained by creating cross-sections of Figs. 4.18c - 4.18f. It can be seen that the influence of the a/c -domain structure on P_r is small while ϵ_r increases considerably.

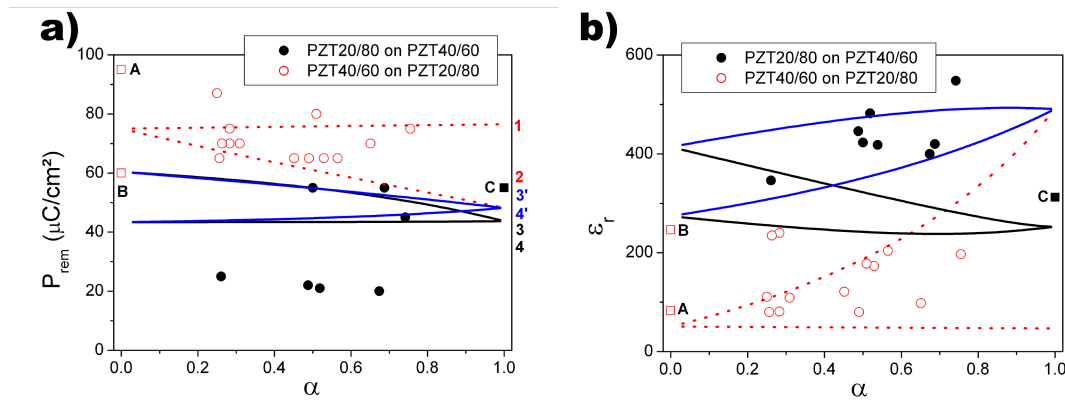


Figure 4.19: a) Remanent polarisation and b) dielectric constant of bilayers with a *PZT20/80* (○) and a *PZT40/60* bottom layer (●). □ and ■ designate single *PZT* layers consisting of strained *PZT20/80* (A), relaxed *PZT20/80* (B) and relaxed *PZT40/60* (C). The lines display the theoretical results of the LGD approach for bilayers with a *PZT20/80* bottom layer (red dotted line, 1, 2) and a *PZT40/60* bottom layer with (blue continuous line, 3', 4') and without a/c -domain walls (black continuous line, 3, 4)

Discussion: Although the properties and lattice constants of the tetragonal *PZT* compositions *PZT20/80* and *PZT40/60* are similar, the combination of both in the form of bilayers results in very different values for the remanent polarisation P_r and the dielectric constant ϵ_r when the layer sequence with respect to the substrate is changed. The main reasons for this behaviour are 1) the different lattice parameters of the two *PZT* compositions, and 2) the dependence of the misfit strain of the top layer on the relaxation state of the bottom layer. During the growth on the *STO* (100) substrate, the lattice constant of *PZT20/80* is close enough to allow a coherent growth (reported for films thinner than ca. 100 nm [13]), whereas *PZT40/60* forms dislocations to relax the strain caused by

its higher lattice mismatch with the substrate. Furthermore, the domain and polarisation states of the two layers are not independent from each other due to strain and electrostatic effects. The interface between the ferroelectric layers is the site of the mechanical and electrostatic coupling and it can, therefore, act as a barrier or favour nucleation for the formation of domains and dislocations, allowing different domain states and dislocation densities in the two layers. Ferroelectric bilayers containing *PZT20/80* as bottom layer, hence with both layers subjected to compressive stress, show high polarisation values and a low dielectric constant (curves No. 1 in Fig. 4.19). The consecutive relaxation of the *PZT40/60* (curves No. 2) and of the *PZT20/80* layer (curves No. 3) leads to a decrease in P_r and increase in ϵ_r due to the a -domains and the domain wall contribution [128]. If *PZT40/60* is grown as the bottom layer, tensile stresses can occur in the *PZT20/80* layer. In this case, P_r would further decrease and ϵ_r further increase (curves No. 4) compared to states with less tensile stress. As it is shown in Fig. 4.12f, the domains might also cross the interface. This causes a slight increase of P_r and a significant increase of ϵ_r (curves No. 3' and 4') due to the further relaxation and the contributions of the a/c -domain structure compared with the films containing the untwinned *PZT40/60* bottom layer.

For the case of α becoming zero or one, the structure entirely consists of either *PZT20/80* or of *PZT40/60*, respectively. At $\alpha = 0$ the values correspond to a *PZT20/80* film under compression without domains (curves No. 1 and 2), and twinned films under no stress (curves No. 3 and 3') and tension (curves No. 4 and 4'), respectively. On the other hand at $\alpha = 1$ the values for a *PZT40/60* film subjected to compressive stress (curves No. 1) and no stress with (curves No. 2, 3', 4') and without a -domains (curves No. 3 and 4) can be read off. These results can be compared with measurement data obtained on single layer films (■ and □ in Fig. 4.19). It turns out that the P_r value of a relaxed *PZT20/80* (designated with B) is in very good accordance with the calculations, whereas the measured P_r value of a strained *PZT20/80* layer (A) is much higher. The latter phenomenon has already been observed and reported in a previous work [108]. The computed values for a *PZT40/60* layer (C) cover the measured result and indicate a highly but not fully relaxed film. Regarding the values of ϵ_r there is a good agreement between simulation and experiment for *PZT20/80* and the calculated range includes the measured value for *PZT40/60*.

Despite the good agreement between the results of the modified LGD approach and the experiment in general, there are observable deviations of the computed values from the experimental data. These occur because the model used is still quite macroscopic in comparison to the diversity of the features in the investigated system. The major influences considered by the model are the global misfit strain and the overall electrostatic coupling between the layers. For a complete model additional effects induced by the interface between the ferroelectric layers and by the interfaces with the metal electrodes should be taken into account. Misfit dislocations that form at the interface are accompanied by local

strains and possible internal fields originating from these microstresses affecting both P_r and ϵ_r [8, 9, 10]. These misfit dislocations give rise to threading dislocations as a by-product [67] which could smear out the distribution of P_r rather than observing a single value [13, 129]. Moreover, pure electronic effects can also affect the properties. For instance, charged traps can significantly contribute to ϵ_r [42]. The presence of the 'dead layer' at the interfaces may alter the ferroelectric properties [129, 130] in addition to the possible existence of space charges, which can also change the properties of the bilayer [131]. Overall, despite the simplicity of the approach, the variations of the experimental observations can be elucidated and the effect of a -domains can be highlighted through the adopted methodology.

Summary: Different dislocation densities and domain states were induced in *PZT20/80* / *PZT40/60* bilayers grown on *SRO*-coated *STO* (100) by changing the growth sequence and the thickness of the component layers. The macroscopic properties are quite different from those measured in films comprised of individual components. Clearly, such a trend is determined by the extent of relaxation via dislocation formation and elastic domain formation as well as the electrostatic interaction between the layers. A modified LGD approach was used to provide a semi-quantitative explanation for this behaviour taking into account the misfit strains, the electrostatic coupling and the formation of an a/c -domain structure. Considering the simplicity of the model the experimental data are well described. The increase of the dielectric constant accompanied by a reduction of the remanent polarisation can be attributed to the changeover from compressive to tensile misfit strain that impacts the CURIE points of the layers. Especially, growing the *PZT40/60* as the bottom layer drives a rapid relaxation of this bottom layer, imposing a tensile strain state in the upper layer. When the upper layer experiences a tensile strain the formation of a -domains is triggered in this layer following relaxation via misfit dislocations. According to the computed results the occurrence of a -domains slows down the decrease of the remanent polarisation in the investigated strain range with increasing tensile misfit, while the domain walls give a significant contribution to the dielectric constant. This study demonstrates that functional ferroelectric structures with controlled microstructures can be fabricated via choosing the appropriate sequence of layers and their appropriate thicknesses, allowing for the possibility to tune the strain state of the system.

As discernible from Fig. 4.19 the used model fails to describe some of the experimentally determined data. Among them are the large values of the remanent polarisation for pure *PZT20/80* films which even exceed the values of the theoretically described ideal structure. Recent investigations pointed towards an unintentional doping by impurities in these *PZT* films. These indications will be traced in the following chapter. Further deviations of the experiment from the theoretical model are ascribed to interface effects.

Therefore, the interface properties will be investigated in Section 4.4 by systematically increasing the interface density.

4.3 Chromium doping of PZT20/80

As shown, our epitaxial *PZT20/80* films exhibit very high polarisation values of $P_r \approx 100 \frac{\mu\text{C}}{\text{cm}^2}$ confirming previously published results [108]. Due to the compressive in-plane strain acting on the coherent film, an enhancement of the tetragonality and implicitly of the remanent polarisation compared to the bulk value is expected, but the observed polarisation exceeds the values provided by theoretical calculations [111] and published by other groups $(70 - 85 \frac{\mu\text{C}}{\text{cm}^2})$ [65, 132].

As already reported, a small amount of foreign atoms, so-called dopants, is able to modify the properties of ferroelectric materials. The probability for the different occupancies of the various lattice sites is given by the size of the dopant ion together with the Goldschmidt factor (Eq. 2.1) [133]. The impact of certain dopant ions are known: the doping results in different piezoelectric behaviour of *PZT*, it can become either 'soft' or 'hard'. In the soft *PZT* the electromechanical coupling factor is high and the mechanical quality factor is low, whereas the hard *PZT* behaves vice versa.

A soft response is achieved by doping with donor ions (Nb^{5+} or Ta^{5+} on B-sites, La^{3+} on A-sites). It is assumed that the soft behaviour results from a reduced tetragonality [134]. An additional effect of the donor doping is a smaller leakage current because the doping reduces the number of oxygen vacancies [135].

The doping with acceptor ions (Mg^{2+} , Al^{3+} , Cr^{3+} or Fe^{3+} on B-sites) causes a hard behaviour due to additional oxygen vacancies [134]. The defects caused by negatively charged acceptor ions do not exist separately but rather form a defect pair together with the positively charged oxygen vacancy which gives rise to an electric dipole. Due to the lattice deformation this electric dipole is accompanied by an elastic dipole. Therefore this type of defect interacts both with 180° and 90° domain walls [136, 137]. The obstruction of the domain wall movement can be described by the Rayleigh law [138]. In a tetragonal ferroelectric material three qualitatively different positions for the oxygen vacancy are possible. It can be arranged to direct the dipole parallel, antiparallel or perpendicular to the spontaneous polarisation. The most probable state is the parallel direction, supporting the spontaneous polarisation [139, 140]. Due to this preferential state the dipoles orient with time in the direction of the polarisation developing an internal electric field which can partially be undone by applying a high ac-field [136, 141]. At elevated temperatures an applied external electric field facilitates the reorientation of the dipoles [142].

There are no systematical investigations on the switching time of the defect dipoles but occasional observations strongly indicate a slow process which might not be able to follow the high frequency external electric field used during the hysteresis measurements [137, 139, 143]. However, their might be doping ions which allow faster switching and increase the measured remanent polarisation.

The large impact of dopant atoms on the properties of ferroelectric materials gave rise to the assumption of impurities being present in the grown films with very high polarisa-

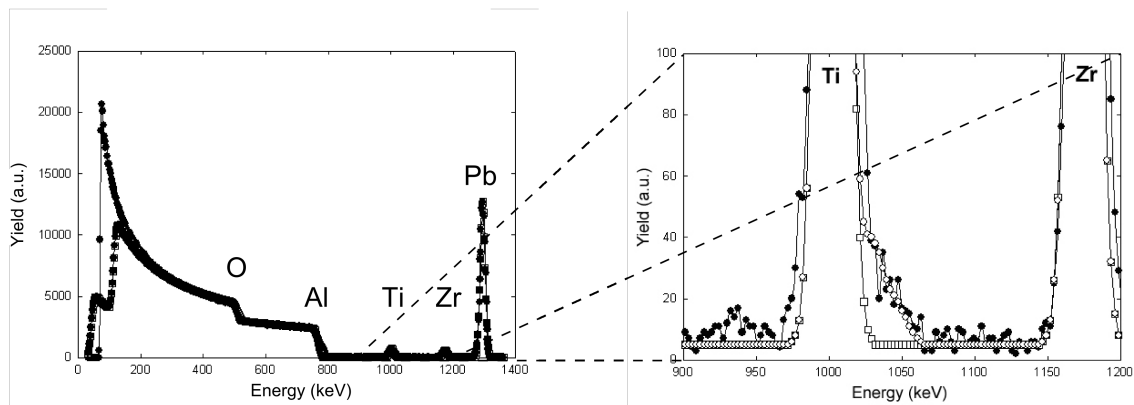


Figure 4.20: RBS spectrum of a very thin (about 15 nm) *PZT20/80* film grown onto a (0001)-oriented sapphire single crystal substrate at 575 °C (black dots), a simulation of the stoichiometric film without any contaminations (white rectangles), and the simulation of a film with composition $Pb(Zr_xTi_yCr_zMn_{z'})O_3$ (white dots). The microstructure of these films is may be worse and not comparable to the films shown in Fig. 4.6 due to the high misfit.

tion values. In order to reveal the type of the unknown atoms, the source of the impurities has to be narrowed down systematically. EDX investigations of the ceramic targets showed no other elements than *Pb*, *Zr*, *Ti* and *O*. Since no impurities were found in the targets, the composition of the films was analysed. This was done using a more sensitive method, RBS, because the small film thickness provides only a weak EDX signal. 15 nm thick *PZT20/80* films were deposited on low-*Z* substrates namely amorphous carbon and single-crystalline (0001)-oriented sapphire (Al_2O_3) to perform the RBS measurements. The films were grown onto the substrates at 575 °C just as the films grown on *STO*. The resulting RBS curve for film on the sapphire substrate is shown in Fig. 4.20. It shows three peaks and two large steps which provide two kinds of information. On the one hand the onset of the energy allows assigning the encountered element. On the other hand the width of the observed feature contains the information about the distance of the elements from the surface. Therefore, the peaks origin from the thin film whereas the steps can be attributed to the much thicker sapphire substrate. A simulation of the curve was done using the known elements *Pb*, *Zr*, *Ti*, *O*, and *Al*. This simulated curve is shown in the enlarged detail in Fig. 4.20 containing the *Ti* and the *Zr* peak. A high energy tail at the peak corresponding to the *Ti* signal is discernible which is not covered by the simulated curve. To achieve this feature in the simulation the presence of 0.6 at% of *Cr* and 0.2 at% of *Mn* has to be assumed, which results in a composition of $Pb(Zr_xTi_yCr_zMn_{z'})O_3$. RBS spectra of other films grown at elevated temperature all gave a *Cr* concentration of 0.5...1 at%. Cr^{3+} has a ionic radius of 61.5 pm which is very close to Ti^{4+} (60.5 pm) and Zr^{4+} (72 pm) compared to Pb^{2+} (119 pm); therefore it is most probably incorporated on the B-site. Comparative studies on different films showed that these impurities are restricted to samples which were grown at elevated temperatures whereas none are present in films deposited at room temperature. As a conclusion of these

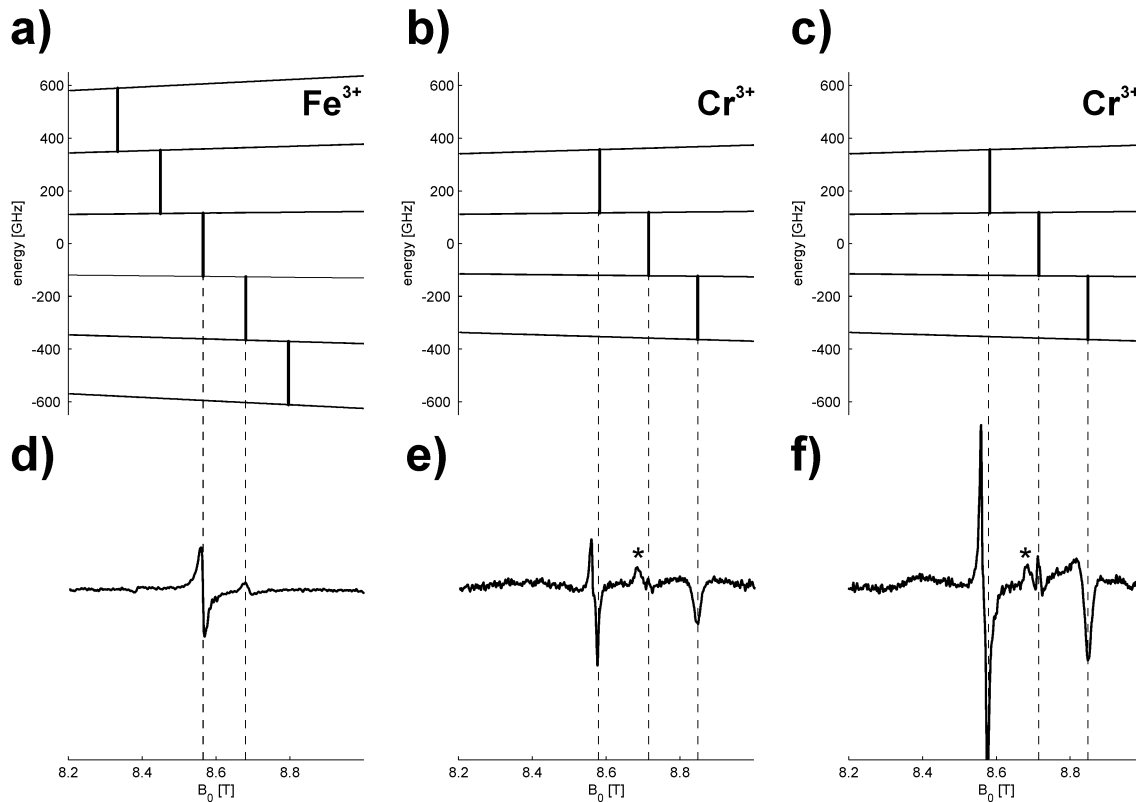


Figure 4.21: **d)** 240 GHz EPR spectra of the $SrTiO_3$ substrate as compared to **e)** unintentionally and **f)** intentionally chromium-doped $PZT20/80$ thin films recorded at 5 K. All resonances are associated to corresponding allowed ($\Delta m_S = \pm 1$) electron spin transitions (**a**, **b**, **c**). The largest resonance peak contains both the Fe^{3+} and the Cr^{3+} signal; the asterisks in **e)** and **f)** designate the non-interfering Fe^{3+} signal.

experiments we can state that there is an unintended doping of our films, most probably originating from the stainless steel holder of the substrate heater. To confirm the results and to figure out the impact of Cr doping on the surrounding $PZT20/80$ lattice, further investigations were performed using EPR.

Intentionally doped $PZT20/80$ films containing x percent of Cr ($PbZr_{0.2}Ti_{0.8}Cr_x/100O_3$, $PZT:Cr_x$) are fabricated besides nominally pure $PZT20/80$ films to allow the identification of the Cr signal by EPR. By ablating a pure $PZT20/80$ target alternately with a $Pb_{1.1}Zr_{0.18}Ti_{0.72}Cr_{0.1}O_3$ target doped films are deposited. The use of different ratios of laser pulses easily allows to achieve a controlled Cr concentration in the resulting film. More precisely this is done by sending 3 to 5 laser pulses on the $PZT:Cr10$ target every 100 pulses (which corresponds to a layer thickness of about 2 nm) sent on the $PZT20/80$ target under the conditions given in Tab. 3.1.

EPR: EPR studies were performed by varying the magnetic field from 8.2 to 9 T at a microwave frequency of 240 GHz and a temperature of 5 K [144]. Preliminary to the investigations on $PZT20/80$ films EPR measurements are performed on a bare STO substrate to identify possible parasitic signals (Figs. 4.21a and 4.21d). The obtained resonance peaks

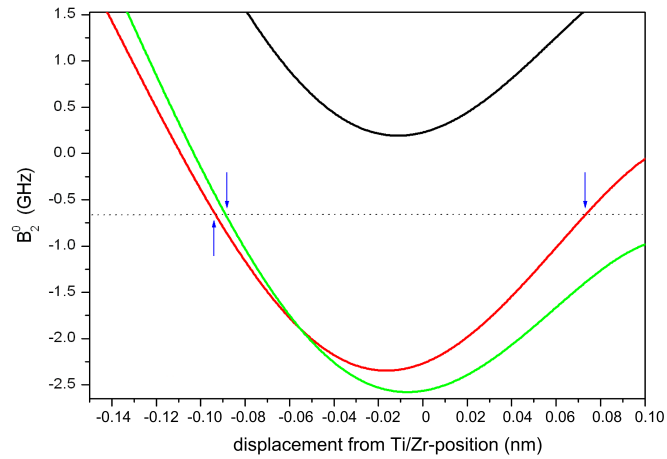


Figure 4.22: Newman superposition model analysis for B_2^0 of the chromium defect centre in PZT 20/80 thin films. The dotted horizontal line represent the experimental mean value ($B_2^0 = -0.63 \text{ GHz}$). The black line represents the NSM calculations assuming a complete octahedron, the coloured lines are for calculations with an associated oxygen vacancy with a dipole parallel (red line) and antiparallel (green line). The displacement is defined according to a line connecting O^{-2} and the B-site position, with the positive direction towards the O^{-2} position. The blue arrows mark the possible positions of the Cr^{3+} ion.

can be described by an axially symmetric fine-structure tensor with a diagonal element $B_2^0 = 0.50 \text{ GHz}$ and a g -factor of $g = 2.002$. These values correspond to Fe^{3+} centres in octahedral coordination distorted along one of the pseudo-cubic axes [145]. The value of the g -factor approximates g_e because the outermost electron shell is half filled ($[Ar] 3d^5$). Since the g -factor of Cr^{3+} is smaller due to the less filled electron shell ($[Ar] 3d^3$), the Cr^{3+} signal appears at higher fields than the Fe^{3+} signal which therefore does not interfere with the Cr^{3+} signal at high measuring frequencies. The EPR spectra obtained from unintentionally and intentionally Cr -doped PZT20/80 films are shown in Figs. 4.21e and 4.21f, respectively. Two lines appear at 8.71 T and 8.85 T in addition to the Fe^{3+} signal. These signals can be described by a single-site chromium centre of axial symmetry with $B_2^0 = 0.63 \text{ GHz}$ and $g = 1.968$, which is characteristic for a trivalent charge state. In order to determine the sign of B_2^0 , measurements below the 'polarisation temperature' have to be done. Below this temperature only the lowest energy level is occupied. It is defined by the condition that the BOLTZMANN exponent equals one. At a frequency of 240 GHz this temperature amounts to $T = \frac{h\nu}{k_B} = 13 \text{ K}$ [146]. Investigations performed at 5 K showed an increased intensity of the high field resonance identifying a negative sign of B_2^0 .

The determined value of B_2^0 is used to model the local environment of the Cr^{3+} defect centre with the help of the NSM. For comparison with the experiment two different cases are simulated with and without an oxygen vacancy in the first coordination sphere. Calculated values of B_2^0 are shown in Fig. 4.22 in dependence on the distance of the vacancy from the Cr^{3+} for a vacancy at the longest and the shortest $Cr - O$ site. The experimental results are plotted as a horizontal line together with the simulated values. Consistency can

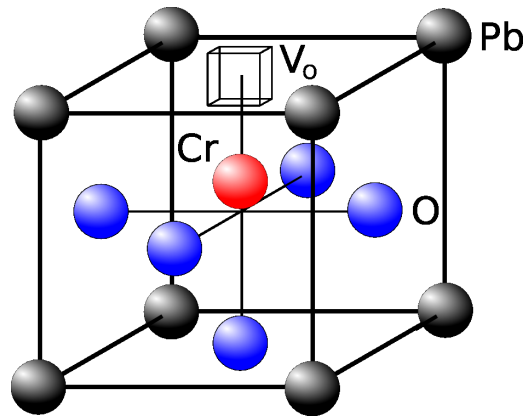


Figure 4.23: Schematic representation of the defect structure in *PZT:Cr_x*. The Cr^{3+} ion forms a defect associate with an oxygen vacancy on the nearest O-site.

only be achieved by assuming a $(Cr'_{Zr,Ti} - V_O^{\bullet\bullet})^{\bullet}$ defect associate.

DFT calculations confirm these results and show that acceptor doping generates one hole in the valence band which corresponds to a Cr'_{Ti} configuration. Further calculations on various $(Cr_{Ti} - V_O)$ defect associates reveal a strong chemical driving force for the association of Cr^{3+} with oxygen vacancies. In this configuration the O-vacancy is located at the nearest O-site along the $[001]$ axis which makes $(Cr'_{Ti} - V_O^{\bullet\bullet})_{\parallel}^{\bullet}$ the most stable charge state (Fig. 4.23). Thus the DFT calculations confirm the formation of a defect dipole along the c -axis. The orientation could be deduced both from the results of the DFT and from the axially of the FS interaction tensor. Within the sensitivity of the method a single-site Cr^{3+} centre is observed with Cr^{3+} on the B-site associated with an oxygen vacancy at the nearest O-site. This means that all defect dipoles are oriented in parallel to the spontaneous polarisation.

Microstructure: Beyond the task to serve as a reference, *PZT20/80* films with a varying Cr content allowed the systematic investigation of the influence of the Cr doping on the electrical properties to expand the picture provided by the EPR measurements [147]. TEM investigations of *PZT:Cr0.5* (Fig. 4.24) proved that epitaxial single crystalline films can be grown in the way described above. In contrast to the pure *PZT20/80* film many a -domains and threading dislocations are discernible. This indicates a strong relaxation of *PZT:Cr_x*. No trace of any individual *PZT* layers could be found in the TEM micrographs. Most probably the amount of *PZT:Cr10* ablated at each deposition step is too small to form a complete atomic monolayer. HAADF investigations were performed in order to check the local composition (Fig. 4.25a). The obtained micrographs show a regular and periodic arrangement of spots representing the atom's positions with no irregularities due to the doping. Moreover, no Cr sites in the lattice could be found which could be distinguished by a brightness contrast deviating from the host lattice. To be much more sensitive to differences in the atomic number of the atoms, local EDX measurements were

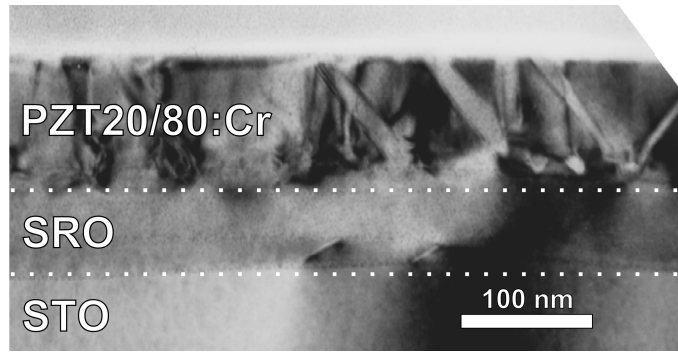


Figure 4.24: Cross-sectional TEM micrograph of $PZT:Cr_{0.5}$ with a thickness of about 100 nm grown with a SRO bottom electrode on (001)-oriented STO, seen from the [010] STO direction. In contrast to comparable films consisting of pure $PZT_{20/80}$ as in Fig. 4.6b the film shown here exhibits the characteristic signs of relaxation that is MDs, TDs and a -domains.

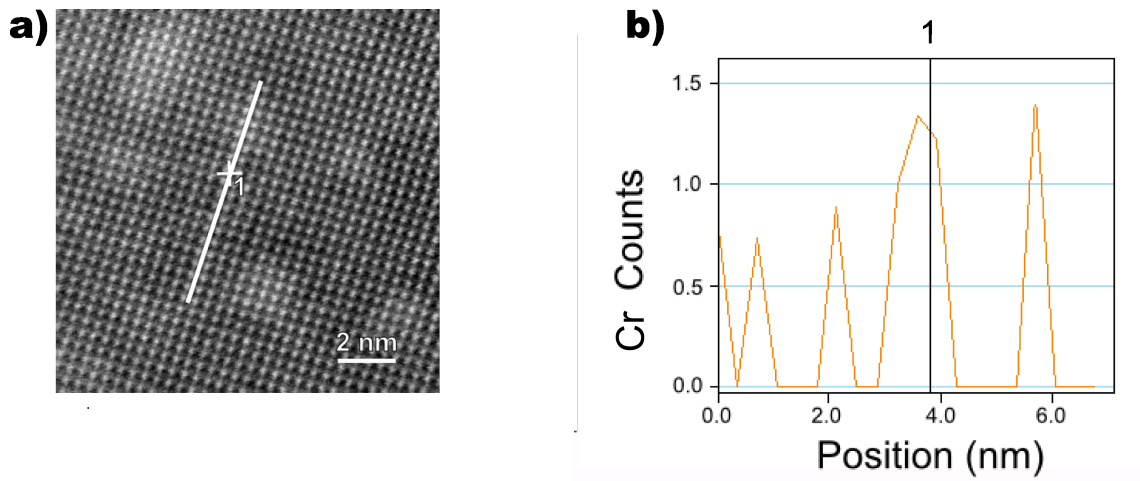


Figure 4.25: a) HAADF cross-section micrograph of a $PZT:Cr_{0.5}$ film grown on (001)-oriented STO, seen from the [010] STO direction. A well defined regular crystal lattice can be seen. The white line designates the path of an EDX line scan whose result is shown in b). This EDX scan proves the incorporation of Cr into the PZT lattice. It furthermore indicates a periodic arrangement of Cr rich layers originating from the deposition process. No extended defects are discernible in combination with the Cr rich layers as shown in a).

performed. The result of an EDX scan following the white line drawn in Fig. 4.25a is displayed in Fig. 4.25b. It clearly shows the presence of Cr in the sample which proves a successful doping of the $PZT_{20/80}$. Since the concentration is close to the detection limit of the used system the Cr profile is very rough and no quantitative determination of the Cr concentration can be made. Irrespective of the small amplitude, the Cr signal indicates a spatial dependence which points towards a periodic fluctuation of the Cr content with a periodicity of 2 nm which is consistent with the value predicted from the deposition parameters. Furthermore it shows that the diffusion length of the Cr atoms in the PZT lattice at the deposition temperature of $T = 575^\circ C$ is too short to achieve a very good homogeneity of the Cr distribution.

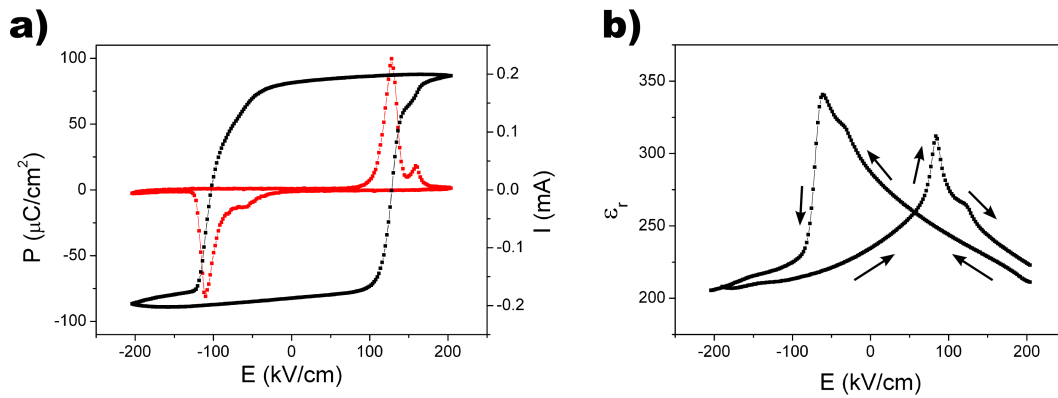


Figure 4.26: **a)** P-E hysteresis loop of *PZT:Cr0.5* (black) presented together with the accompanying switching current (red). The appearance of the hysteresis is nearly square-shaped with only slight slant when compared to the pure *PZT20/80* films (see Fig. 4.8b). The current shows sharp switching peaks which go down to about zero confirming complete switching and satisfactory low leakage current. **b)** Field dependent dielectric constant of *PZT:Cr0.5*. The asymmetry which is clearly pronounced in pure *PZT20/80* (Fig. 4.9b) is still visible but already blurred by the defects accompanying the relaxation process (see Fig. 4.24).

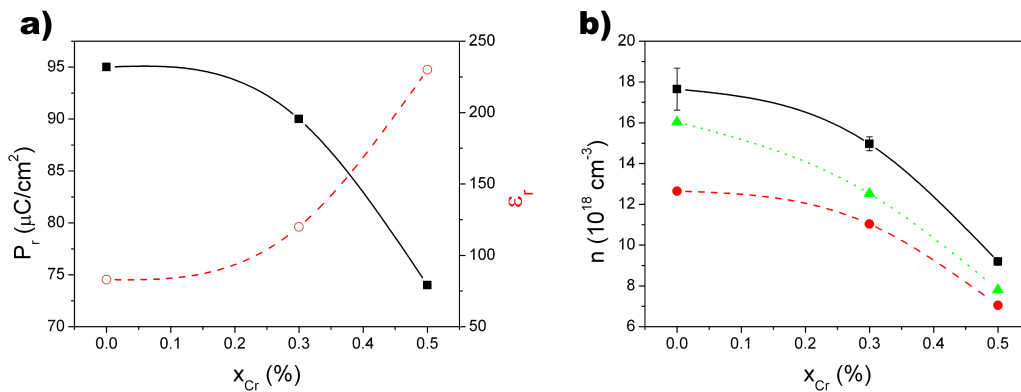


Figure 4.27: **a)** Remanent polarisation (black squares, solid line as guide for the eyes) and the dielectric constant (red circles, dashed line as guide) of *PZT:Cr* films versus the *Cr* concentration. With increasing *Cr* content the remanent polarisation decreases and the dielectric constant simultaneously increases due to the relaxation of compressive strain. **b)** Density of free charge carriers (line as guide) of *PZT:Cr* versus the *Cr* concentration. The black symbols refer to the carrier density before switching takes place. The red and the green symbols depict the measured values after switching at positive and negative voltage, respectively. The density of free charge carriers is determined from the voltage dependent capacitance. It decreases with increasing *Cr* content due to trapping and scattering of the electrons.

Electrical properties: In order to investigate the *Cr* influence on epitaxial *PZT* films, similar measurements as in the case of the pure *PZT* compositions comprising measurements of the polarisation, the dielectric constant and the leakage current in dependence on the applied voltage are performed. A typical P-E hysteresis curve of the highest doped *PZT* film (*PZT:Cr0.5*) is displayed in Fig. 4.26a together with the respective switching current. Similar to measurements on pure *PZT20/80* films, the P-E hysteresis has a nearly rectangular shape and the peaks of the accompanying switching current are steep

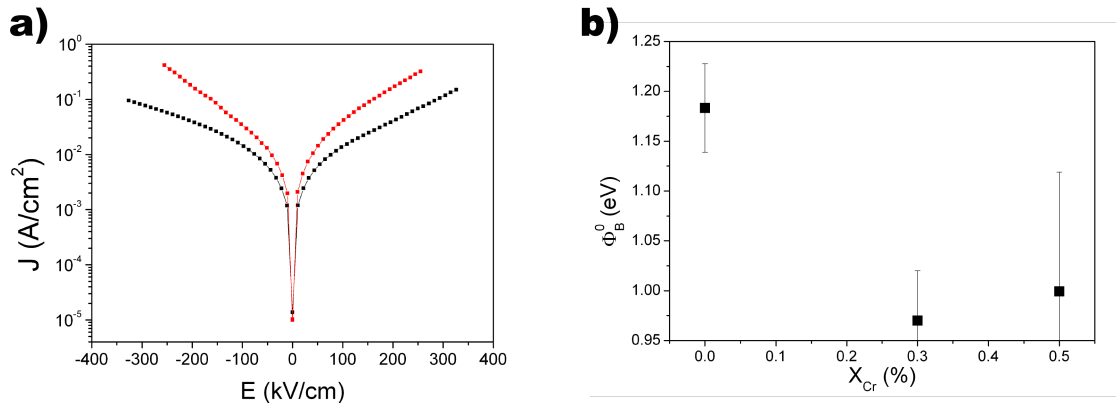


Figure 4.28: **a)** Current density of unintentionally doped *PZT20/80* (black symbols) and intentionally doped *PZT:Cr0.5* (red symbols). **b)** Height of the SCHOTTKY barrier at the interface with the electrode of *PZT:Cr x* in dependence on the *Cr* content. Both quantities can be deduced from voltage dependent measurements of the leakage current. The current density increases with doping due to the lower apparent height of the SCHOTTKY barrier reduced by interface states which allow trap-assisted tunneling and recombination through the barrier.

and clearly distinguishable from the leakage current. However, the hysteresis is slightly slanted and the remanent polarisation reaches a value of $P_r \approx 75 \frac{\mu C}{cm^2}$ which is smaller compared to pure *PZT20/80* films. The shape of the voltage dependent dielectric constant (Fig. 4.26b) resembles the shape of the non-doped *PZT20/80*. The asymmetry is still visible but less pronounced than in Fig. 4.9b. At zero volt the dielectric constant reaches $\epsilon_r \approx 230$. When the values of the remanent polarisation and of the dielectric constant are displayed in dependence on the *Cr* content, a clear trend is discernible (Fig. 4.27a): the remanent polarisation drops with increasing *Cr* content whereas the dielectric constant increases. A decreasing remanent polarisation in conjunction with an increasing dielectric constant is a typical indication for the relaxation of compressive strain. These results therefore confirm the conclusion drawn from the structural investigations, where the observed dislocations and *a*-domains suggested already the same.

Further investigations concerning the electronic properties were performed. The measured C-V curves are in-depth analysed using Eq. 4.8 to determine the density of free charge carriers. The resulting dependence of the latter on the *Cr* content is displayed in Fig. 4.27b. Either the part of the C-V curve before of after the switching peak may be used to determine the carrier density. As visible from Fig. 4.27b the carrier density is smaller directly after the switching. This effect may originate from the slow release of electrons from deep traps which are affected by the changed extent of the depletion region due to the polarisation switching. The time between the different sweep directions is long enough to release the electrons, therefore the carrier density is higher for the new sweep. This effect is less pronounced for a negative voltage. The distribution of the switching process over a wider voltage range provides more time to release the electrons from the deep traps. Irrespective on the used part of the curve, n decreases when the *Cr* content

becomes higher. To learn whether the *Cr* doping affects the conduction mechanism as observed in similar systems [148], the leakage current is measured. With increasing *Cr* content the current density increases more rapidly with increasing voltage (Fig. 4.28a).

The measured I-V curves are analysed in terms of the SCHOTTKY model. N_{eff} and Φ_B^0 are estimated from the nonlinear regression to the $J(E)$ curve using Eq. 4.9. The SCHOTTKY barrier Φ_B^0 shows a significant decrease as *Cr* is introduced (Fig. 4.28). The significant decrease of Φ_B^0 of about 0.1 eV enables a higher leakage current in the *Cr* doped *PZT20/80* in spite of the lower density of mobile charge carriers whereas no distinct dependency on the *Cr* content can be observed for N_{eff} which stays in the range of $10^{20} \dots 10^{21}\text{ cm}^{-3}$ (Tab. 4.1).

Discussion A picture of the defect structure of a *Cr* centre in ferroelectric *PZT20/80* films could be derived by the combination of spectroscopical measurements with quantum mechanical calculations. These show a strong chemical driving force for the formations of defect dipoles with an oxygen vacancy on the nearest oxygen site oriented in parallel to the spontaneous polarisation. The deduced configuration corresponds to the model known for similar bulk materials [136]. As discernible from HRSTEM investigations (Figs. 4.24 and 4.25a) it is possible to grow doped epitaxial thin films by alternating ablation of two different targets. No observable lattice defects are formed by the *Cr* doping whose presence is evidenced by EDX measurements (Fig. 4.25b). However, the formation of MDs and TDs in the doped PZT film shown in Fig. 4.24 indicates a relaxation of the compressive strain. Due to the tetragonal splitting of the lattice parameters of the PZT below the Curie temperature tensile in-plane strain arises which leads to the formation of *a*-domains. In case of the pure *PZT20/80* film the low dislocation density was explained amongst other things by the long time scale of the relaxation process. Reasons are the nucleation time of dislocations and the PEIERLS force which impedes the movement of the MDs [60]. During film growth the periodical high dopant concentration of 10 % *Cr* could cause perturbations in the lattice which enable the film to relax. These perturbations might act as nucleation sites or reduce the PEIERLS force. Therefore the addition of *Cr* initiates the relaxation of the doped PZT film at a smaller thickness compared to the pure PZT film. The possibility to modify the crystal growth by doping is well known and applied on ceramics and other polycrystalline materials [149, 150, 151, 152] but in this context it is a not intentionally generated side effect. A decreasing remanent polarisation concurrent with an increasing dielectric constant accompanies the relaxation process. Thus, it was not possible to definitely decide whether the *Cr* impurities enhance the remanent polarisation or not.

The impact of the doping on the electronic properties is a decrease of both the density of free carriers and the SCHOTTKY barrier height. These two effects have an opposing impact on the leakage current. Altogether, the lowering of the SCHOTTKY barrier dominates

and the leakage current increases as shown in Fig. 4.28a. To understand the electronic properties it has to be considered that the values of n and Φ_B^0 are governed by different areas of the film. While the density of charge carriers refers to the properties in the 'bulk' of the film, the SCHOTTKY barrier directly refers to the interface between film and electrode.

Cr on B-sites acts as an acceptor. If PZT is considered as a n-type conductor this contributes to the reduced density of charge carriers. This effect is enhanced by MDs and TDs accompanying the relaxation process and lattice deformations in the vicinity of the dopant ions which all can act as traps or scattering centres.

At the same time certain defects at the interface lower the apparent SCHOTTKY barrier height. Interface traps are formed due to the interruption of the periodic lattice structure [117]. These enable trap-assisted tunneling through the barrier or act as recombination centres allowing the charge carriers to cross the barrier and therefore apparently reduce it [118]. In the case of doped $PZT20/80$ the density of such interface states might be higher due to induced irregularities at the interface. Previous investigations revealed a decrease of the leakage current for PZT films with a fixed composition and an increasing number of defects which is reasoned by the higher density of scattering centres in the film [120]. A decrease of the SCHOTTKY barrier height was not reported which seems to be a feature specifically accompanying the described doping process. Cr is not expected to directly cause a lowering, since the barrier height is rather insensitive to doping [117]. However, since acceptor ions are responsible for the creation of additional oxygen vacancies, these could agglomerate at the Pt top electrode and reduce the barrier height. An additional effect can arise if the traps are distributed in energy. This would lead to a voltage dependent density of ionised traps which cause a more rapid increase of the current in dependence on the voltage [153]. Further contributions to the leakage current possibly arise from the TDs which partially compensate oxygen vacancies and might provide a current path due to a higher Pb concentration [13]. As discussed, the generation of defects has to be accounted for the altered properties. In this context defects denote all changes of the original lattice including replaced ions, lattice deformations, vacancies, MDs and TDs. However, the type of defects which is primarily responsible can not be exactly determined since several types might contribute simultaneously.

In spite of the observation by other groups where the formation of dipoles impedes the domain wall motion which usually leads to a higher coercive field E_C [138, 154], the investigated films behave in just the opposite manner and E_C is reduced. Probably the features present in the doped film act as nucleation sites for 180° domain walls during switching which therefore takes place at lower fields.

Summary

Epitaxial Cr -doped $PbZr_{0.2}Ti_{0.8}O_3$ films were successfully grown by PLD. The presence of Cr in the $PZT20/80$ films exhibiting the high polarisation values could be proved with

the help of RBS analysis on fabricated reference films. The overall electric polarisation of these materials is the sum of dipoles formed by displacements of charged ions inside the crystal unit cell [29] and $(Cr'_{Zr,Ti} - V_{O}^{\bullet\bullet})_{\parallel}$ defect dipoles. If the switching process of Cr proceeds fast enough, this may explain the very high polarisation values obtained. From systematically doped $PZT20/80$ films it is apparent that the addition of highly Cr -doped regions strongly influences the growth of PZT films. This results in an enhanced relaxation which in turn leads to an increase of the dielectric constant and a decrease of the remanent polarisation.

The electronic properties are modified by the Cr addition in two ways; viz. both due to the direct influence of the Cr in terms of acting as an acceptor and creating local deformations of the lattice and due to the indirect effect where defects and dislocations are caused by the relaxation process induced by the inhomogeneous Cr doping. Dependent on the location of the defects they might act as scattering centres within the film or assist in passing the SCHOTTKY barrier at the interface. This results in a reduced density of free charge carriers in the film and a lower SCHOTTKY barrier. Since the latter effect dominates, the leakage current is increased.

No reduced mobility of domain walls is indicated but the coercive field is decreased in Cr doped PZT films. In order to clarify the effect of the Cr doping excluding the impact of the relaxation process and defect formation, a series of several $PZT:Cr$ targets with varying Cr content would be necessary to grow homogeneously doped films.

4.4 Impact of increased density of interfaces

In Section 4.2 it was shown that the introduction of just one artificial interface into a *PZT* film gives rise to a dramatic change of the ferroelectric properties. This was not caused by the features of the interface but evolved due to the influence of the interface on the relaxation states of the different layers. Theoretical calculations using the LGD theory gave a good approximation of the measured values and therefore confirmed the assumed relaxational effect. However, as it can be seen from Fig. 4.19 there are still some deviations from the model used. Possible explanations given in Section 4.2 mainly referred to effects caused by a deviating structural quality of the region surrounding the interface in some films. In an attempt to separate the interface effects from the relaxational impact and to make them accessible to electrical measurements, in this chapter the density of interfaces in *PZT*20/80 / *PZT*40/60 multilayers is systematically increased [155]. The number of interfaces per nanometre N_i/t , with N_i the number of interfaces and t the film thickness, is introduced as a measure for the interface density as shown in Fig. 4.29. Both

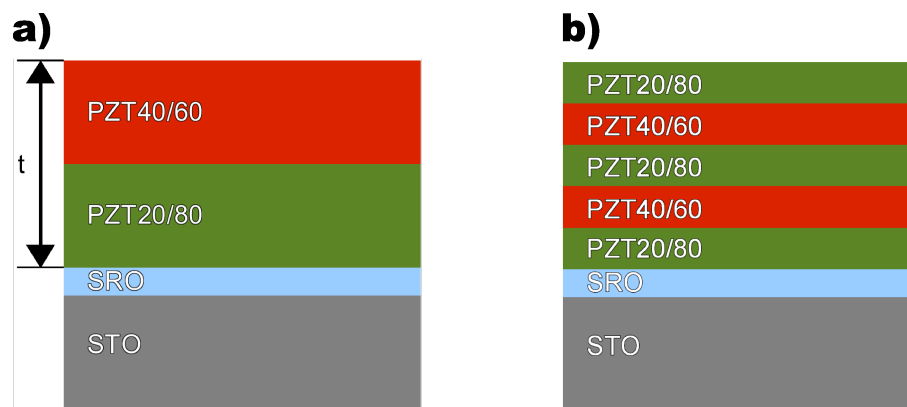


Figure 4.29: **a)** *PZT*20/80 / *PZT*40/60 bilayer as discussed in Section 4.2 and **b)** a multilayer structure consisting of 5 layers. At a hypothetical thickness $t = 100\text{nm}$ the interface density would be $N_i/t = 0.01\text{nm}^{-1}$ for the bilayer and $N_i/t = 0.04\text{nm}^{-1}$ for the drawn multilayer.

the top and the bottom layer of the multilayers consist of the same *PZT* composition to assure a symmetric structure and therefore avoid additional effects from non-symmetry. Multilayers with N_i/t ranging from 0.05nm^{-1} to 0.63nm^{-1} were manufactured.

Detailed investigations were performed on four films which cover a large range of interface densities ($N_i/t = 0.05, 0.17, 0.48, 0.63\text{nm}^{-1}$). The corresponding P-E hysteresis curves and the respective switching current are displayed in Fig. 4.30. All hysteresis curves show saturation and a similar low leakage current. The P-E hysteresis of the sample with $N_i/t = 0.05\text{nm}^{-1}$ (Fig. 4.30a) is slightly slanted whereas the other ones exhibit a nearly square shape. Also the curves of the voltage dependent dielectric constant (Fig. 4.31) show a similar shape for all investigated samples besides the one with $N_i/t = 0.05\text{nm}^{-1}$ which exhibits a broader peak of the dielectric constant accompanying the ferroelectric switching.

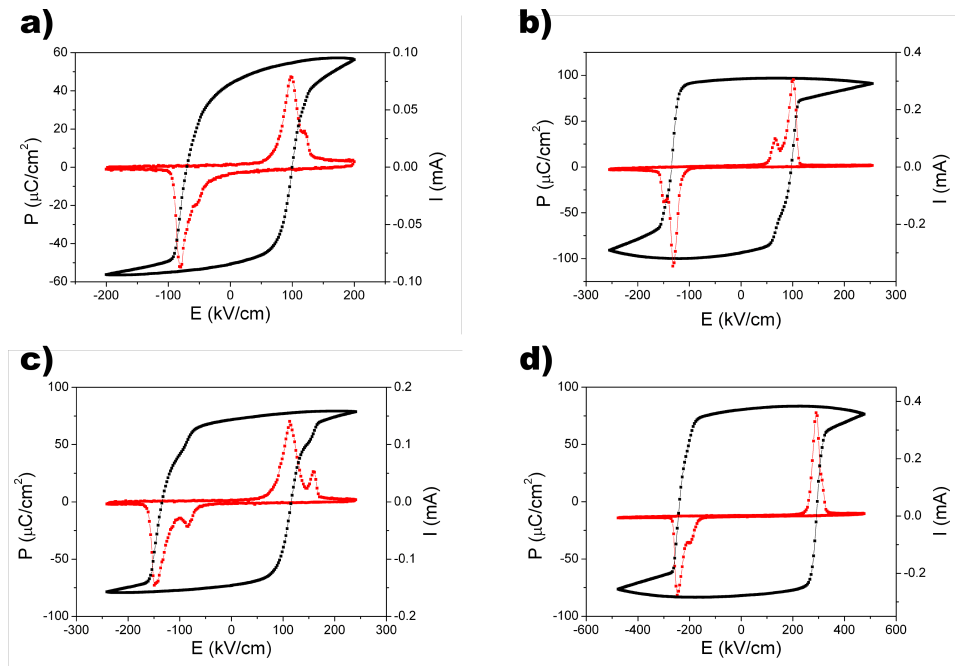


Figure 4.30: P-E hysteresis curves and respective switching current of *PZT20/80 / PZT40/60* multilayer structures. **a)** At $N_i/t = 0.05 \text{ nm}^{-1}$ the P-E curve is slanted. In case of higher interface densities (**b**, **c**, **d**) the P-E curve is nearly rectangular and shows a higher remanent polarisation compared to **a**. The pronounced peaks of the switching current in all figures demonstrate a complete ferroelectric switching in the investigated range.

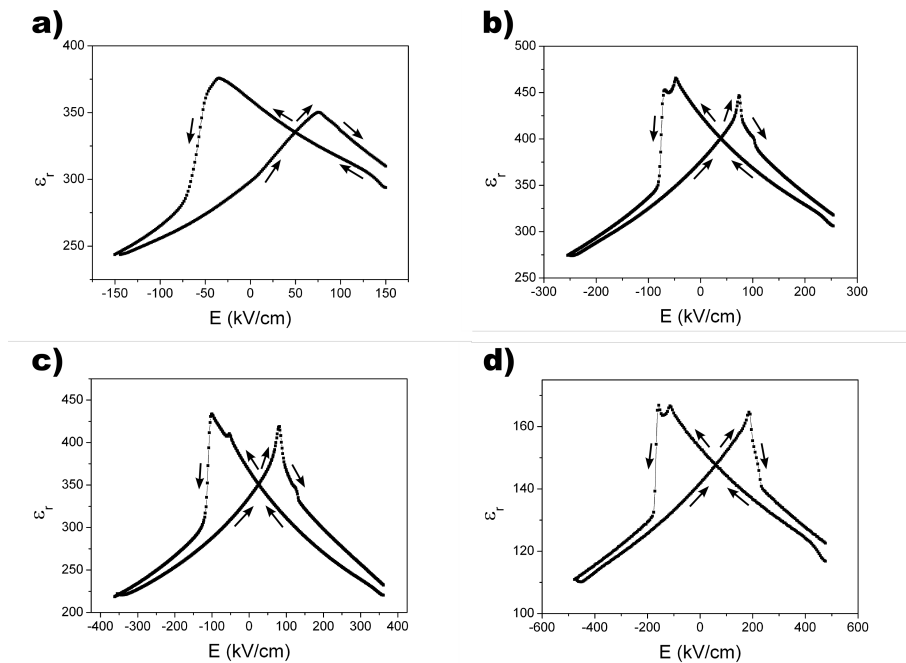


Figure 4.31: Dielectric constant in dependence on the applied electric field of *PZT20/80 / PZT40/60* multilayer structures. **a)** In case of $N_i/t = 0.05 \text{ nm}^{-1}$ broad maxima at the coercive field are discernible. The dielectric constant exhibits narrow peaks for higher interface densities (**b**, **c**, **d**) and a decreasing trend of the value at zero field.

The remanent polarisation P_r and the dielectric constant ϵ_r are measured perpendicular to the film surface on all manufactured samples. The results are summarised in Fig. 4.32a and 4.32b. The samples which are in depth investigated are marked by red circles. As it can be easily observed, the experimental values are strongly scattered. This might stem from a variation of the relaxation state. As shown in Section 4.2, a relaxation of compressive strain will result in lower values of P_r and in higher values of ϵ_r . This scattering can be drastically reduced by plotting the product $P_r \cdot \epsilon_r$, considered as a figure of merit for the ferroelectric properties (Fig. 4.33). In the simple case of a single c -domain oriented film, this product is proportional to the piezoelectric coefficients d_{31} and d_{33} [110]:

$$P_r \cdot \epsilon_r \equiv P_3 \cdot \epsilon_{33} = \frac{d_{31}}{2Q_{331}} = \frac{d_{33}}{2Q_{333}}. \quad (4.26)$$

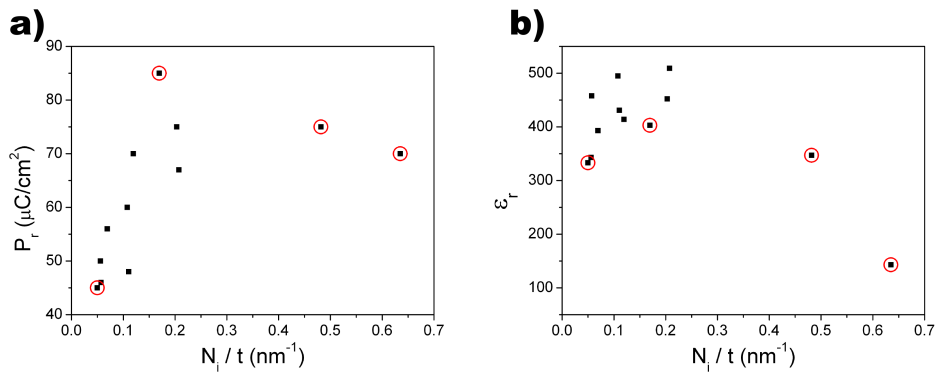


Figure 4.32: a) Remanent polarisation and b) dielectric constant in dependence on the interface density of $PZT_{20/80} / PZT_{40/60}$ multilayers. Both show a maximum around $N_i/t \approx 0.2 \text{ nm}^{-1}$. At $N_i/t < 0.2 \text{ nm}^{-1}$ the remanent polarisation show a strong increase whereas the dielectric constant only slightly increases. The decrease at $N_i/t > 0.2 \text{ nm}^{-1}$ is steep in case of the dielectric constant and gradual in case of the remanent polarisation. The red circles mark the samples which are discussed in detail.

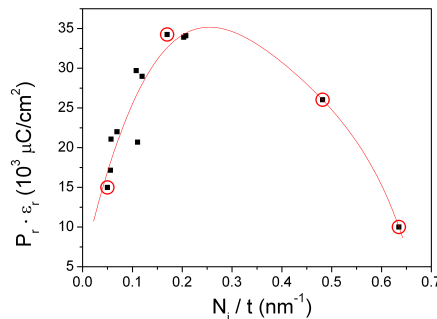


Figure 4.33: $P_r \cdot \epsilon_r$ of $PZT_{20/80} / PZT_{40/60}$ multilayers in dependence on the interface density. This product reduces the scattering observed in Fig. 4.32 and serves as a figure of merit due to its proportionality to the piezoelectric coefficients. It clearly brings out the maximum at $N_i/t = 0.2 \text{ nm}^{-1}$. The red circles mark the samples which are discussed in detail. The red line is just a guide for the eye.

In the above equation the electrostrictive coefficients Q_{331} and Q_{333} of both $PZT20/80$ and $PZT40/60$ contribute to the measured values, therefore we may define $P_r \cdot \epsilon_r$ as an equivalent piezoelectric coefficient. From Fig. 4.33 a marked dependence of $P_r \cdot \epsilon_r$ on the interface density is noticeable. The product $P_r \cdot \epsilon_r$ increases with the interface density till $N_i/t \approx 0.2 \text{ nm}^{-1}$ where it exhibits a maximum before decreasing till the end of the investigated range. In order to check for any thickness dependency, $P_r \cdot \epsilon_r$ is displayed in Fig. 4.34a together with the coercive field E_C in Fig. 4.34b. Obviously there is no

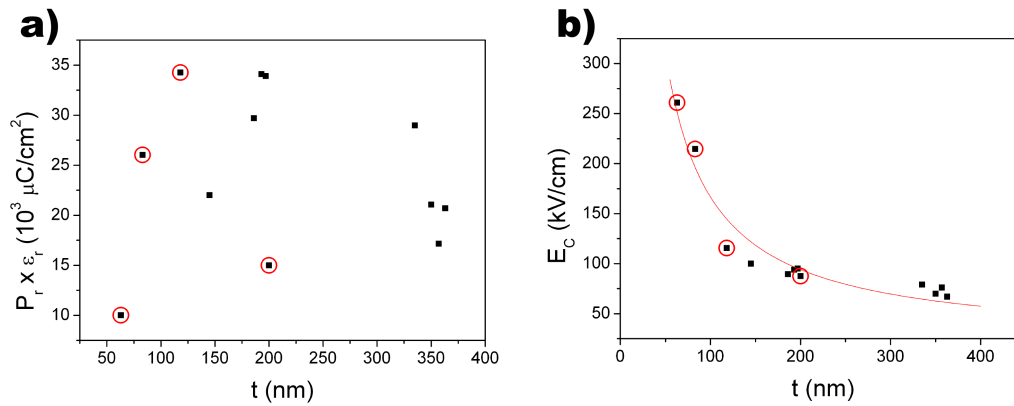


Figure 4.34: a) $P_r \cdot \epsilon_r$ and b) coercive field plotted versus the film thickness. No distinct dependence can be observed in case of $P_r \cdot \epsilon_r$. The interface density does not impact the clearly discernible $1/t$ behaviour of the coercive field. The red circles mark the samples which are discussed in detail.

pronounced thickness dependence of $P_r \cdot \epsilon_r$ whereas the coercive field scales with

$$E_C \propto \frac{1}{t}. \quad (4.27)$$

In the attempt to understand the origin of these results, structural investigations of the selected samples were performed. Through reciprocal space mapping (RSM) the in- and out-of-plane lattice constants can be determined simultaneously and thus reveal the average strain state of the layers. Additionally, RSM is potentially giving information about the fraction of a -domains [156]. In order to determine the lattice parameters by RSM, a certain diffraction peak has to be chosen. The main condition is that this peak should not be perpendicular to any of the unit cell axes, otherwise the lattice constant of this axis could not be determined. Since PZT exhibits a tetragonal structure, two axes are equal, therefore, the beam can be perpendicular to one of them without any loss of information. In this study RSM investigations using the diffraction peaks of the (204) plane were performed. From the ω and θ angles the inverse coordinates Q_x and Q_y can be determined using the relations[97]

$$Q_x = \frac{\cos \omega - \cos(2\theta - \omega)}{2} \quad (4.28)$$

and

$$Q_y = \frac{\sin \omega + \sin(2\theta - \omega)}{2}. \quad (4.29)$$

The in- and out-of-plane lattice parameters are calculated from these inverse coordinates using the wavelength λ of the X-rays and the MILLER indices h and l of the investigated plane [157]:

$$a = \frac{\lambda h}{2Q_x} \quad (4.30)$$

and

$$c = \frac{\lambda l}{2Q_y}. \quad (4.31)$$

First the samples showing the increase of $P_r \cdot \epsilon_r$ are in focus of the analysis. Figure 4.35 shows the maps of the diffraction peaks in real space for two heterostructures. The double

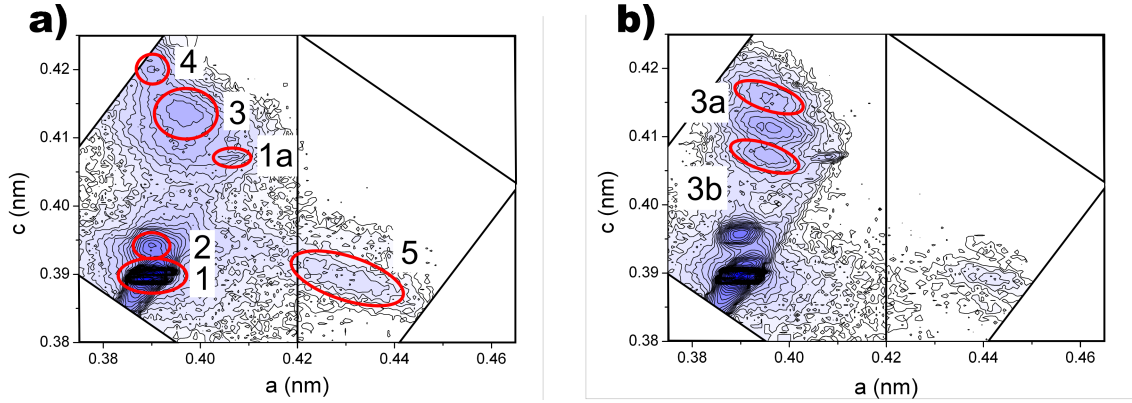


Figure 4.35: Determination of in- and out-of-plane lattice parameters of *PZT20/80 / PZT40/60* multilayers with an interface density of **a)** $N_i = 0.05 \text{ nm}^{-1}$ and **b)** $N_i = 0.17 \text{ nm}^{-1}$ grown on *STO* using a *SRO* bottom electrode by RSM around the (204) reflection of the *STO* substrate. The circles mark the peaks of the substrate (1, 1a), the electrode (2) and the *PZT* (3, 3a, 3b, 4, 5). Each of both figures consist of two measurements. The black line designates the intersection.

peak exhibiting the highest intensity (peak 1) is attributed to the *STO* substrate with contributions of both $\text{CuK}\alpha_1$ and $\text{CuK}\alpha_2$ radiations. The residual $\text{CuK}\beta$ radiation causes a further substrate peak at lower ω and θ diffraction angles (corresponding to both higher c and a lattice parameters after applying equations 4.28 - 4.31, see peak 1a) due to its shorter wavelength. Very close to the substrate's peak the reflection from the *SRO* bottom electrode is visible (peak 2). Finally, the investigated peaks of the *PZT* are labelled as peak 3, peak 4 and peak 5. Peak 3 corresponds to the contribution of the c -domain fraction of the film that has an out-of-plane polarisation. Two additional reflections occur for $N_i/t = 0.17 \text{ nm}^{-1}$ (peaks 3a and 3b) which are superlattice reflections. Peak 4 belongs to a part of the film whose in-plane lattice parameter is smaller and whose out-of plane lattice parameter is larger compared to peak 3. In case of peak 5 the proportions of the lattice parameters are interchanged with respect to the direction of the incoming X-ray

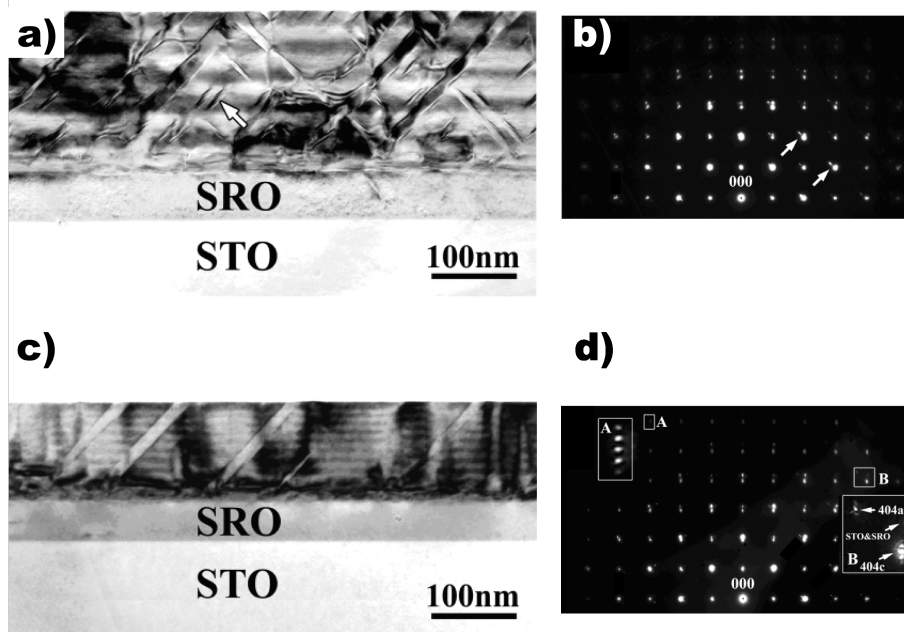


Figure 4.36: TEM cross-section micrographs and respective diffraction patterns of *PZT20/80* / *PZT40/60* multilayers with $N_i/t = 0.05 \text{ nm}^{-1}$ (a, b) and $N_i/t = 0.17 \text{ nm}^{-1}$ (c, d) seen from the [010] *STO* direction. A change in the domain pattern is observable from a to c. The diffraction peaks seen in Fig. 4.35 are also roughly visible in b and d.

beam identifying the *a*-domain part of the film.

Further on, the microstructures of these samples and respective diffraction patterns are shown in cross-sectional TEM pictures displayed in Fig. 4.36. A changeover in the 90° *a-c* domain structure is visible. In case of $N_i/t = 0.05 \text{ nm}^{-1}$ (Fig. 4.36a) various domain types, ranging from *a*-domains confined to single layers to *a*-domains propagating through several layers or even the whole film, are formed, resulting in a rather complicated domain pattern. As visible from Figs. 4.36a and 4.37, the individual *a*-domains preferentially form in the *PZT20/80* layers. The very first *PZT20/80* layer represents an exception, it is coherently grown to the substrate, no domains and dislocations can be observed therein (Fig. 4.36). TEM (Fig. 4.36c) as well as HRTEM (Fig. 4.38) show that at a reduced layer thickness the *a*-domains are not terminated at the interfaces but propagate through the whole film. The features observed in RSM are also visible in TEM diffraction patterns though with a lower resolution and concerning only a small part of the film which has been subjected to a rather rough mechanical treatment during the preparation of the cross-section TEM samples. The spot splitting due to the formation of *a*-domains can be seen in both diffraction patterns in Fig. 4.36 whereas the satellite spots (superlattice reflections) occur only in the pattern shown in Fig. 4.36d.

Again it can be noted that no dislocations are observed in the TEM micrographs of the *SRO* electrode layer, and the RSM measurements show the same in-plane lattice parameter of *SRO* like the *STO* substrate which confirms our assumption that the *PZT* is exposed to the same misfit as grown directly on *STO*.

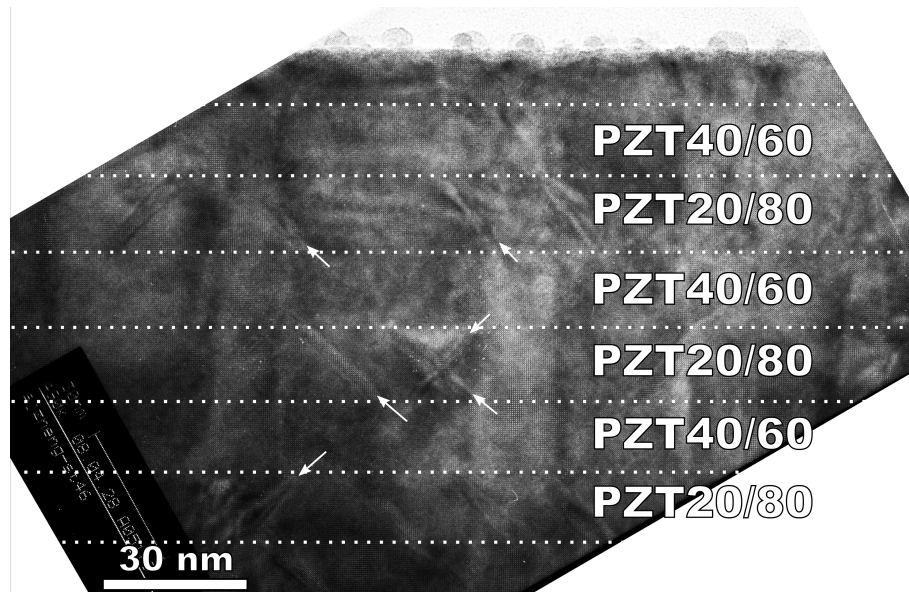


Figure 4.37: HRTEM cross-section micrographs of a film with $N_i/t = 0.05 \text{ nm}^{-1}$ seen from the [010] *STO* direction. The *a*-domains form exclusively in the *PZT20/80* layers as designated by the white arrows.

From the RSM in Fig. 4.35 it can be seen that the intensity of peak 5 (*a*-domains) is much smaller than peak 3 (*c*-domains). This indicates a lower volume fraction of *a*-domains. To make a quantitative statement about the domain fractions, it is necessary to investigate the diffraction peaks perpendicular to the surface [156]. Figure 4.39 shows the reciprocal space maps around the (400) diffraction peak of the multilayers with $N_i/t = 0.05 \text{ nm}^{-1}$ and $N_i/t = 0.17 \text{ nm}^{-1}$, respectively. Since we have previously observed a contribution of the *a*-domains as two peaks at $Q_x = \pm 0.01 \dots 0.02$ in a similar *PZT40/60* / *PZT60/40* multilayer [17], and there are no visible peaks, it might be concluded that the density of the *a*-domains is too small to give an intensity measurable by the setup used.

Now the structural properties concerning the decreasing part of the curve given in Fig. 4.33 are investigated. The results of the RSM investigation of the two corresponding multilayer structures are shown in Fig. 4.40. In the map related to $N_i/t = 0.48 \text{ nm}^{-1}$ the superlattice peaks disappeared (Fig. 4.40a). If the interface density is further increased to $N_i/t = 0.63 \text{ nm}^{-1}$ (Fig. 4.40b) peaks 3a and 3b are again visible and in spite of the much thinner layers there is no qualitative difference compared to Fig. 4.35b. The same holds for the structure visible by TEM (Fig. 4.41b). Even at this high interface density of $N_i/t = 0.63 \text{ nm}^{-1}$, which corresponds to a layer thickness of about 1.5 nm , the layers are visible and *a*-domains which propagate through the entire film thickness are present. Concerning the multilayer with $N_i/t = 0.48 \text{ nm}^{-1}$ a more careful look is necessary to understand the disappearing of the superlattice peaks. Figures 4.41a and 4.42a show different parts of the film under the same two-beam conditions (approximately by a 'symmetric row' of reflections) which would allow to see the layers parallel to the substrate's surface

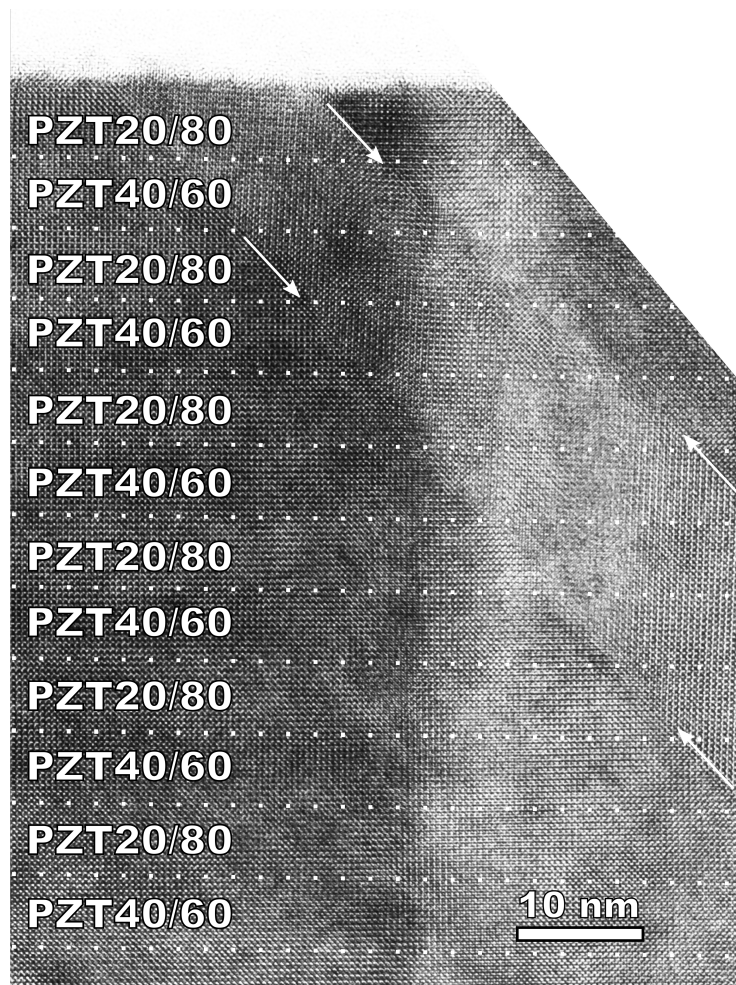


Figure 4.38: HRTEM cross-section micrograph of a film with $N_i/t = 0.17 \text{ nm}^{-1}$ seen from the [010] *STO* direction. The *a*-domains propagate through layers of both compositions. The domain walls are marked by the white arrows.

(Fig. 4.42b). Despite the correct imaging conditions the individual layers in Fig. 4.42a are hardly visible. This leads to the conclusion that in this case the interface roughness is too high for the visualisation of the layers. This might also explain the disappearing of the satellite peaks corresponding to the superlattice structure. However, when comparing $P_r \cdot \epsilon_r$ of this structure with the trend of the other ones no abnormal behaviour is observable; in this investigated system the observed variation of the interface roughness seems not to play a major role for the macroscopic properties.

Besides RSM, another possibility to compare the fraction of *a*-domains (Φ_a) of different films is provided by PFM. In PFM amplitude maps of the surface, *a*-domains show a lower response signal to the applied probing field compared to the *c*-oriented surrounding *PZT* matrix. Since only the domains which reach the top surface can be probed by PFM, this method is exclusively used on the multilayers with $N_i/t \geq 0.17 \text{ nm}^{-1}$. Representative amplitude maps of the PFM signal are shown in Fig. 4.43. In order to avoid interfering

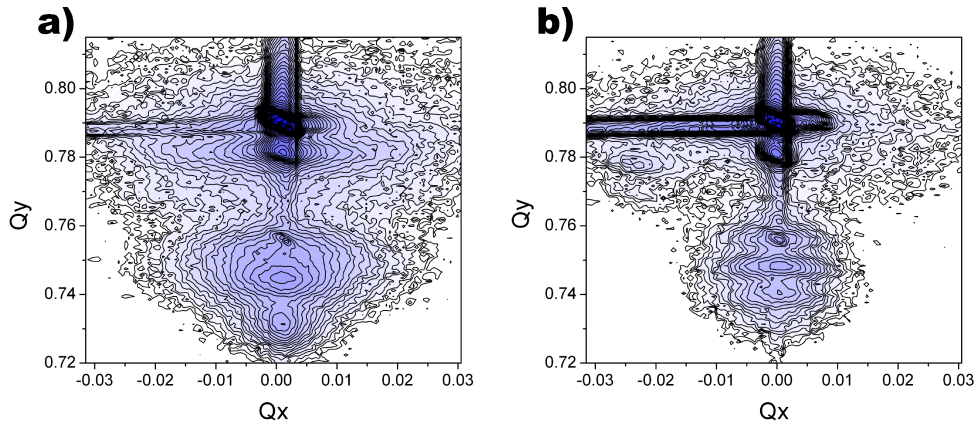


Figure 4.39: RSM around the (400) diffraction peak of *STO* showing the inverse lattice parameters of films with a) $N_i/t = 0.05 \text{ nm}^{-1}$ and b) $N_i/t = 0.17 \text{ nm}^{-1}$. No peaks of the *a*-domains are visible in this kind of measurement.

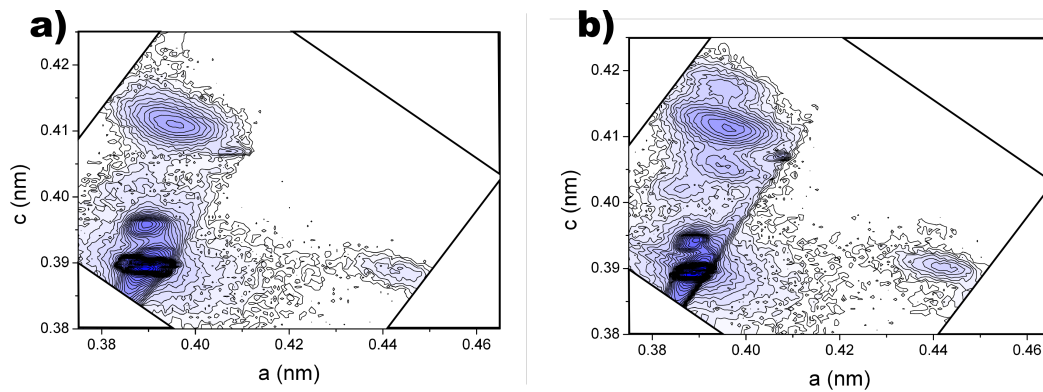


Figure 4.40: In- and out-of-plane lattice parameters of *PZT20/80 / PZT40/60* multilayers with an interface density of a) $N_i = 0.48 \text{ nm}^{-1}$ and b) $N_i = 0.63 \text{ nm}^{-1}$ grown on *STO* using a *SRO* bottom electrode determined from a RSM around the (204) reflection of the *STO* substrate. No superlattice peaks are observed for $N_i = 0.48 \text{ nm}^{-1}$ but they reappear for $N_i = 0.63 \text{ nm}^{-1}$.

contributions of 180° domain walls the imaged area was poled preliminary to the imaging scan by applying a constant voltage. The rectangularly arranged dark lines represent the traces of the *a*-domains. The fraction of *a*-domains is estimated by measuring the dark area of the images. In Fig. 4.43c three larger dark spots are observable which are artifacts from the topography and therefore are excluded during the estimation of Φ_a . The results are plotted in Fig. 4.44a, which clearly shows a decreasing domain fraction when N_i/t is increased.

However, not only the fraction but also the mobility of the domain walls has a strong influence on the macroscopic properties. To evaluate the mobility of domains the propagation of 180° domain walls with increasing poling time and field is examined. First the investigated area is uniformly poled. Afterwards the tip is placed on a certain position inside this area and a voltage opposite to the polarisation is applied to pole this spot. Subsequently the tip is moved to the next position which is then poled under slightly changed

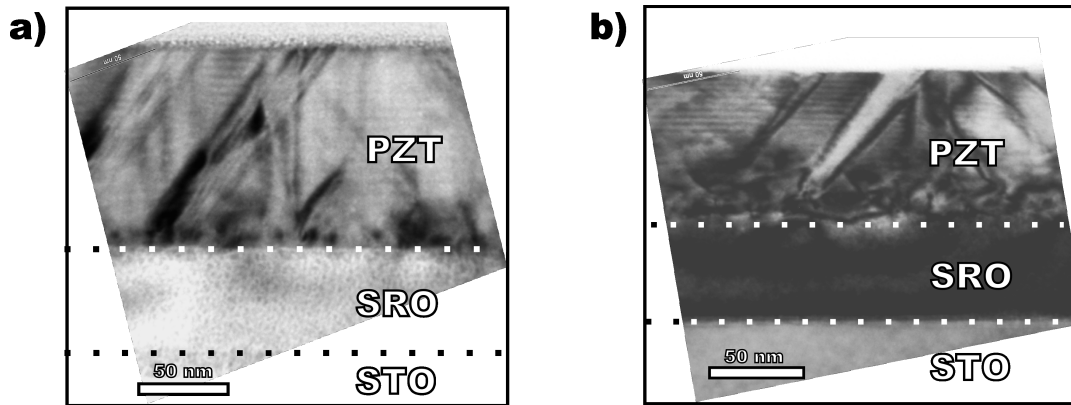


Figure 4.41: TEM cross-section micrographs of *PZT20/80 / PZT40/60* multilayers with **a)** $N_i/t = 0.48 \text{ nm}^{-1}$ and **b)** $N_i/t = 0.63 \text{ nm}^{-1}$ seen from the $[010]$ *STO* direction. No qualitative alteration is observable; the *a*-domains are propagating through the whole film and the layers are still visible.

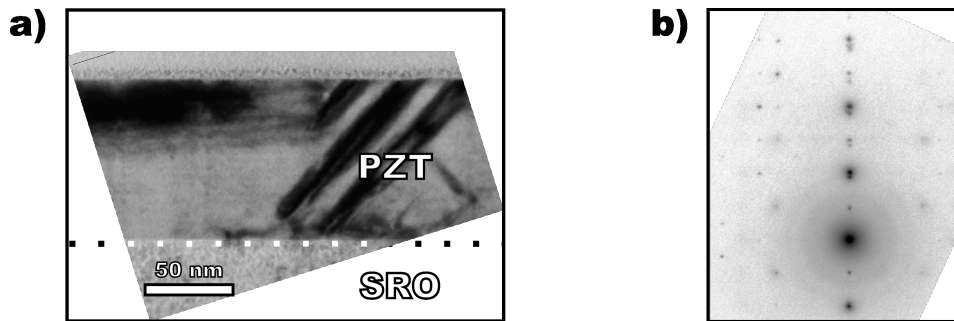


Figure 4.42: **a)** TEM cross-section micrograph and **b)** symmetric-row diffraction condition of a *PZT20/80 / PZT40/60* multilayer with $N_i/t = 0.48 \text{ nm}^{-1}$ seen from the $[010]$ *STO* direction. In spite of the same imaging conditions as in Fig. 4.41a the layers are hardly visible.

conditions. This procedure is continued until the maximum poling time or field is reached.

First the poling voltage was kept constant at $V = 3 \text{ V}$, which is well above the coercive voltage, and the poling time is varied. Figure 4.45 shows the amplitude and the phase of the PFM scan performed after the local polarisation switching. The poling time was increased as shown in Fig. 4.45b. In the amplitude image (Fig. 4.45a) the 180° domain walls are visible as dark rings around each poling point. Concerning the image of the PFM phase (Fig. 4.45b) a bright area appears at the poling spots which corresponds to a polarisation pointing upwards whereas the surrounding dark area corresponds to a polarisation pointing downwards. If the radius of the resulting area is plotted in dependence on the time a logarithmic behaviour is observable. A linear fit on semi-logarithmic plots reveals an increase of the radius which amounts to about $20 \frac{\text{nm}}{\log(s)}$ irrespective of the interface density. No differences in the velocity of the domain walls could be observed on the investigated time scale. Possible influences of the interface density could not be detected due to the fast propagation of the domain walls.

A similar experiment but with a constant poling time of $t = 1 \text{ s}$ was performed. The poling voltage was increased exactly as the poling time, that is voltages of $V = 0.1, 0.2, 0.4, 0.8, 1.6, 3.2, 6.4,$ and 10 V were used. The radius of the switched area increased linearly

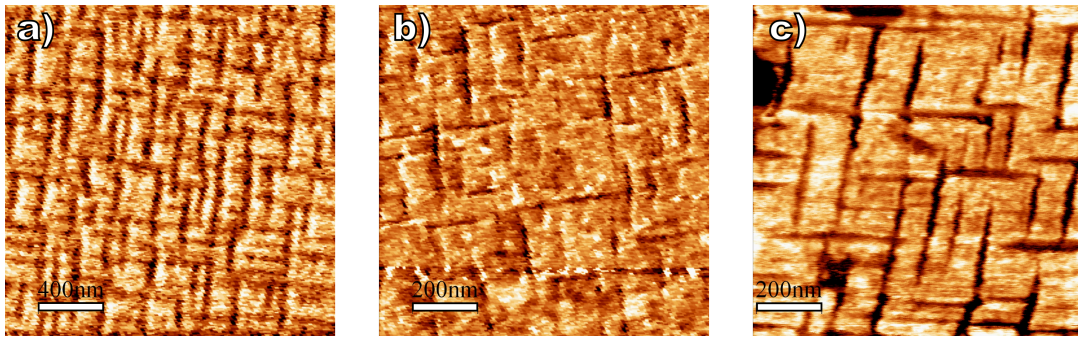


Figure 4.43: PFM amplitude maps of *PZT20/80 / PZT40/60* multilayers with a) $N_i/t = 0.17 \text{ nm}^{-1}$ b) $N_i/t = 0.48 \text{ nm}^{-1}$ c) $N_i/t = 0.63 \text{ nm}^{-1}$. The dark lines show the *a*-domains [158].

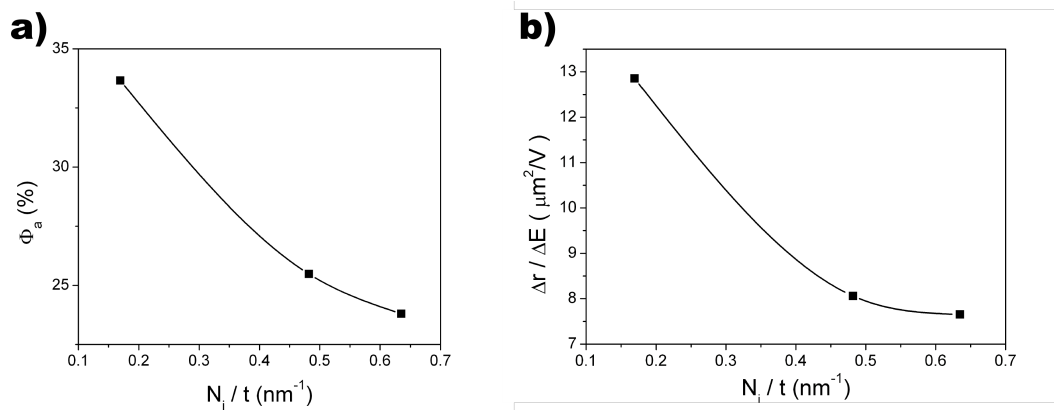


Figure 4.44: a) Fraction of *a*-domains and b) expansion rate of 180° domain walls in dependence on the interface density as determined from PFM measurements. Both decrease with increasing interface density.

with the applied electric field. A smaller area was switched as the interface density increased (Fig. 4.44b). During PFM measurements also the coercive field was investigated. As shown in Fig. 4.46, it increases with decreasing film thickness comparable to the coercive voltage determined from macroscopic measurements on electrodes (Fig. 4.34b). The increasing coercive field might explain the smaller radius of the switched area for a high interface density. The electric field around the PFM tip is very inhomogeneous. It is largest directly beneath the tip and gets weaker with increasing distance. It is possible to switch *c*-domains by 180° as long as the applied electric field is above the coercive field. Therefore, a larger area can be switched if the coercive field is lower.

Discussion: As shown above there is a distinct influence of the interface density on the macroscopic properties of *PZT20/80 / PZT40/60* multilayers. The film thickness can be excluded as the origin of this behaviour for all properties besides the varying coercive field. The dependence of the coercive field on the film thickness is usually ascribed to a thin interface layer with a constant capacitance. That layer leads to an apparent increase of the coercive field due to the decreasing field strength in the film if its thickness is decreased [24]. For films with $t < 100 \text{ nm}$ the displacement of the ions is reported to be

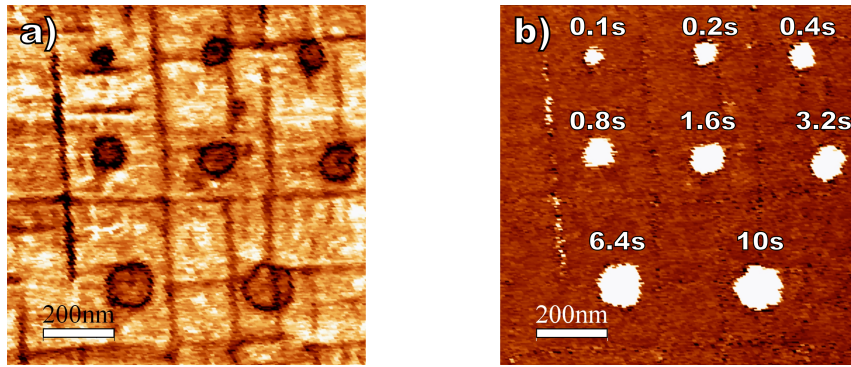


Figure 4.45: Expansion rate of 180° domain walls seen in **a)** the amplitude image and **b)** the phase image of PFM measurements. The imaged area was uniformly poled prior to the switching which results in the visible circles. The poling field was kept constant whereas the poling time was increased logarithmically from 0.1 . . . 10s.

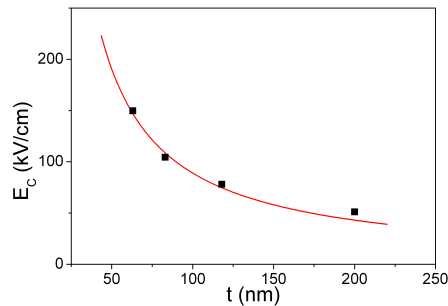


Figure 4.46: Decrease of the coercive field with increasing thickness as measured by PFM. The inhomogeneous electric field around the PFM tip switched a smaller region for thinner films due to the higher coercive field.

impeded by the epitaxial strain which could also contribute to a higher E_C in this thickness range [159].

It can be judged from both TEM and RSM investigations that there is a clear structural difference between samples with $N_i/t = 0.05 \text{ nm}^{-1}$ and $N_i/t = 0.17 \text{ nm}^{-1}$. This leads to the enhancement of the ferroelectric properties with increasing interface density in this range (Fig. 4.33). At $N_i/t = 0.05 \text{ nm}^{-1}$ the first layer consists of *PZT20/80* and is free of dislocations indicating it as fully strained to the substrate (Fig. 4.41a). This layer can be attributed to peak 4 in Fig. 4.35a. Due to the compressive in-plane strain the out-of-plane lattice parameter is increased. The lattice parameter of the subsequent *PZT40/60* layer is too large to allow a coherent growth, therefore the dislocation and domain formation starts in this layer. At these low interface densities the individual layers are able to relax to their original lattice parameter during growth. If the film is cooled down to room temperature this leads to a tensile in-plane strain acting on the *PZT20/80* layers (due to their smaller tetragonal a -axis lattice parameter compared to the *PZT40/60* layers) which causes the formation of a -domains and has a detrimental impact on the remanent polarisation of these layers. Since *PZT20/80* has a higher spontaneous polarisation than *PZT40/60* the loss of the out-of-plane polarisation of the *PZT20/80* layers leads to a considerable decrease

of the remanent polarisation of the heterostructure. Through the electrostatic coupling between the layers [125] the remanent polarisation of the *PZT40/60* layers is also reduced. The multiple strain and domain states are responsible for a broadening of peaks 3 and 5 in Fig. 4.35a, because both peaks originate from various contributions of lattice parameters distributed in the *a*- and *c*-direction. Threading dislocations, which are edge dislocations in the case of PZT [13, 70, 73], are also known to broaden the RSM diffraction peaks [97].

In case of $N_i/t = 0.17 \text{ nm}^{-1}$ the strained first *PZT20/80* layer is too thin to provide enough intensity to become visible in the RSM. The reduced thickness also prevents the individual relaxation of the layers. Therefore the layers adopt a common in-plane lattice parameter. This avoids the strong tensile strain in the *PZT20/80* layers and therefore leads to a higher remanent polarisation. Due to the high coherency of the thin layers superlattice peaks occur, which is not possible for the thicker layers at $N_i/t = 0.05 \text{ nm}^{-1}$. However, to enable the observed continuous domains also the out-of-plane lattice parameter of both *PZT* compositions has to fit each other. The similar lattice parameters of all layers might also reduce the obstruction of the domain wall movement which may contribute to an enhanced dielectric constant. The enhancement of both the remanent polarisation and the dielectric constant leads to the strong increase of $P_r \cdot \epsilon_r$.

The described changeover of the microstructure leaves its marks on all investigations. Already in the most common macroscopic measurements a qualitative difference is obvious. The hysteresis curve in Fig. 4.30a is more slanted and the peaks of the dielectric constant in Fig. 4.31a are broader compared to the others. Possibly the inhomogeneous domain pattern and relaxation state causes a rather non-uniform switching which is distributed over a range of electric field strengths and time.

In order to learn more on the crystallographic changes during the observed transition the RSM measurements are further evaluated to determine the in-plane and out-of-plane lattice constants of the multilayers. The lattice constants determined by RSM are not exact, absolute values. However, the lattice constant of bulk *STO* is well known and should not change due to the film deposition. Therefore the maps are normalised with respect to the substrate's lattice constant to determine the lattice parameters of the layers. Thus, the misfit f is considered to be invariant under this coordinate transformation. If the measured coordinate a'_s of the *STO* peak is shifted to the literature value $a_s = a'_s - \Delta a$ and the new coordinate a_f of one of the film peaks shall be calculated, the misfit f in Eq. 2.2 becomes

$$f = \frac{a'_s - \Delta a - a_f}{a_f}. \quad (4.32)$$

From Eq. 4.32 follows for the corrected value for the film peak

$$a_f = \frac{a'_s - \Delta a}{f + 1}. \quad (4.33)$$

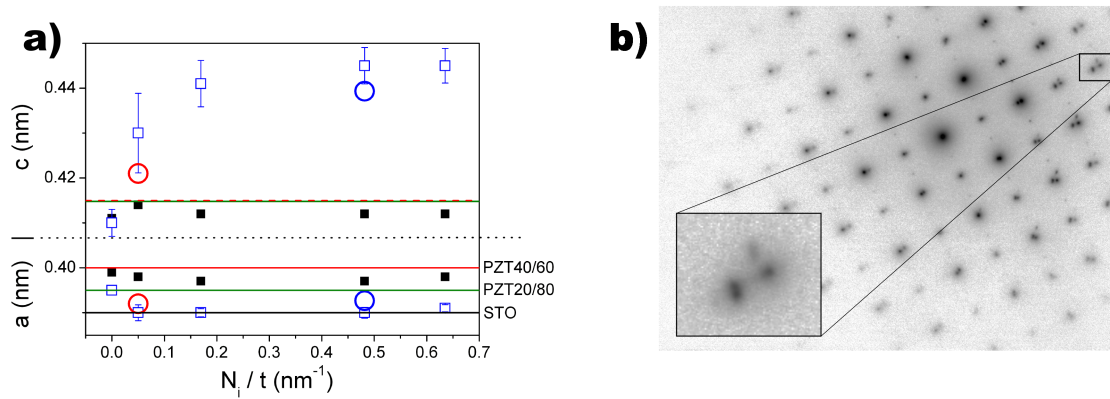


Figure 4.47: a) Average lattice parameters of *PZT20/80* / *PZT40/60* multilayers. The c - and a -domains are designated by black full squares (■) and blue open squares (□), respectively. For comparison the nominal tabular values of the bulk crystals of *STO* (black line), *PZT20/80* (green lines) and *PZT40/60* (red lines) are shown. The red circle (○) at $N_i/t = 0.05 \text{ nm}^{-1}$ refers to the strained part of the film whereas the blue circle (○) at $N_i/t = 0.48 \text{ nm}^{-1}$ refers to the lattice parameter of the a -domain determined from the TEM diffraction pattern shown in **b**).

In this way the absolute values of the film lattice parameters can be measured and their shift with increasing interface density can be followed.

Figure 4.47a summarises the lattice parameters as determined from RSM. The lattice parameters a and c of both the c -domains and the a -domains are plotted in dependence on the interface density together with the ones of a pure *PZT40/60* film ($N_i/t = 0 \text{ nm}^{-1}$). They are shown in comparison to the bulk values of *STO*, *PZT20/80* and *PZT40/60*. The error bars are estimated from the variation of the diffraction peak to be the radius of the corresponding peak both in the c - and a -direction. This results in large error bars for the large axis of the a -domains. In most other cases the resulting error is smaller than the drawn symbol.

The values of both lattice parameters of the c -domain hardly change when increasing the interface density. In case of lattice parameter a the determined value stays between the bulk values of *PZT20/80* and *PZT40/60* due to the elastic coupling of both the layers of two *PZT* compositions. This value is higher than the substrate's lattice parameter; the film is obviously not fully strained to the substrate. The whole ferroelectric structure is partially relaxed because the critical thickness for the formation of MDs is exceeded. The out-of-plane lattice parameter c determined from RSM is slightly smaller than the bulk values. This might be facilitated by the expanded in-plane lattice parameter of the *PZT20/80* which would lead to a smaller out-of-plane lattice parameter. Furthermore the thin film lattice parameters are compared with the bulk values which don't necessarily have to be in congruence. One exception from the relaxed state is shown as a red circle (○) at $N_i/t = 0.05 \text{ nm}^{-1}$ in Fig. 4.47a. It originates from peak 4 in Fig. 4.35a which was attributed to the first *PZT20/80* layer. This layer appears to be at least partially strained with an in-plane lattice parameter close to the substrate. The disappearance of peak 4,

when the interface density is increased, demonstrates the formation of the common strain state in most of the multilayer.

Concerning the lattice parameters of the a -domains it is noticeable that due to the RSM their out-of-plane lattice parameter a fits perfectly that of STO whereas the in-plane lattice parameter c is increased considerably. To understand this, we recall that in case of the a -domains two different in-plane lattice parameters exist. One of them (c) is parallel and the other one (a) is perpendicular to the polarisation. The lattice parameter c is larger than a due to the tetragonal distortion. Judging from the experimental results it has to be assumed that the in-plane lattice parameter a is strained to that of the substrate. Due to the tetragonality of the unit cell the out-of-plane lattice parameter a has to be identical to the in-plane parameter a . Accompanying this reduction of both lattice parameters a , the in-plane lattice parameter c increases. Remarkably is the much larger value of this lattice parameter compared to the bulk values. TEM diffraction patterns (Fig. 4.47b) are utilised to check the RSM results. Despite the higher error of this method the large lattice constant of the a -domains can be verified (blue circle \circ at $N_i/t = 0.48 \text{ nm}^{-1}$ in Fig. 4.47a).

In order to double-check the correctness of the large value of the lattice parameter c of the a -domains, the POISSON ratio can be determined. Since always average values for $PZT20/80$ and $PZT40/60$ are determined, the change of the lattice parameters will be compared with the averaged bulk values of $a = 0.3975 \text{ nm}$ and $c = 4149 \text{ nm}$. The lattice parameter a of the a -domain changes only slightly to an average value of about $a = 0.39 \text{ nm}$ whereas the lattice parameter c significantly increases to about $c = 0.442 \text{ nm}$. Therefore a tensile strain on the lattice parameter c must be assumed. In this way a POISSON ratio of $\nu = 0.29$ is calculated which is slightly smaller than the averaged value of ceramics ($\nu_{PZT20/80} = 0.29$, $\nu_{PZT40/60} = 0.34$) [160]. The good agreement with these tabulated values supports our assumptions.

As shown in Fig. 4.47a the elongation of the lattice parameter c of the a -domains does not occur for a single composition film. Moreover, it increases with the interface density up to $N_i/t = 0.17 \text{ nm}^{-1}$. This behaviour follows the structural transition described above. Possibly it is energetically favourable to strain the lattice parameter c of the existent a -domains in the multilayers with $N_i/t \geq 0.17 \text{ nm}^{-1}$ rather than to introduce additional a -domains. This process would be facilitated by the compressive stress acting on the in-plane lattice parameter a induced by the substrate. If the in-plane lattice parameter a matches the substrate lattice parameter a further compression is no longer supported and consequently the formation of a new a -domain becomes favourable. No further change of the lattice parameters is observed for $N_i/t > 0.17 \text{ nm}^{-1}$; the described process seems to be already finished at this interface density.

The polarisation of the a -domains should be increased due to the higher tetragonality which could also increase the polarisation of the c -domains via the electrostatic coupling at the domain walls to avoid charging [124].

Although no microstructural changes are observed by TEM and RSM measurements, $P_r \cdot \epsilon_r$ decreases if the interface density is increased above about 0.2 nm^{-1} . PFM measurements reveal a decreasing Φ_a with increased interface density. This points to a higher residual compressive strain in the whole multilayer [124]. A more compressive strain leads to a decrease of the dielectric constant. However, the difference is too small to be observed by the other investigation methods, which indicates this effect to be not sufficient to explain the drastic drop of $P_r \cdot \epsilon_r$. No quantitative statements can be made concerning the mobility of the domains walls. Their propagation seems to proceed faster to be observed within the used poling times of $t \geq 0.1 \text{ s}$. The varying area of the switched region might result from the inhomogeneous field applied by the tip. With increasing distance from the tip the electric field decreases. If the coercive field increases, the area around the tip where this threshold field is reached is decreased.

The properties of the interfaces might be responsible for the deterioration of $P_r \cdot \epsilon_r$. Although the interfaces are smooth they remain distinguishable in TEM which demonstrates residual lattice distortions. If the interface density is increased above 0.2 nm^{-1} the higher volume fraction of features like interface defects and dislocations may result in a deterioration of both P_r and ϵ_r by local strains and charge effects [10, 12]. These distortions could reduce the mobility of the domains or pin them [13, 128] which would also contribute to a smaller dielectric constant.

Summary In epitaxial multilayer structures a changeover to a common strain state of all layers is observed, if the interface density is increased to a value of about 0.2 nm^{-1} . This avoids the formation of tensile strain in the *PZT20/80* layers as observed for smaller interface densities. Therefore the remanent polarisation is increased. Furthermore the tight coupling of both compositions smoothens the interfaces. This causes the *a*-domains to propagate through the whole film and may also reduce the obstruction of the domain wall movement causing an enhanced dielectric constant. If the interface density is increased above 0.2 nm^{-1} , the relaxation of the compressive epitaxial strain introduced by the substrate to the film can be somewhat further suppressed. However, the high volume fraction of the distorted interface regions leads to a drop of $P_r \cdot \epsilon_r$ which might be amplified by a reduced mobility of the domain walls.

5 Summary

In this work the impact of artificially introduced modifications in the form of interfaces, dislocations and doping on the microstructural and macroscopic properties of epitaxial *PZT40/60* and *PZT20/80* thin films was elucidated. To achieve this goal, heterostructures with a controlled dislocation and domain structure were fabricated by pulsed laser deposition. Comprehensive microstructural investigations and a careful analysis of the resulting electric properties were performed. The experimental findings were theoretically evaluated by means of the SCHOTTKY model and the LANDAU-GINZBURG-DEVONSHIRE theory.

In case of single composition layers the properties are determined by the in-plane lattice constants of film and substrate. These allow a nearly coherent growth of *PZT20/80* on *STO*. A higher leakage current is observed for a *PZT40/60* film. The larger in-plane lattice parameter of the latter causes a high density of dislocations which strongly alter the properties by the relaxation of compressive strain and also by the formation of 90° *a-c* domain walls. These changes increase the dielectric constant and decrease the remanent polarisation, compared to the *PZT20/80* film.

PZT20/80 films were observed to exhibit extraordinarily high values of the remanent polarisation. Motivated by the detection of Cr^{3+} ions in thin film heterostructures containing a ferroelectric *PZT20/80* layer, the properties of *PZT20/80* were tuned by systematic *Cr* doping. It turned out that the utilised layer-wise doping facilitated the usually sluggish dislocation formation which caused an advanced relaxation of the doped *PZT20/80* films. Moreover *Cr* is known to form defect associates with oxygen vacancies. This gives rise to defect dipoles whose preferential orientation is parallel to the remanent polarisation of the *PZT20/80*. The simultaneous generation of doping centres and dislocations prevents the clear attribution of the altered properties. However, it can be assumed that the relaxation process increases the dielectric constant and decreases the remanent polarisation. The latter would compensate for any enhancing effect of the doping on the remanent polarisation. Changes of the electronic properties, probably induced by the doping, cause a higher leakage current. An increase of the coercive field, which has been reported to be caused by the described defect dipoles [138, 154], was not observed.

In order to investigate the modifications caused by an additional interface within the ferroelectric film, bilayers consisting of *PZT20/80* and *PZT40/60* were fabricated. This released the direct coupling of the top layer to the substrate. The strain exposed to the

top layer becomes exclusively determined by the relaxation state of the bottom layer. Depending on the sequence of the *PZT* layers a clear gap in the values of the remanent polarisation and the dielectric constant arises. A theoretical approach, using the LANDAU-GINZBURG-DEVONSHIRE theory, was applied to understand the results. By a combination and modification of previous models it was possible to describe the large difference in properties observed for different cases. In addition, the variation of the values in dependence on the thickness ratio of the layers could be explained for most bilayers. Both effects are caused by an interplay of the different dislocation and *a-c* domain states as well as by the influence of both layers, weighted by the relative thickness, which are connected via mechanical and electrostatic coupling.

A stronger impact of the interface properties together with a closer coupling of the *PZT* layers was induced by increasing the density of interfaces. At low interface densities a relaxation of the individual layers was observed which caused the formation of *a*-domains in the *PZT20/80* layers. This has a detrimental influence on the remanent polarisation of the multilayer. The resulting dielectric constant is comparable to *PZT40/60* films.

With increasing interface density the individual relaxation of the layers is increasingly suppressed. This leads to a closer coupling of the layers which adopt common lattice parameters. Consequently the dominating influence of the bottom layer observed in bilayers, which caused the described gap, is circumvented. No difference of the remanent polarisation and the dielectric constant of multilayers with different bottom layer can be found. Due to the matching lattice parameters the *a*-domains cross the entire film. Since *a*-domains are no longer confined to small parts of the film they might more easily respond to an electric field and the dielectric constant increases. As a further consequence of the common strain state, the strong tensile strain on the *PZT20/80* layers is reduced which leads to a higher remanent polarisation.

A surprising feature is a largely increased *c*-axis lattice parameter of the *a*-domains in multilayers with an interface density high enough to exhibit a common strain state. Due to the high coherency of the layers it seems to be energetically favourable to further strain the *c*-axis of the existent *a*-domains than to introduce additional *a*-domains. Compared to single composition films and to bilayers, the remanent polarisation amounts to high values but stays below the value of a pure *PZT20/80* film. The dielectric constant is still exceeded by those bilayers which also show domains that propagate through the whole film. However, due to the simultaneous occurrence of high values of the remanent polarisation as well as the dielectric constant, the product of both, which is proportional to the piezoelectric coefficient, is much higher in multilayer films at a certain interface density.

If the interface density is further increased after having reached a common state, this has a deteriorating impact on the properties. It is assumed that the high volume fraction of the distorted region around the interfaces is responsible for this behaviour.

To shortly summarise, it has been shown that the number of interfaces controls the relaxation state of the ferroelectric heterostructures. At small interface densities various combinations of strained and relaxed layers can be realised to create films exhibiting either a high remanent polarisation or a high dielectric constant. If the density of interfaces is sufficiently large the heterostructure exhibits a common strain state. This allows high piezoelectric coefficients due to the combination of the properties of different materials without the dominating relaxational effect. Care has to be taken not to increase the interface density too much since the distorted regions close to the interfaces deteriorates the properties of the whole film.

The findings of this work may directly contribute to various modern research topics. Multiferroics are at the moment in the focus of extensive investigations [161, 162, 163, 164, 165, 166, 167]. Since materials which intrinsically exhibit both ferroelectric and ferromagnetic properties are rare [168], great attention is paid to the creation of superstructures which combine ferroelectric and ferromagnetic properties through mechanical and possibly electronic coupling. In order to effectively exploit the properties of the combined materials a very close coupling is necessary [169]. The presented work clarifies the impact of the relaxation processes in heterostructures and how to utilise them in order to tune the resulting properties. Moreover the processes arising due to an intimate coupling of the layers at a high interface density are revealed. These results may contribute to future efforts to understand and systematically fabricate thin film multiferroic heterostructures.

Bibliography

- [1] C. Pulvari: Memory matrix using ferroelectric condensers as bistable elements. *J. ACM* **2** (1955), 169.
- [2] P. Muralt: Ferroelectric thin films for micro-sensors and actuators: A review. *J. Micromech. Microeng.* **10** (2000), 136.
- [3] O. Auciello: Science and technology of thin films and interfacial layers in ferroelectric and high-dielectric constant heterostructures and application to devices. *J. Appl. Phys.* **100** (2006), 051614.
- [4] J. F. Scott: Applications of modern ferroelectrics. *Science* **315** (2007), 954.
- [5] P. S. Waggoner and H. G. Craighead: Micro- and nanomechanical sensors for environmental, chemical, and biological detection. *Lab Chip* **7** (2007), 1238.
- [6] N. Setter and R. Waser: Electroceramic materials. *Acta Mater.* **48** (2000), 151.
- [7] P. Muralt: Piezoelectrics in micro and nanosystems: Solutions for a wide range of applications. *J. Nanosci. Nanotechnol.* **8** (2008), 2560.
- [8] S. P. Alpay, I. B. Misirlioglu, V. Nagarajan, and R. Ramesh: Can interface dislocations degrade ferroelectric properties? *Appl. Phys. Lett.* **85** (2004), 2044.
- [9] M. W. Chu, I. Szafraniak, R. Scholz, C. Harnagea, D. Hesse, M. Alexe, and U. Gösele: Impact of misfit dislocations on the polarization instability of epitaxial nanostructured ferroelectric perovskites. *Nat. Mater.* **3** (2004), 87.
- [10] I. B. Misirlioglu, A. L. Vasiliev, M. Aindow, and S. P. Alpay: Strong degradation of physical properties and formation of a dead layer in ferroelectric films due to interfacial dislocations. *Integr. Ferroelectr.* **71** (2005), 67.
- [11] V. Nagarajan, C. Jia, H. Kohlstedt, R. Waser, I. Misirlioglu, S. Alpay, and R. Ramesh: Misfit dislocations in nanoscale ferroelectric heterostructures. *Appl. Phys. Lett.* **86** (2005), 192910.
- [12] I. Misirlioglu, S. Alpay, M. Aindow, and V. Nagarajan: Thermodynamic and electrostatic analysis of threading dislocations in epitaxial ferroelectric films. *Appl. Phys. Lett.* **88** (2006), 102906.
- [13] I. Vrejoiu, G. LeRhun, N. D. Zakharov, D. Hesse, L. Pintilie, and M. Alexe: Threading dislocations in epitaxial ferroelectric $\text{PbZr}_{0.2}\text{Ti}_{0.8}\text{O}_3$ films and their effect on polarization backswitching. *Philos. Mag.* **86** (2006), 4477.
- [14] D. Hesse and M. Alexe: Interfaces in nanosize perovskite titanate ferroelectrics - Microstructure and impact on selected properties. *Z. Metallkd.* **96** (2005), 448.

- [15] D. G. Schlom, L.-Q. Chen, C.-B. Eom, K. M. Rabe, S. K. Streiffer, and J.-M. Triscone: Strain tuning of ferroelectric thin films. *Annu. Rev. Mater. Res.* **37** (2007), 589.
- [16] B. S. Kwak, A. Erbil, J. D. Budai, M. F. Chisholm, L. A. Boatner, and B. J. Wilkens: Domain formation and strain relaxation in epitaxial ferroelectric heterostructures. *Phys. Rev. B* **49** (1994), 14865.
- [17] I. Vrejoiu, Y. Zhu, G. Le Rhun, M. A. Schubert, D. Hesse, and M. Alexe: Structure and properties of epitaxial ferroelectric $\text{PbZr}_{0.4}\text{Ti}_{0.6}\text{O}_3/\text{PbZr}_{0.6}\text{Ti}_{0.4}\text{O}_3$ superlattices grown on SrTiO_3 (001) by pulsed laser deposition. *Appl. Phys. Lett.* **90** (2007), 072909.
- [18] F. A. Urtiev, V. G. Kukhar, and N. A. Pertsev: Phase diagrams of single-domain ferroelectric-dielectric superlattices. *Appl. Phys. Lett.* **90** (2007), 252910.
- [19] Y. L. Li, S. Y. Hu, D. Tenne, A. Soukiassian, D. G. Schlom, X. X. Xi, K. J. Choi, C. B. Eom, A. Saxena, T. Lookman, Q. X. Jia, and L. Q. Chen: Prediction of ferroelectricity in $\text{BaTiO}_3/\text{SrTiO}_3$ superlattices with domains. *Appl. Phys. Lett.* **91** (2007), 112914.
- [20] M. Okuyama, K. Yokoyama, and Y. Hamakawa: Analysis of non-volatile polarized memory of semiconductor-ferroelectric heterostructure junction. *Jpn. J. Appl. Phys.* **18** (1979), 1111.
- [21] C. Bjormander, A. Grishin, B. Moon, J. Lee, and K. Rao: Ferroelectric superconductor $\text{PbZr}_{0.52}\text{Ti}_{0.48}\text{O}_3/\text{Y}_1\text{Ba}_2\text{Cu}_3\text{O}_{7-x}/\text{LaAlO}_3$ heterostructure prepared by Nd:YAG pulsed-laser deposition. *Appl. Phys. Lett.* **64** (1994), 3646.
- [22] W. Merz: Domain properties in BaTiO_3 . *Physical Review* **88** (1952), 421.
- [23] J. W. Matthews, S. Mader, and T. B. Light: Accommodation of misfit across the interface between crystals of semiconducting elements or compounds. *J. Appl. Phys.* **41** (1970), 3800.
- [24] P. K. Larsen, G. J. M. Dormans, D. J. Taylor, and P. J. Vanveldhoven: Ferroelectric properties and fatigue of $\text{PbZr}_{0.51}\text{Ti}_{0.49}\text{O}_3$ thin-films of varying thickness - blocking layer model. *J. Appl. Phys.* **76** (1994), 2405.
- [25] L. Pintilie: Extrinsic contributions to the apparent thickness dependence of the dielectric constant in epitaxial $\text{Pb}(\text{Zr},\text{Ti})\text{O}_3$ thin films. *Phys. Rev. B* **75** (2007), 224113.
- [26] U. Böttger: Dielectric properties of polar oxides. In R. Waser, U. Böttger, and S. Tiedke (eds.) *Polar Oxides*. WILEY-VCH Verlag GmbH & Co. KGaA (2005).
- [27] J. Curie and P. Curie: Sur l'électricité polaire dans les cristaux hémieédres á faces inclinées. *C.R. Acad. Sci.* **91** (1880), 383.
- [28] J. Valasek: Piezo-electric and allied phenomena in rochelle salt. *Phys. Rev.* **17** (1921), 475.
- [29] C.-L. Jia, S.-B. Mi, K. Urban, I. Vrejoiu, M. Alexe, and D. Hesse: Atomic-scale study of electric dipoles near charged and uncharged domain walls in ferroelectric films. *Nat. Mater.* **7** (2008), 57.
- [30] E. Little: Dynamic behavior of domain walls in barium titanate. *Phys. Rev.* **98** (1955), 978.
- [31] M. Marutake and T. Ikeda: Anisotropy in polarized barium titanate ceramics. *J. Phys. Soc. Jpn.* **12** (1957), 233.

- [32] N. Uchida and T. Ikeda: Temperature and bias characteristics of $\text{Pb}(\text{Zr,Ti})\text{O}_3$ families ceramics. *Jpn. J. Appl. Phys.* **4** (1965), 867.
- [33] L. Wu, C.-C. Wei, T.-S. Wu, and C.-C. Teng: Dielectric properties of modified PZT ceramics. *J. Phys. C: Solid State Phys.* **16** (1983), 2803.
- [34] V. M. Goldschmidt: Die Gesetze der Krystallochemie. *Naturwissenschaften* **14** (1926), 477.
- [35] T. Tsuchiya and J. Tsuchiya: High-pressure-high-temperature phase relations of MgGeO_3 : First-principles calculations. *Phys. Rev. B* **76** (2007), 092105.
- [36] P. Goudochnikov and A. J. Bell: Correlations between transition temperature, tolerance factor and cohesive energy in $2+$: $4+$ perovskites. *J. Phys.: Condens. Matter* **19** (2007), 176201.
- [37] B. Jaffe, W. R. Cook, and H. Jaffe: *Piezoelectric ceramics*. Academic Press (1971).
- [38] D. Berlincourt: Transducers using forced transitions between ferroelectric and antiferroelectric states. *IEEE T. Son. Ultrason.* **SU13** (1966), 116.
- [39] G. Shirane and K. Suzuki: Crystal structure of $\text{Pb}(\text{Zr-Ti})\text{O}_3$. *J. Phys. Soc. Jpn.* **7** (1952), 333.
- [40] S. Alpay, V. Nagarajan, L. Bendersky, M. Vaudin, S. Aggarwal, R. Ramesh, and A. Roytburd: Effect of the electrode layer on the polydomain structure of epitaxial $\text{PbZr}_{0.2}\text{Ti}_{0.8}\text{O}_3$ thin films. *J. Appl. Phys.* **85** (1999), 3271.
- [41] J. Frantti, J. Lappalainen, S. Eriksson, V. Lantto, S. Nishio, M. Kakihana, S. Ivanov, and H. Rundlof: Neutron diffraction studies of $\text{Pb}(\text{Zr}_x\text{Ti}_{1-x})\text{O}_3$ ceramics. *Jpn. J. Appl. Phys., Part 1* **39** (2000), 5697. 17th Meeting on Ferroelectric Materials and Their Applications (FAM-17), Kyoto, Japan, May 24-27, 2000.
- [42] L. Pintilie, I. Vrejoiu, G. L. Rhun, and M. Alexe: Short-circuit photocurrent in epitaxial lead zirconate-titanate thin films. *J. Appl. Phys.* **101** (2007), 064109.
- [43] S. Yang, Y. Zhang, and D. Mo: A comparison of the optical properties of amorphous and polycrystalline PZT thin films deposited by the sol-gel method. *Mater. Sci. Eng., B* **127** (2006), 117.
- [44] Z. Zhang, P. Wu, K. P. Ong, L. Lu, and C. Shu: Electronic properties of A-site substituted lead zirconate titanate: Density functional calculations. *Phys. Rev. B* **76** (2007), 125102.
- [45] M. Raymond and D. Smyth: Defects and charge transport in perovskite ferroelectrics. *J. Phys. Chem. Solids* **57** (1996), 1507.
- [46] J. F. Scott: *Ferroelectric memories*. Springer (2000).
- [47] L. Pintilie, I. Vrejoiu, D. Hesse, and M. Alexe: The influence of the top-contact metal on the ferroelectric properties of epitaxial ferroelectric $\text{Pb}(\text{Zr}_{0.2}\text{Ti}_{0.8})\text{O}_3$ thin films. *J. Appl. Phys.* **104** (2008), 114101.
- [48] T. Yamanaka, N. Hirai, and Y. Komatsu: Structure change of $\text{Ca}_{1-x}\text{Sr}_x\text{TiO}_3$ perovskite with composition and pressure. *Am. Mineral.* **87** (2002), 1183.

- [49] N. D. Zakharov, K. Satyalakshmi, G. Koren, and D. Hesse: Substrate temperature dependence of structure and resistivity of SrRuO₃ thin films grown by pulsed laser deposition on (100) SrTiO₃. *J. Mater. Res.* **14** (1999), 4385.
- [50] S. Cuffini, J. Guevara, and Y. Mascarenhas: Structural analysis of polycrystalline CaRuO₃ and SrRuO₃ ceramics from room temperature up to 1273 k. *Mater. Sci. Forum* **228** (1996), 789.
- [51] S. Bushmeleva, V. Pomjakushin, E. Pomjakushina, D. Sheptyakov, and A. Balagurov: Evidence for the band ferromagnetism in SrRuO₃ from neutron diffraction. *Journal of Magnetism and Magnetic Materials* **305** (2006), 491.
- [52] A. T. Zayak, X. Huang, J. B. Neaton, and K. M. Rabe: Structural, electronic, and magnetic properties of SrRuO₃ under epitaxial strain. *Phys. Rev. B* **74** (2006), 094104.
- [53] H. M. Duiker, P. D. Beale, J. F. Scott, C. A. P. de Araujo, B. M. Melnick, J. D. Cuchiaro, and L. D. McMillan: Fatigue and switching in ferroelectric memories: Theory and experiment. *J. Appl. Phys.* **68** (1990), 5783.
- [54] J. A. Venables and G. L. Price: Nucleation of thin films. In J. W. Matthews (ed.) *Epitaxial Growth Part B*, pp. 382–436. Academic Press, Inc. (1975).
- [55] H. Bethge: Nucleation and surface conditions. *J. Vac. Sci. Technol.* **6** (1969), 460.
- [56] G. Rosenfeld, B. Poelsema, and G. Comsa: Epitaxial growth modes far from equilibrium. In D. A. King (ed.) *The chemical physics of solid surfaces*. Elsevier Science B.V. (1997).
- [57] K. Sangwal and R. Rodriguez-Clemente: *Surface morphology of crystalline materials*. Trans Tech Publications (1991).
- [58] J. W. Matthews and A. E. Blakeslee: Defects in epitaxial multilayers. 1. Misfit dislocations. *J. Crystal Growth* **27** (1974), 118.
- [59] A. H. Cottrell: *Dislocations and plastic flow in crystals*. Clarendon Press (1953).
- [60] J. E. Ayers: *Heteroepitaxy of semiconductors : Theory, growth, and characterization*. CRC Press (2007).
- [61] K. Iijima, R. Takayama, Y. Tomita, and I. Ueda: Epitaxial growth and the crystallographic, dielectric, and pyroelectric properties of lanthanum-modified lead titanate thin films. *J. Appl. Phys.* **60** (1986), 2914.
- [62] R. E. Cohen: Origin of ferroelectricity in perovskite oxides. *Nature* **358** (1992), 136.
- [63] C. Ederer and N. A. Spaldin: Effect of epitaxial strain on the spontaneous polarization of thin film ferroelectrics. *Phys. Rev. Lett.* **95** (2005), 257601.
- [64] C.-L. Jia, V. Nagarajan, J.-Q. He, L. Houben, T. Zhao, R. Ramesh, K. Urban, and R. Waser: Unit-cell scalemapping of ferroelectricity and tetragonality in epitaxial ultrathin ferroelectric films. *Nat. Mater.* **6** (2007), 64.
- [65] H. N. Lee, S. M. Nakhmanson, M. F. Chisholm, H. M. Christen, K. M. Rabe, and D. Vanderbilt: Suppressed dependence of polarization on epitaxial strain in highly polar ferroelectrics. *Phys. Rev. Lett.* **98** (2007), 217602.

- [66] K. Iijima, Y. Tomita, R. Takayama, and I. Ueda: Preparation of c-axis oriented PbTiO₃ thin films and their crystallographic, dielectric, and pyroelectric properties. *J. Appl. Phys.* **60** (1986), 361.
- [67] Z.-G. Ban and S. P. Alpay: Dependence of the pyroelectric response on internal stresses in ferroelectric thin films. *Appl. Phys. Lett.* **82** (2003), 3499.
- [68] A. Sharma, Z.-G. Ban, S. P. Alpay, and J. V. Mantese: Pyroelectric response of ferroelectric thin films. *J. Appl. Phys. Lett.* **95** (2004), 3618.
- [69] W. D. Nix: Mechanical properties of thin films. *Metall. Trans. A* **20** (1989), 2217.
- [70] J. Speck and W. Pompe: Domain configurations due to multiple misfit relaxation mechanisms in epitaxial ferroelectric thin films. I. Theory. *J. Appl. Phys.* **76** (1994), 466.
- [71] S. Stemmer, S. K. Streiffer, F. Ernst, and M. Rühle: Dislocations in PbTiO₃ thin films. *Phys. Stat. Sol. (a)* **147** (1995), 135.
- [72] T. Suzuki, Y. Nishi, and M. Fujimoto: Analysis of misfit relaxation in heteroepitaxial BaTiO₃ thin films. *Philos. Mag. A* **79** (1999), 2461.
- [73] S. H. Oh and C. G. Park: Misfit strain relaxation by dislocations in SrRuO₃/SrTiO₃ (001) heteroepitaxy. *J. Appl. Phys.* **95** (2004), 4691.
- [74] S. P. Alpay and A. L. Roytburd: Thermodynamics of polydomain heterostructures. III. Domain stability map. *J. Appl. Phys.* **83** (1998), 4714.
- [75] H. M. Smith and A. F. Turner: Vacuum deposited thin films using a ruby laser. *Appl. Opt.* **4** (1965), 147.
- [76] J. T. Cheung and T. Magee: Recent progress on LADA growth of HgCdTe and CdTe epitaxial layers. *J. Vac. Sci. Technol., A* **1** (1983), 1604.
- [77] J. T. Cheung and H. Sankur: Growth of thin-films by laser-induced evaporation. *CRC Crit. Rev. Solid State Mater. Sci.* **15** (1988), 63.
- [78] D. Bauerle, M. Dinescu, R. Dinu, J. Pedarnig, J. Heitz, R. Schwodiauer, S. Bauer, and S. Bauer-Gogonea: Pulsed-laser deposition and characterization of thin films. In C. Galassi, M. Dinescu, K. Uchino, and M. Sayer (eds.) *Piezoelectric materials: Advances in science, technology and applications*. Kluwer Acad. Publ. (2000).
- [79] J. T. Cheung: History and fundamentals of pulsed laser deposition. In D. B. Chrisey and G. K. Hubler (eds.) *Pulsed Laser Deposition of Thin Films*. John Wiley & Sons, Inc. (1994).
- [80] R. Kelly and A. Miotello: Mechanisms of pulsed laser sputtering. In D. B. Chrisey and G. K. Hubler (eds.) *Pulsed Laser Deposition of Thin Films*. John Wiley & Sons, Inc. (1994).
- [81] G. Koren, R. J. Baseman, A. Gupta, M. I. Lutwyche, and R. B. Laibowitz: Particulates reduction in laser-ablated YBa₂Cu₃O₇-delta thin-films by laser-induced plume heating. *Appl. Phys. Lett.* **56** (1990), 2144.
- [82] S. M. Green, A. Piqué, K. S. Harshavardhan, and J. Bernstein: Equipment. In D. B. Chrisey and G. K. Hubler (eds.) *Pulsed Laser Deposition of Thin Films*. John Wiley & Sons, Inc. (1994).

- [83] C. Chan and J. Mazumder: One-dimensional steady-state model for damage by vaporization and liquid expulsion due to laser-material interaction. *J. Appl. Phys.* **62** (1987), 4579.
- [84] R. E. Leuchtner and K. S. Grabowski: Ferroelectrics. In D. B. Chrisey and G. K. Hubler (eds.) *Pulsed Laser Deposition of Thin Films*. John Wiley & Sons, Inc. (1994).
- [85] C. C. Chang, X. D. Wu, R. Ramesh, X. X. Xi, T. S. Ravi, T. Venkatesan, D. M. Hwang, R. E. Muenchausen, S. Foltyn, and N. S. Nogar: Origin of surface-roughness for c-axis oriented Y-Ba-Cu-O superconducting films. *Appl. Phys. Lett.* **57** (1990), 1814.
- [86] J. S. Horwitz and J. A. Sprague: Film nucleation and film growth in pulsed laser deposition of ceramics. In D. B. Chrisey and G. K. Hubler (eds.) *Pulsed Laser Deposition of Thin Films*. John Wiley & Sons, Inc. (1994).
- [87] W. Hong, H. N. Lee, M. Yoon, H. M. Christen, D. H. Lowndes, Z. G. Suo, and Z. Y. Zhang: Persistent step-flow growth of strained films on vicinal substrates. *Phys. Rev. Lett.* **95** (2005), 095501.
- [88] S. R. Foltyn, R. C. Dye, K. C. Ott, E. Peterson, K. M. Hubbard, W. Hutchinson, R. E. Muenchausen, R. C. Estler, and X. D. Wu: Target modification in the excimer laser deposition of $\text{YBa}_2\text{Cu}_3\text{O}_{7-x}$ thin films. *Appl. Phys. Lett.* **59** (1991), 594.
- [89] N. B. Ibrahim, C. Edwards, and S. B. Palmer: Yttrium iron garnet surface modification during pulsed laser ablation deposition. *Materials Science-Poland* **22** (2004), 111.
- [90] J. C. Jiang, X. Q. Pan, W. Tian, C. D. Theis, and D. G. Schlom: Abrupt $\text{PbTiO}_3/\text{SrTiO}_3$ superlattices grown by reactive molecular beam epitaxy. *Appl. Phys. Lett.* **74** (1999), 2851.
- [91] M. Kawasaki, K. Takahashi, T. Maeda, R. Tsuchiya, M. Shinohara, O. Ishiyama, T. Yonezawa, M. Yoshimoto, and H. Koinuma: Atomic control of the SrTiO_3 crystal-surface. *Science* **266** (1994), 1540.
- [92] G. Koster, G. Rijnders, D. H. A. Blank, and H. Rogalla: Surface morphology determined by (001) single-crystal SrTiO_3 termination. *Physica C* **339** (2000), 215.
- [93] S. N. Magonov and M.-H. Whangbo: *Surface analysis with STM and AFM : Experimental and theoretical aspects of image analysis*. VCH (1996).
- [94] S. Kalinin and D. Bonnell: Electric scanning probe imaging and modification of ferroelectric surfaces. In M. Alexe and A. Gruverman (eds.) *Nanoscale characterisation of ferroelectric materials : Scanning probe microscopy approach*. Springer (2004).
- [95] D. B. Williams and C. B. Carter: *Transmission Electron Microscopy*. Plenum Press, New York and London (1996).
- [96] B. Agarwal: *X-ray spectroscopy : An introduction*. Springer-Verlag (1991).
- [97] L. Spieß, R. Schwarzer, H. Behnken, and G. Teichert: *Moderne Röntgenbeugung: Röntgendiffraktometrie für Materialwissenschaftler, Physiker und Chemiker*. Teubner (2005).
- [98] J. A. Bearden: X-ray wavelengths. *Rev. Mod. Phys.* **39** (1967), 78.
- [99] D. Williams, J. Goldstein, and D. E. Newbury (eds.): *X-ray spectrometry in electron beam instruments*. Plenum Press (1995).

- [100] L. C. Feldman and J. W. Mayer: *Fundamentals of surface and thin film analysis*. North Holland (1986).
- [101] A. Witzmann, *RUBSODY Users Guide, Friedrich-Schiller-Universität Jena, 1992*.
- [102] J. M. Spaeth, J. R. Niklas, and R. H. Bartram: *Structural analysis of point defects in solids: An introduction to multiple magnetic resonance spectroscopy*. Springer-Verlag (1992).
- [103] A. Hassan, L. Pardi, J. Krzystek, A. Sienkiewicz, P. Goy, M. Rohrer, and L. Brunel: Ultrawide band multifrequency high-field EMR technique: A methodology for increasing spectroscopic information. *J. Magn. Reson.* **142** (2000), 300.
- [104] J. van Tol, L. Brunel, and R. Wylde: A quasioptical transient electron spin resonance spectrometer operating at 120 and 240 GHz. *Rev. Sci. Instrum.* **76** (2005), 074101.
- [105] D. Newman and B. Ng: The superposition model of crystal fields. *Rep. Prog. Phys.* **52** (1989), 699.
- [106] G. Kresse and J. Furthmüller: Efficient iterative schemes for ab initio total-energy calculations using a plane-wave basis set. *Phys. Rev. B* **54** (1996), 11169.
- [107] G. Kresse and D. Joubert: From ultrasoft pseudopotentials to the projector augmented-wave method. *Phys. Rev. B* **59** (1999), 1758.
- [108] I. Vrejoiu, G. LeRhun, L. Pintilie, D. Hesse, M. Alexe, and U. Gösele: Intrinsic ferroelectric properties of strained tetragonal $\text{PbZr}_{0.2}\text{Ti}_{0.8}\text{O}_3$ obtained on layer-by-layer grown, defect-free single-crystalline films. *Adv. Mater.* **18** (2006), 1657.
- [109] G. Shirane, K. Suzuki, and A. Takeda: Phase transitions in solid solutions of PbZrO_3 and PbTiO_3 . 2. X-ray study. *J. Phys. Soc. Jpn.* **7** (1952), 12.
- [110] A. S. Sonin and B. A. Strukov: *Einführung in die Ferroelektrizität*. Akademie-Verlag, Berlin (1974).
- [111] M. Haun, E. Furman, S. Jang, and L. Cross: Thermodynamic theory of the lead zirconate-titanate solid-solution system, part 5: Theoretical calculations. *Ferroelectrics* **99** (1989), 63.
- [112] M. E. Lines and A. M. Glass: *Principles and Applications of Ferroelectric and Related Materials*. Clarendon Press Oxford (2004).
- [113] D. Bolten, O. Lohse, M. Grossmann, and R. Waser: Reversible and irreversible domain wall contributions to the polarization in ferroelectric thin films. *Ferroelectrics* **221** (1999), 251.
- [114] C. Sudhama, A. C. Campbell, P. D. Maniar, R. E. Jones, R. Moazzami, C. J. Mogab, and J. C. Lee: A model for electrical-conduction in metal-ferroelectric-metal thin-film capacitors. *J. Appl. Phys.* **75** (1994), 1014.
- [115] L. Pintilie and M. Alexe: Metal-ferroelectric-metal heterostructures with Schottky contacts. I. Influence of the ferroelectric properties. *J. Appl. Phys.* **98** (2005), 123103.
- [116] A. Hartmann, M. Neilson, R. Lamb, K. Watanabe, and J. Scott: Ruthenium oxide and strontium ruthenate electrodes for ferroelectric thin-films capacitors. *Appl. Phys. A* **70** (2000), 239.

- [117] S. M. Sze and K. K. Ng: *Physics of semiconductor devices*. John Wiley & Sons, Inc. (2007).
- [118] D. K. Schroder: *Semiconductor material and device characterization*. Wiley-Interscience, 3. edn. (2006).
- [119] L. Pintilie, I. Boerasu, M. J. M. Gomes, T. Zhao, R. Ramesh, and M. Alexe: Metal-ferroelectric-metal structures with Schottky contacts. II. Analysis of the experimental current-voltage and capacitance-voltage characteristics of Pb(Zr,Ti)O₃ thin films. *J. Appl. Phys.* **98** (2005), 123104.
- [120] L. Pintilie, I. Vrejoiu, G. LeRhun, D. Hesse, M. Alexe, and U. Gösele: Electrical characterization of ferroelectric thin films: Intrinsic versus extrinsic contributions to material properties. In *E-MRS Spring Meeting* (2006) .
- [121] H. Amano, M. Iwaya, N. Hayashi, T. Kashima, M. Katsuragawa, T. Takeuchi, C. Wetzel, and I. Akasaki: Improvement of crystalline quality of group III nitrides on sapphire using low temperature interlayers. *MRS Internet J. Nitride Semicond. Res.* **4** (1999), G10.1.
- [122] A. Dadgar, M. Poschenrieder, O. Contreras, J. Christen, K. Fehse, J. Blasing, A. Diez, F. Schulze, T. Riemann, F. A. Ponce, and A. Krost: Bright, crack-free InGaN/GaN light emitters on Si(111). *Phys. Status Solidi A* **192** (2002), 308.
- [123] L. Feigl, I. B. Misirlioglu, I. Vrejoiu, M. Alexe, and D. Hesse: Impact of misfit relaxation and a-domain formation on the electrical properties of tetragonal PbZr_{0.4}Ti_{0.6}O₃ / PbZr_{0.2}Ti_{0.8}O₃ thin film heterostructures: Experiment and theoretical approach. *J. Appl. Phys.* **105** (2009), 061607.
- [124] V. G. Koukhar, N. A. Pertsev, and R. Waser: Thermodynamic theory of epitaxial ferroelectric thin films with dense domain structures. *Phys. Rev. B* **64** (2001), 214103.
- [125] A. L. Roytburd, S. Zhong, and S. P. Alpay: Dielectric anomaly due to electrostatic coupling in ferroelectric-paraelectric bilayers and multilayers. *Appl. Phys. Lett.* **87** (2005), 092902.
- [126] N. A. Pertsev, A. G. Zembilgotov, and A. K. Tagantsev: Effect of mechanical boundary conditions on phase diagrams of epitaxial ferroelectric thin films. *Phys. Rev. Lett.* **80** (1998), 1988.
- [127] N. Pertsev, V. Kukhar, H. Kohlstedt, and R. Waser: Phase diagrams and physical properties of single-domain epitaxial Pb(Zr_{1-x}Ti_x)O₃ thin films. *Phys. Rev. B* **67** (2003), 054107.
- [128] G. Le Rhun, I. Vrejoiu, L. Pintilie, D. Hesse, M. Alexe, and U. Gösele: Increased ferroelastic domain mobility in ferroelectric thin films and its use in nano-patterned capacitors. *Nanotechnol.* **17** (2006), 3154.
- [129] M. Stengel and N. A. Spaldin: Origin of the dielectric dead layer in nanoscale capacitors. *Nature* **443** (2006), 679.
- [130] A. M. Bratkovsky and A. P. Levanyuk: Very large dielectric response of thin ferroelectric films with the dead layers. *Phys. Rev. B* **63** (2001), 132103.
- [131] I. B. Misirlioglu, M. Alexe, L. Pintilie, and D. Hesse: Space charge contribution to the apparent enhancement of polarization in ferroelectric bilayers and multilayers. *Appl. Phys. Lett.* **91** (2007), 022911.

- [132] V. Nagarajan, J. Junquera, J. Q. He, C. L. Jia, R. Waser, K. Lee, Y. K. Kim, S. Baik, T. Zhao, R. Ramesh, P. Ghosez, and K. M. Rabe: Scaling of structure and electrical properties in ultrathin epitaxial ferroelectric heterostructures. *J. Appl. Phys.* **100** (2006), 051609.
- [133] B. Roy, S. B. Majumder, and R. S. Katiyar: Investigation on the dielectric and polarization behavior of sol-gel derived erbium doped $\text{Pb}(\text{Zr}_{0.53}\text{Ti}_{0.47})\text{O}_3$ thin films. *Integr. Ferroelectr.* **42** (2002), 373.
- [134] T. Kamiya, T. Suzuki, T. Tsurumi, and M. Daimon: Effects of manganese addition on piezoelectric properties of $\text{Pb}(\text{Zr}_{0.5}\text{Ti}_{0.5})\text{O}_3$. *Jpn. J. Appl. Phys.* **31** (1992), 3058.
- [135] R. Moazzami, C. Hu, and W. Shepherd: Electrical characteristics of ferroelectric PZT thin-films for DRAM applications. *IEEE T. Electron. Dev.* **39** (1992), 2044.
- [136] G. Arlt and H. Neumann: Internal BIAS in ferroelectric ceramics: Origin and time dependence. *Ferroelectrics* **87** (1988), 109.
- [137] U. Robels and G. Arlt: Domain-wall clamping in ferroelectrics by orientation of defects. *J. Appl. Phys.* **73** (1993), 3454.
- [138] O. Boser: Statistical-theory of hysteresis in ferroelectric materials. *J. Appl. Phys.* **62** (1987), 1344.
- [139] P. V. Lambeck and G. H. Jonker: Ferroelectric domain stabilization in BaTiO_3 by bulk ordering of defects. *Ferroelectrics* **22** (1978), 729.
- [140] M. Grossmann, O. Lohse, D. Bolten, U. Boettger, T. Schneller, and R. Waser: The interface screening model as origin of imprint in $\text{PbZr}_x\text{Ti}_{1-x}\text{O}_3$ thin films. I. Dopant, illumination, and bias dependence. *J. Appl. Phys.* **92** (2002), 2680.
- [141] H. Neumann and G. Arlt: Dipole orientation in Cr-modified BaTiO_3 ceramics. *Ferroelectrics* **76** (1987), 303.
- [142] W. Warren, G. Pike, K. Vanheusden, D. Dimos, B. Tuttle, and J. Robertson: Defect-dipole alignment and tetragonal strain in ferroelectrics. *J. Appl. Phys.* **79** (1996), 9250.
- [143] G. Pike, W. Warren, D. Dimos, B. Tuttle, R. Ramesh, J. Lee, V. Keramidis, and J. Evans: Voltage offsets in $(\text{Pb},\text{La})(\text{Zr},\text{Ti})\text{O}_3$ thin-films. *Appl. Phys. Lett.* **66** (1995), 484.
- [144] R.-A. Eichel, E. Erdem, P. Erhart, J. van Tol, L. Feigl, I. Vrejoiu, M. Alexe, R. Mattheis, and D. Hesse: Enhanced electric polarization in chromium-doped PZT20/80 thin films through formation and alignment of $(\text{Cr}'_{\text{Zr,Ti}}-\text{V}_\text{O}^{\bullet\bullet})_{\parallel}^{\bullet}$ defect dipoles. *To be submitted to Phys. Rev. Lett.*
- [145] R. Merkle and J. Maier: Defect association in acceptor-doped SrTiO_3 : case study for Fe_{Ti}' , $\text{V}_\text{O}^{\bullet\bullet}$ and $\text{Mn}_{\text{Ti}}''-\text{V}_\text{O}^{\bullet\bullet}$. *Phys. Chem. Chem. Phys.* **5** (2003), 2297. 78th International Discussion Meeting of the Deutsche-Bunsen-Gesellschaft-fur-Physikalische-Chemie, VAALS, NETHERLANDS, OCT 06-09, 2002.
- [146] R. Eichel, H. Mestric, K. Dinse, A. Ozarowski, J. van Tol, L. Brunel, H. Kungl, and M. Hoffmann: High-field/high-frequency EPR of paramagnetic functional centers in Cu^{2+} - and Fe^{3+} -modified polycrystalline $\text{Pb}[\text{Zr}_x\text{Ti}_{1-x}]\text{O}_3$ ferroelectrics. *Magn. Reson. Chem.* **43** (2005), S166.

- [147] L. Feigl, E. Pippel, L. Pintilie, M. Alexe, and D. Hesse: Chromium doping of epitaxial $\text{PbZr}_{0.2}\text{Ti}_{0.8}\text{O}_3$ thin films. *To be submitted to Appl. Phys. Lett.*
- [148] J. K. Kim, S. S. Kim, W. J. Kim, M. H. Park, A. S. Bhalla, and R. Guo: Influences of Cr doping on the electrical properties in BiFeO_3 thin films. *Ferroelectr. Lett.* **33** (2006), 91.
- [149] D. F. Ryder and N. K. Raman: Sol-gel processing of nb-doped $\text{Pb}(\text{Zr}, \text{Ti})\text{O}_3$ thin-films for ferroelectric memory applications. *J. Electron. Mater.* **21** (1992), 971.
- [150] S. B. Majumder, B. Roy, R. S. Katiyar, and S. B. Krupanidhi: Effect of acceptor and donor dopants on polarization components of lead zirconate titanate thin films. *Appl. Phys. Lett.* **79** (2001), 239.
- [151] R. Zuo, L. Li, X. Hu, and Z. Gui: Effect of silver dopant on electrical properties of PNIN-PNN-PZT piezoelectric ceramics by complex impedance spectroscopy. *Mater. Lett.* **54** (2002), 185.
- [152] R. Koduri and M. Lopez: Influence of mn on dielectric and piezoelectric properties of A-site and B-site modified PLZT nano-ceramics for sensor and actuator applications. *J. Mater. Sci. - Mater. Electron.* **19** (2008), 669.
- [153] A. Rose: Space-charge-limited currents in solids. *Phys. Rev.* **97** (1955), 1538.
- [154] D. Damjanovic: Ferroelectric, dielectric and piezoelectric properties of ferroelectric thin films and ceramics. *Rep. Prog. Phys.* **61** (1998), 1267.
- [155] L. Feigl, S. J. Zheng, B. I. Birajdar, B. J. Rodriguez, Y. L. Zhu, M. Alexe, and D. Hesse: Impact of high interface density on ferroelectric and structural properties of $\text{PbZr}_{0.2}\text{Ti}_{0.8}\text{O}_3$ / $\text{PbZr}_{0.4}\text{Ti}_{0.6}\text{O}_3$ epitaxial multilayers. *Submitted to J. Phys. D: Appl. Phys.*
- [156] K. Saito, T. Kurosawa, T. Akai, T. Oikawa, and H. Funakubo: Structural characterization and 90° domain contribution to ferroelectricity of epitaxial $\text{Pb}(\text{Zr}_{0.35}, \text{Ti}_{0.65})\text{O}_3$ thin films. *J. Appl. Phys.* **93** (2003), 545.
- [157] P. F. Fewster: *X-ray scattering from semiconductors*. Imperial College Press (2003).
- [158] I. Horcas, R. Fernández, J. M. Gómez-Rodríguez, J. Colchero, J. Gómez-Herrero, and A. M. Baro: WSXM: a software for scanning probe microscopy and a tool for nanotechnology. *Rev. Sci. Instrum.* **78** (2007), 013705.
- [159] S. Horii, S. Yokoyama, H. Nakajima, and S. Horita: Thickness dependence of material properties of epitaxial $\text{Pb}(\text{Zr}_x\text{Ti}_{1-x})\text{O}_3$ films on $\text{Ir}/(100) (\text{ZrO}_2)_{(1-x)}(\text{Y}_2\text{O}_3)_{(x)}/(100)\text{Si}$ structures. *Jpn. J. Appl. Phys., Part 1* **38** (1999), 5378.
- [160] T. Mitsui and S. Nomura: *Landolt-Börnstein Numerical data and functional relationships in science and technology: New series*, vol. III. Springer (1981).
- [161] M. Fiebig: Revival of the magnetoelectric effect. *J. Phys. D: Appl. Phys.* **38** (2005), R123.
- [162] Y.-H. Chu, L. W. Martin, M. B. Holcomb, M. Gajek, S.-J. Han, Q. He, N. Balke, C.-H. Yang, D. Lee, W. Hu, Q. Zhan, P.-L. Yang, A. Fraile-Rodriguez, A. Scholl, S. X. Wang, and R. Ramesh: Electric-field control of local ferromagnetism using a magnetoelectric multiferroic. *Nat. Mater.* **7** (2008), 478.

- [163] M. Bibes and A. Barthelemy: Multiferroics: Towards a magnetoelectric memory. *Nat. Mater.* **7** (2008), 425.
- [164] S. Lee, A. Pirogov, M. Kang, K.-H. Jang, M. Yonemura, T. Kamiyama, S. W. Cheong, F. Gozzo, N. Shin, H. Kimura, Y. Noda, and J. G. Park: Giant magneto-elastic coupling in multiferroic hexagonal manganites. *Nature* **451** (2008), 805.
- [165] N. Mathur: Materials science - A desirable wind up. *Nature* **454** (2008), 591.
- [166] R. Ramesh and N. A. Spaldin: Multiferroics: progress and prospects in thin films. *Nat. Mater.* **6** (2007), 21.
- [167] I. Stolichnov, S. W. E. Riester, H. J. Trodahl, N. Setter, A. W. Rushforth, K. W. Edmonds, R. P. Champion, C. T. Foxon, B. L. Gallagher, and T. Jungwirth: Non-volatile ferroelectric control of ferromagnetism in (Ga, Mn)As. *Nat. Mater.* **7** (2008), 464.
- [168] N. Hill: Why are there so few magnetic ferroelectrics? *J. Phys. Chem. B* **104** (2000), 6694.
- [169] W. Eerenstein, N. D. Mathur, and J. F. Scott: Multiferroic and magnetoelectric materials. *Nature* **442** (2006), 759.

Lebenslauf

Persönliche Daten

Name - Ludwig Feigl
Geburtsname - Geske
Adresse - Große Schlossgasse 1
06108 Halle
E-Mail (priv.) - lfeigl@web.de
E-Mail (off.) - feigl@uni-potsdam.de
Tel. (priv.) - 0345 - 6786746
0174 - 8879622
Tel. (off.) - 0331 - 9775711

Beruflicher Werdegang

seit 2009 - akademischer Mitarbeiter der Universität Potsdam
2006 - 2009 - Promotionsstudent am Max-Planck-Institut für Mikrostrukturphysik
Abschluss mit "magna cum laude"
2005 - 2006 - Promotionsstudent an der Martin- Luther-Universität Halle-Wittenberg
1999 - 2005 - Physikstudium an der Martin-Luther-Universität Halle-Wittenberg
Abschluss als Diplom-Physiker
Diplomarbeitstitel: "Elektromechanische und dielektrische Untersuchungen an Bariumtitanat-Stannat Keramiken"
1998 - 1999 - Zivildients an der Caritas Sozialstation Bad Lauchstädt
1991 - 1998 - Domgymnasium Merseburg, Abschluss mit dem Abitur
1986 - 1991 - Grundschule: Kurt-Kittelmann-Oberschule Schafstädt

Weitere Tätigkeiten

2003 - WE-Heraeus-Ferienkurs für Physik: Ferroelektrika - Intelligente
Materialien für Aktoren, Sensoren und Speicher
2002 - Studentische Hilfskraft am Max-Planck-Institut für Mikrostrukturphysik
2001 - Studentische Hilfskraft am Max-Planck-Institut für Mikrostrukturphysik

Stipendien

2005 - 2007 - Graduiertenförderung des Landes Sachsen-Anhalt

Qualifikationen

- experimentell - Dünnfilmherstellung: Gepulste Laserabscheidung
strukturelle Charakterisierung: (HR)TEM, XRD, AFM, PFM
elektrische Charakterisierung: P-V, C-V, I-V, Impedanzspektroskopie
- theoretisch - Landautheorie
- EDV - Mathematica, MS Office, Origin, Tex, Turbo Pascal
- Sprachen - flüssiges Englisch, Grundkenntnisse in Französisch und Latein

Veröffentlichungen

Artikel

Mein Familienname hat sich auf Grund meiner Heirat im Jahr 2008 von *Geske* zu *Feigl* geändert. Deshalb bin ich in älteren Veröffentlichungen als *L. Geske* aufgeführt.

- L. Feigl, E. Pippel, L. Pintilie, M. Alexe, and D. Hesse: Chromium doping of epitaxial $\text{PbZr}_{0.2}\text{Ti}_{0.8}\text{O}_3$ thin films. *J. Appl. Phys.* **105** (2009), 126103.
- L. Feigl, S. J. Zheng, B. I. Birajdar, B. J. Rodriguez, Y. L. Zhu, M. Alexe, and D. Hesse: Impact of high interface density on ferroelectric and structural properties of $\text{PbZr}_{0.2}\text{Ti}_{0.8}\text{O}_3$ / $\text{PbZr}_{0.4}\text{Ti}_{0.6}\text{O}_3$ epitaxial multilayers. *J. Phys. D.* **42** (2009) 085305.
- L. Feigl, I. B. Misirlioglu, I. Vrejoiu, M. Alexe, and D. Hesse: Impact of misfit relaxation and a-domain formation on the electrical properties of tetragonal $\text{PbZr}_{0.4}\text{Ti}_{0.6}\text{O}_3$ / $\text{PbZr}_{0.2}\text{Ti}_{0.8}\text{O}_3$ thin film heterostructures – experiment and theoretical approach. *J. Appl. Phys.* **105** (2009), 061607.
(auch verfügbar als: L. Geske, I. B. Misirlioglu, I. Vrejoiu, M. Alexe, and D. Hesse: Impact of misfit strain on the properties of tetragonal $\text{Pb}(\text{Zr,Ti})\text{O}_3$ thin film heterostructures. arXiv:0803.2805v1 [cond-mat.mtrl-sci] (2008), 1–9.)
- K. Barz, M. Diestelhorst, H. Beige, L. Geske, M. Alexe, and D. Hesse: Nonlinear dielectric behaviour of metal/ferroelectric/metal and metal/ferroelectric/semiconductor-heterostructures. *Proc. 16th IEEE Intern. Symp. on Appl. of Ferroelectrics* (2007), 212-213.
- L. Geske, V. Mueller, and H. Beige: Influence of the poling conditions on the ferroelectric properties of orthorhombic $\text{Ba}(\text{Ti,Sn})\text{O}_3$ ceramics. *Ferroelectrics* **361** (2007), 37–44.
- U. Straube, B. Broich, L. Geske, R. Steinhausen, H. T. Langhammer, H. Beige, and H.-P. Abicht: Ultrasound investigations of $\text{BaTi}_{1-x}\text{Sn}_x\text{O}_3$ ceramics. *Ferroelectrics* **353** (2007), 598–604.
- L. Geske, H. Beige, H. Abicht, and V. Mueller: Electromechanical resonance study of the diffuse ferroelectric phase transition in $\text{BaTi}_{1-x}\text{Sn}_x\text{O}_3$ ceramics. *Ferroelectrics* **314** (2005), 97–104.
- L. Geske, V. Lorenz, T. Muller, L. Jager, H. Beige, H. Abicht, and V. Mueller: Dielectric and electromechanical characterisation of fine-grain $\text{BaTi}_{0.95}\text{Sn}_{0.05}\text{O}_3$ ceramics sintered from glycolate-precursor powder. *J. Eur. Ceram. Soc.* **25** (2005), 2537–2542.

Tagungsbeiträge

- L. Feigl, Y. L. Zhu, B. I. Birajdar, B. J. Rodriguez, Y. S. Kim, I. Vrejoiu, M. Alexe, and D. Hesse: Impact of high interface density on ferroelectric and structural properties of $\text{PbZr}_{0.2}\text{Ti}_{0.8}\text{O}_3$ / $\text{PbZr}_{0.4}\text{Ti}_{0.6}\text{O}_3$ epitaxial multilayers. *2009 MRS Spring Meeting*, San Francisco (Vortrag)
- L. Feigl, L. Pintilie, E. Pippel, I. Vrejoiu, M. Alexe, and D. Hesse: Cr doping of epitaxial $\text{PbZr}_{0.2}\text{Ti}_{0.8}\text{O}_3$ films. *2009 MRS Spring Meeting*, San Francisco (Poster)
- L. Feigl, S. J. Zheng, B. I. Birajdar, B. J. Rodriguez, Y. L. Zhu, M. Alexe, and D. Hesse: Impact of high interface density on ferroelectric and structural properties of $\text{PbZr}_{0.2}\text{Ti}_{0.8}\text{O}_3$ / $\text{PbZr}_{0.4}\text{Ti}_{0.6}\text{O}_3$ epitaxial multilayers. *DPG Spring Meeting 2009*, Dresden (Vortrag)
- L. Feigl, E. Pippel, I. Vrejoiu, R.-A. Eichel, E. Erdem, R. Mattheis, M. Alexe, and D. Hesse: Cr doping of epitaxial $\text{PbZr}_{0.2}\text{Ti}_{0.8}\text{O}_3$ films. *DPG Spring Meeting 2009*, Dresden (Poster)
- L. Geske, I. B. Misirlioglu, I. Vrejoiu, M. Alexe, and D. Hesse: The impact of misfit strain on the properties of ferroelectric bilayers: A LGD approach. *20th International Symposium on Integrated Ferroelectrics 2008*, Singapore (Vortrag)
- L. Geske, I. B. Misirlioglu, I. Vrejoiu, M. Alexe, and D. Hesse: The impact of misfit strain on the properties of ferroelectric bilayers: A LGD approach. *72nd Annual Meeting of the DPG 2008*, Berlin (Vortrag)
- L. Geske, I. Vrejoiu, L. Pintilie, I. B. Misirlioglu, M. Alexe, and D. Hesse: Impact of interfaces and structural defects on the properties of tetragonal $\text{Pb}(\text{Zr},\text{Ti})\text{O}_3$ thin film heterostructures. *19th International Symposium on Integrated Ferroelectrics 2007*, Bordeaux (Vortrag)
- L. Geske, I. Vrejoiu, L. Pintilie, I. B. Misirlioglu, M. Alexe, and D. Hesse: Impact of interfaces and structural defects on the properties of tetragonal $\text{Pb}(\text{Zr},\text{Ti})\text{O}_3$ thin film heterostructures. *71st Annual Meeting of the DPG 2007*, Regensburg (Vortrag)
- K. Barz, M. Diestelhorst, H. Beige, L. Geske, M. Alexe, and D. Hesse: Size and Microstructure Effects on Nonlinear Dielectric Properties of Nanoscaled Ferroelectrics. *International Symposium: Nonlinear Dynamics of Nanosystems 2006*, Chemnitz (Poster)
- L. Geske: Elektromechanische Resonanzuntersuchungen an Bariumtitanat-Stannat Keramiken. *Doktorandenworkshop im Rahmen des Schwerpunktprogramms „Substitutionseffekte in ionischen Festkörpern“ 2004*, Rauischholzhausen (Poster)

Danksagung

Als Abschluss meiner Arbeit möchte ich mich bei allen Personen bedanken, die mich während der gesamten Zeit unterstützt haben. Prof. Ulrich Gösele hat es mir ermöglicht, am Max-Planck-Institut für Mikrostrukturphysik zu arbeiten, dadurch stand mir die hochwertige Ausrüstung und die Unterstützung von hervorragenden Mitarbeitern aus aller Welt zur Verfügung.

Prof. Dietrich Hesse danke ich für die hervorragende Betreuung, verbunden mit immer ermutigenden Worten und unermüdlichem Eintreten für meine Interessen, und ich danke ihm für sein Engagement, mir die Möglichkeit zu geben, meine Ergebnisse auf Tagungen und in Zeitschriften zu präsentieren.

Besonderer Dank gilt Dr. Marin Alexe und Dr. Ionela Vrejoiu. Sie haben mich in die spannende Welt der Herstellung und Charakterisierung von dünnen ferroelektrischen Filme eingeführt. Sowohl bei experimentellen Schwierigkeiten als auch bei Verständnisproblemen standen sie mir immer mit detaillierten Hilfestellungen und Hinweisen zur Seite. Ohne sie wäre es mir nicht möglich gewesen, solch hochwertige Schichten abzuscheiden, umfassend zu untersuchen und zu verstehen.

Meinen beiden zeitweiligen Kollegen im Büro, Dr. Burç Mısırlıoğlu und Dr. Lucian Pintilie, möchte ich mich für die aufschlussreichen Diskussionen zur theoretischen Beschreibung meiner Ergebnisse bedanken. Das erlaubte mir ein tieferes Verständnis der Effekte, eine teilweise Quantifizierung der physikalischen Größen und war ein gutes Training für mein mündliches Englisch.

Der unermüdlich schleifenden Frau Sina Swatek danke ich für die Präparation der vielen TEM-Proben, Herr Norbert Schammelt für die Wartung der PLD-Anlage, Dr. Steffen Schmidt für die Einweisung am TEM, Herr Andreas Schubert für die Einweisung am Röntgendiffraktometer und Dr. Brian Rodriguez für die Einweisung am PFM.

Auch den wichtigsten Personen in meinem Leben, meiner Frau und meinen Kindern, möchte ich vielmals danken. Sie trugen zwar nicht direkt zur Arbeit bei, aber durch ihre Unterstützung und bloße Gegenwart haben sie mir soviel gegeben, dass sowohl meine Person als auch meine Arbeit durch sie nachhaltig beeinflusst wurden.

Zu guter Letzt danke ich Frau Theresa Geske, Frau Ulrike Hoffmann und Dr. Johannes Hohlbein für das Korrekturlesen von Teilen meiner Arbeit und ihre Hinweise auf meine Verfehlungen im schriftlichen Englisch. Alle weiteren Personen, die zur Entstehung der Arbeit beigetragen haben und hier keine namentliche Erwähnung fanden, mögen mir verzeihen, selbstverständlich danke ich auch ihnen.